3-11-2011

An Analytical Model of Nanometer Scale Viscoelastic Properties of Polymer Surfaces Measured Using an Atomic Force Microscope

Jacob B. Goldberg

Recommended Citation

Goldberg, Jacob B., "An Analytical Model of Nanometer Scale Viscoelastic Properties of Polymer Surfaces Measured Using an Atomic Force Microscope" (2011). *Theses and Dissertations*. 1482.
https://scholar.afit.edu/etd/1482

An Analytical Model of Nanometer Scale Viscoelastic Properties of Polymer Surfaces Measured Using an Atomic Force Microscope

DISSERTATION

Jacob B. Goldberg,

AFIT/DAM/ENC/11-03

DEPARTMENT OF THE AIR FORCE
AIR UNIVERSITY

AIR FORCE INSTITUTE OF TECHNOLOGY

Wright-Patterson Air Force Base, Ohio

AFIT/DAM/ENC/11-03

AN ANALYTICAL MODEL OF NANOMETER SCALE VISCOELASTIC PROPERTIES OF POLYMER SURFACES MEASURED USING AN ATOMIC FORCE MICROSCOPE

DISSERTATION

Presented to the Faculty
Graduate School of Engineering and Management
Air Force Institute of Technology
Air University
Air Education and Training Command
in Partial Fulfillment of the Requirements for the
Degree of Doctor of Philosophy

Jacob B. Goldberg, B.A., M.S.

March 2011

AFIT/DAM/ENC/11-03

AN ANALYTICAL MODEL OF NANOMETER SCALE VISCOELASTIC PROPERTIES OF POLYMER SURFACES MEASURED USING AN ATOMIC FORCE MICROSCOPE

Jacob B. Goldberg, B.A., M.S.

Approved:

//signed//	March 2011
Dr. William Baker Dissertation Advisor	Date
//signed//	March 2011
Dr. Mark Oxley Committee Member	Date
//signed//	March 2011
Dr. Larry Burggraf Committee Member	Date
//signed//	March 2011
Dr. Anthony Palazotto Committee Member	Date

Accepted:

//signed//	March 2011
M. U. Thomas Dean, Graduate School of Engineering and Management	Date

AFIT/DAM/ENC/11-03

Abstract

The United States Air Force and the Department of Defense is increasingly interested in nanomaterials. To study these materials, one needs to measure the mechanics of materials on the nanoscale. Over the past few decades the atomic force microscope (AFM) has been used in various methods to establish local surface properties at the nanoscale. In particular, surface elasticity measurements are crucial to understanding nanoscale surface properties. Problems arise, however, when measuring soft surfaces such as polymers and biological specimens, because these materials have a more complex viscoelastic response.

This research focuses on modeling an AFM dynamic nanoindentation experiment intended to characterize near-surface viscoelastic material parameters. The experiment uses an AFM in dynamic contact mode with a polymer surface to gather frequency dependent amplitude and phase data. A three-dimensional, dynamic viscoelastic model of the AFM and surface interaction is developed and then analytically solved in the linear approximation under appropriate physical assumptions based on the physics of the AFM experimental setup. As an illustrative application, the analytical solution is coupled with experimental data from a polystyrene material to ascertain surface material properties at the nanoscale. Our solution allows the direct calculation of the storage and loss modulus from experimental data.

Acknowledgements

First and foremost, I would like to thank Dr. William P. Baker. Without his infinite patience, capable mentoring, and helpful comments and critiques, completion of this dissertation would not have been possible. I would also like to extend my gratitude to the other members of my committee; their assistance was greatly appreciated. Special thanks must certainly go to Dr. Guangming (Alex) Li, whose experiments provided the foundation for my research. Finally, I would like to express my appreciation to my family and my friends, whose patience, encouragement, and unflagging support have been invaluable. Of course, it goes without saying that any and all errors in this document are mine and mine alone.

Jacob B. Goldberg

Table of Contents

Page

List of Figures

Figure Page

List of Tables

Table Page

List of Abbreviations

Abbreviation		Page
AFM	Atomic Force Microscope	1
Piezo	Piezoelectric Crystal	4
LIA	Lock-In-Amplifier	6
JKR	Johnson, Kendall, and Roberts	19
DMT	Derjaguin, Muller, and Toporov	21

AN ANALYTICAL MODEL OF NANOMETER SCALE VISCOELASTIC PROPERTIES OF POLYMER SURFACES MEASURED USING AN ATOMIC FORCE MICROSCOPE

I. Introduction

The United States Air Force and the Department of Defense is increasingly interested in nanomaterials [17]. In order to study these materials, one needs to measure the mechanics of materials on the nanometer scale. With technology's increasing focus on the atomic and molecular level, the importance of nanoscale surface physics and chemistry cannot be understated. Since the invention of the atomic force microscope (AFM) in 1986 [9], there has been substantial growth in its applications. In particular, the AFM has been used to establish local surface properties such as elastic modulus, adhesion, surface friction, viscosity, hardness, energy dissipation, and glass transition temperature [3, 10, 19, 21, 23, 40, 45, 90, 49, 59, 68, 76, 86, 87, 88, 91, 99]. Determining nanoscale surface properties is a challenge at the atomic level because surface materials behave different from the bulk material. Forces such as adhesion and van der Waals bond interactions, which are usually unsubstantial at the macro scale, now become dominant influences. In addition, problems arise when dealing with softer surfaces such as polymers and biological specimens. One reason is because these materials have more complex viscoelastic and even plastic responses. Another important reason is that these materials can have anisotropic responses.

This research focuses on modeling an AFM dynamic nanoindentation experiment on a viscoelastic surface. In the experiment, an AFM in dynamic contact mode with a polymer surface is used to gather frequency dependent amplitude and phase data.

A mathematical model of the experiment is created and, under several appropriate physical assumptions, an analytical solution in the linear approximation is achieved for the penetration depth of the AFM tip into the material. Another model is created that relates the raw experimental data to the depth of penetration of the AFM tip. These two models are then equated to ascertain an analytical solution allowing the calculation of frequency dependent, viscoelastic material properties from the experimental data. As an illustration, viscoelastic properties for a polystyrene material are calculated and presented using the analytical solution.

This chapter is divided into three sections. The first section contains the motivation for this research along with other research that has been performed. The second section gives a brief overview of the experiment that is to be modeled. Finally, we detail what will be presented in the remaining chapters of this document.

1.1 Motivation

The interest of the United States Air Force and the Department of Defense in nanomaterials is of key importance in many areas. In particular, high-altitude long-endurance ISR airships, prompt theater-range ISR/strike systems, direct forward air delivery and resupply, energy-efficient partially buoyant cargo airlifters, fuel-efficient hybrid wing-body aircraft, and hyperprecision low-collateral damage munitions [17]. In order to help further research in these areas, nanoscale viscoelastic material properties are of particular importance. These properties are calculated using both mathematical theory and experiment. Though the experiments widely vary, their mathematical approach remains consistent, that is the movement of the indentation/loading system, whether an AFM or a nanoindenter, is often modeled as a spring-mass system [5, 97, 98]. In addition, the contact model of the indentation/loading system with the material surface is the Sneddon solution [84] extended to the viscoelastic case using the method of functional equations proposed by Lee and Radok [52]. Sneddon's solution is derived from a rigid axisymmetric indenter that is indented into a half-space composed of a homogeneous, isotropic, linearly elastic material. Sneddon's solution is based on the quasi-static equilibrium equations and provides the penetration depth in terms of the indenter's geometry as well as the load imposed on the indenter in terms of its geometry. Using the method of functional equations, Sneddon's solution is extended to the linearly viscoelastic case provided that the contact area of the indenter increases monotonically with time. This extended solution provides a mathematical way of relating monotonically increasing and/or constant load histories to the complex stiffness of a material given a chosen viscoelastic model [67, 81]. The extended solution, along with a particular viscoelastic model, can also be used in specific testing procedures such as the load relaxation test or the creep test, to produce the relaxation modulus or creep compliance, respectively [15, 96, 97].

We model the dynamic nanoindentation experiment in two pieces which, are coupled together using the appropriate boundary conditions. The two pieces of the experimental setup are the AFM and the material. The AFM is modeled as a one-dimensional spring-mass system with three driving forces. The driving forces consist of the static and sinusoidal forcing provided by the AFM system, and the force on the tip caused from the stress within the surface. The latter force serves to couple the AFM with the material. The modeling of the AFM as a spring-mass system is similar to current AFM modeling theory [53, 95].

The material is modeled based on continuum mechanics using a three-dimensional, linear viscoelastic material model. The generated equations are the elastodynamic equilibrium equations, i.e., they contain an inertial term. This clearly differs from the current theories which are based upon the quasi-static equilibrium equations [15, 56, 58, 67, 81, 96]. An axisymmetric indenter, representing the AFM tip, is applied to the surface of the material. The application of the indenter is such that there is a static indentation superposed with a much smaller sinusoidally varying indentation. This represents the nature of the experiment in that the driving force from the system contains a static loading which is far greater than the dynamic loading. The related equations are then analytically solved in the linear approximation under the assumption that the static loading far exceeds the dynamic loading. The analytic solution is in terms of the penetration depth of the indenter into the material.

A model that relates the raw experimental data to the penetration depth of the AFM tip is then equated to the analytical solution from the material model. This allows for the calculation of the frequency dependent storage and loss modulus based on a generic viscoelastic polynomial model. Our solution allows the direct calculation of the storage and loss modulus from experimental data. A specific viscoelastic model can then be chosen to fit the data as accurately as possible in order to attain specific material parameters. This differs from current solutions in that current solutions have to choose a viscoelastic model before the storage and loss modulus are calculated [15, 67, 81, 96]. Thus, our model allows for a more varied approach to choosing a viscoelastic material model.

This concludes the overview of the motivation for our research. The next section gives an overview of the experimental setup and procedure.

1.2 Experimental Setup

The experiment we are concerned with uses an AFM as a dynamic indentor in order to glean nanomechanical properties of a sample surface. The representation of the experimental setup can be seen in Figure 1. In the experiment, the AFM cantilever tip is moved toward the sample surface by expansion of the piezoelectric crystal (Piezo). The considered sample consists of a polystyrene layer bonded to a

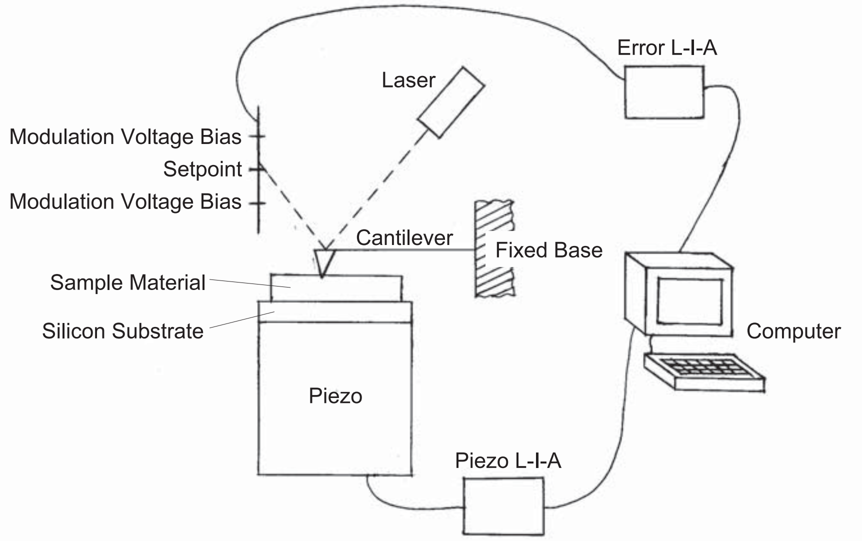

Figure 1. A simplified model of the experimental setup.

silicon base. The silicon base rests atop a piezo. A voltage is applied to the piezo, which causes the crystal to expand thus raising the sample's surface into the AFM tip. This voltage is the DC component of the piezo drive signal. Since the surface is viscoelastic, there is some initial creep, but after a set amount of time, the system approaches an equilibrium position.

A laser beam is continuously reflected off the tip end of the cantilever and onto a detector. The initial voltage measured at the detector is called the preload voltage, or the static load. The preload voltage is considered the setpoint of the experiment. It is the voltage which corresponds to a cantilever position around which the cantilever will be oscillating. This voltage is considered to be the initial start point or zero point.

A manual bias is set on the detector. The voltage of this manual bias is called the modulation voltage or forcing amplitude, and its phase is the forcing frequency or tapping frequency. This forcing never changes and is also our reference amplitude and phase. A closed-loop, computer controlled feedback system modifies the modulation voltage and phase in an attempt to maintain the setpoint within the modulation voltage bias. The total signal that is input to the piezo is called the piezo drive signal. A lock-in-amplifier (LIA), which we call the AC component of the piezo drive signal, measures the exact piezo voltage input and phase. The piezo LIA records a continuous measurement for all tapping frequencies.

The piezo drive signal forces the piezo to oscillate at a fixed frequency and amplitude, causing the movement of the surface relative to its initial position to be of an oscillatory nature. Since the piezo is a crystal, it takes a set amount of time to contract or expand to the voltage that is applied to it. This delay in contraction or expansion is called the *piezo delay time*, which is in this case frequency dependent. Consequently, the oscillatory nature of the surface's relative position occurs at the piezo drive signal, but it is phase delayed by the piezo delay time.

As the surface's relative position oscillates, it interacts with the AFM tip and causes the tip to move in an oscillating pattern. This tip movement is not at the same amplitude or phase as the piezo drive signal nor is it at the same amplitude and phase as the modulation voltage. The interaction between the soft sample surface and the harder AFM tip creates a smaller voltage amplitude and an additional delay time, called the *viscoelastic retardation time*, which is manifested in the AFM cantilever tip's relative motion. The difference between the actual AFM tip movement and the piezo modulation voltage is measured by a lock-in-amplifier. We call this the error LIA. The error LIA continuously measures the AC amplitude and phase difference for all tapping frequency.

This procedure is performed through a sweep of tapping frequencies from 1000 Hz to 1 Hz, allowing equilibrium to be reached at each frequency. After sweeping through all the frequencies, the process is started over with a new preload voltage. Between ten and fifteen different preload voltages are used, ranging from 0.25 V to

5.4 V. The same experiment is also performed using polystyrene samples of differing thickness: 30 nm, 70 nm, and 220 nm.

This concludes the discussion on the experimental setup. Our focus will be to mathematically model the above procedure as closely as possible. Through our proceedings we will make simplifying assumptions based on the physics of the experiment in order to achieve an analytical solution but, we will maintain the pertinent physics needed to fully describe the experiment. The next section of this chapter will detail the contents contained in the remainder of this dissertation.

1.3 Dissertation Contents

Chapter one contains an introduction to nanoscale material modeling, as well as a description of the experiment and the mathematical model that we will produce. Chapter two includes a description of AFM modeling theories and the formulation of a one-dimensional spring-mass model that represents the AFM cantilever. In Chapter three we present material modeling theories and create a three-dimensional, viscoelastic material model. The one-dimensional AFM model and the three-dimensional material model are then nondimensionalized. In Chapter four, we present necessary background material and then proceed to make physical assumptions that allow us to simplify the three-dimensional, viscoelastic material model, as well as the one-dimensional AFM model. This reduced three-dimensional system is then analytically solved in the linear approximation, and analyzed. Chapter five includes the creation of a model that describes how the data was collected. This new model is then coupled to the reduced three-dimensional model; and in conjunction with the experimental data, a method for determining viscoelastic material properties is produced. Finally, Chapter six draws conclusions and investigates areas for future work.

II. The AFM

Atomic force microscopy techniques have been around since its invention in 1986 [9]. Various techniques have been developed ranging from measuring surface details to modifying surface structures. This chapter focuses on aspects of AFM modeling theory and how the AFM can be coupled to the surface it is in contact with. The chapter ends by choosing an AFM model with the appropriate surface contact model.

2.1 AFM Modeling Theories

The process of modeling how dynamic atomic force microscopy techniques are used to determine surface properties, allows us to gain a better understanding of the mechanical properties of the surface at the nanoscale. An AFM is an instrument used to produce high resolution, three-dimensional images of sample surfaces on a nanometer scale. Using a scanning technique the AFM is capable of measuring small forces between the AFM tip and the sample surface.

The AFM tip is mounted on a cantilevered beam having a very small mass. As the tip is scanned across the surface, the cantilevered beam flexes based on the surface topology. The flexing motion can be measured using a variety of techniques including optical deflection, optical interference, capacitance, and tunneling current. All of these techniques can be used to produce an image of the sample surface. As an example, Figure 2 shows a topographical image of nanodots on a polystyrene surface using an AFM with a silicon nitride tip [54].

Beyond the basic physics of a cantilever system and its forcing, there are three major methods to model the forces that occur between the AFM tip and the sample surface. The first method is to model the tip surface interaction by means of a potential function. A potential function is a molecular model with two terms; one term

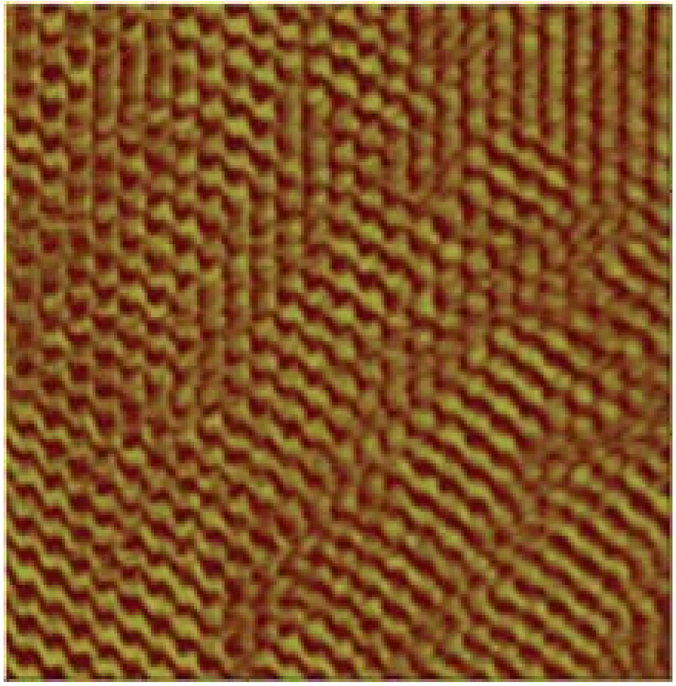

Figure 2. A sample topographical image of nanodots created on a polystyrene surface.

represents the adhesive potential, and one term represents the repulsive potential between two molecules. It is a simple mathematical model that describes the interaction force between two molecules based on how far apart they are. An example of a potential function is the Lennard-Jones potential, which is also called the 6-12 potential. It can be written as $V(r) = \frac{A}{r^{12}} - \frac{B}{r^{6}}$, where r is the distance between molecules, and A and B are constants based on properties of the molecular interactions [4].

The second method is a macroscopic method that does not explicitly consider atomic scale forces. This method is by modeling the surface adhesion between the tip and the surface, or between the tip and the small layer of condensed water on the surface [78]. The third method is a continuum model that uses the stress that is induced within the material by the movement of the AFM tip in contact with the surface. This stress exerts a force back onto the AFM tip. The effects of one of these methods to model tip to surface interactions, combined with the properties of the surface material and the basic physics of the cantilever system lead to the ability to measure surface material properties. Therefore, we must choose the most applicable method to model the interactions in order to capture material properties.

2.1.1 Cantilever Beam Model With A Surface Potential.

An AFM cantilever can be represented by the shape of a rectangular beam with a length L, a width w ($w \ll L$), a thickness h ($h \ll L$), and a tip length of L_{tip}. We will set up the coordinate system as in Figure 3. Since forces can occur in any direction, the cantilever tip can deflect in any direction. We will let the displacement of the beam be represented by $\vec{u}(t, x, y, z)$, where $\vec{u} = [u_x, u_y, u_z]^\top$. The terms u_x, u_y, and u_z represent the displacement in the x, y, and z-directions, respectively.

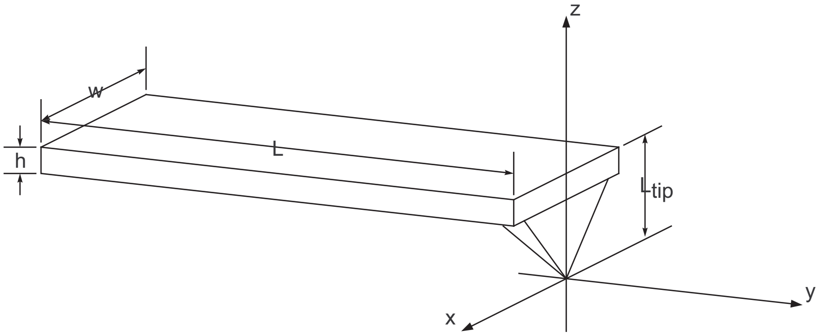

Figure 3. The model cantilever and the coordinate system.

The cantilever tip movement is driven by the forces that act upon it and its response to these forces. In order to study the cantilever tip movement, we must first look at the elastic properties of the cantilever. Although the cantilever has three degrees of freedom, for our simple model, we will only concern ourselves with the cantilever movement in the z-direction. Thus, we only need the elastic property of the stiffness in the z-direction, k. So, we will make the following assumptions. First, we will deal only with static beam loading. Next, we will assume that there is a vertical point force, F_z, applied downward at the centroid of the beam at the cantilever tip end. This assumption means that there is no beam displacement in the x-direction. Though there is an indirect displacement in the y-direction from the bending of the cantilever in response to the vertical force, this displacement is of a very small magnitude, and we will assume that its contribution is negligible compared to the displacement in the z-direction. Therefore, $\vec{u}(t, x, y, z)$ can be represented by $u_z(x, y, z)$. The coordinates $(0, 0, 0)$ represent the center of the thickness and the width of the beam at the clamped end of the beam.

Since the cantilever is only bending a very small amount in the vertical direction and it behaves as a linear-elastic material, the cantilever follows Hooke's Law. This states, $F_z = ku_z$, and from Saada [77], we obtain the formula

$$k = \frac{Ewh^3}{4L^3}, \tag{1}$$

where E is the Young's modulus of elasticity for the cantilever material.

To ensure that our model includes all of the important physics of the AFM, we will calculate the natural frequency of the cantilever. We will assume that our cantilever is isotropic and has a constant mass density with mass m. Drawing again from Saada, we see that a statically-loaded cantilever deflected under a vertical load at the free end, obeys the equation

$$u_z(0, y, 0) = \frac{2F_z}{Ewh^3}(3L - y)y^2. \tag{2}$$

This equation is for a cantilever under plane stress, and the coordinates $(0, y, 0)$ represent the center of the thickness and the width of the beam. Also, $y = 0$ represents the clamped end of the beam, and $y = L$ represents the free end. Equation (2) assumes the boundary conditions, $u_z(0, 0, 0) = 0$ and $\frac{du_z}{dy}(0, 0, 0) = 0$. From here on, we will let $u_z(0, y, 0) = u_z(y)$. So, the cantilever deflection at the free end is

$$u_z(L) = \frac{4F_z L^3}{Ewh^3}. \tag{3}$$

This leads to

$$u_z(y) = \frac{u_z(L)}{2}\left(3\left(\frac{y}{L}\right)^2 - \left(\frac{y}{L}\right)^3\right). \tag{4}$$

If we consider F_z slowly varying with time, then the static beam Equation (4) captures the dynamic behavior as

$$u_z(t, y) = \frac{u_z(t, L)}{2}\left(3\left(\frac{y}{L}\right)^2 - \left(\frac{y}{L}\right)^3\right). \tag{5}$$

We will next calculate the kinetic energy, E_k, and potential energy, E_p, of the cantilever. First we consider an infinitesimal beam element dy a distance y from the clamped end. The infinitesimal kinetic energy of such a beam element is described by the equation

$$dE_k = \frac{1}{2}m(\dot{u}_z(t, y))^2\frac{dy}{L}, \tag{6}$$

where the dot is a derivative with respect to time. Substituting Equation (5) into Equation (6) and integrating over the length of the cantilever produces

$$E_k = \int_0^L \frac{1}{2}m(\dot{u}_z(t, y))^2\frac{dy}{L} = \frac{33}{140}\frac{m}{2}(\dot{u}_z(t, L))^2. \tag{7}$$

Since the point force F_z acts only on the free end of the cantilever, E_p is equal to the work needed to move the free end of the cantilever a distance $u_z(t, L)$. Thus,

$$E_p = \int_0^{u_z(t,L)} F_z du_z = \int_0^{u_z(t,L)} k u_z du_z = \frac{k u_z^2(t, L)}{2}. \tag{8}$$

The total energy of the system, W, is equal to the sum of the kinetic and potential energies. If we assume that the cantilever vibrations occur without energy dissipation then W is constant. If we differentiate W with respect to time under this assumption, and then divide through by $\dot{u}_z(t, L)$, we arrive at

$$\frac{33m}{140}\ddot{u}_z(t, L) + ku_z(t, L) = 0, \tag{9}$$

which is the equation of movement for the free end of the cantilever.

Let $M = \frac{33m}{140}$ represent the effective mass of the cantilever. We will suppress the L and subscript z symbols and let $u(t) = u_z(t, L)$. Making the above substitutions in Equation (9) gives

$$M\ddot{u}(t) + ku(t) = 0. \tag{10}$$

Furthermore, the natural frequency of the cantilever is $\omega_0 = \sqrt{\frac{k}{M}}$.

Next, we examine the force of internal damping within the cantilever itself. The internal damping is caused mainly by internal interatomic friction. At small velocities of oscillation, v, the force of internal damping is modeled proportional to the velocity itself, i.e., $F_d = -\beta_0 v = -\beta_0 \dot{u}$, where β_0 is a positive constant. When the force of internal damping is included in Equation (10) we obtain

$$M\ddot{u} + \beta_0\dot{u} + ku = 0. \tag{11}$$

Dividing Equation (11) by M and make the substitution $\delta = \frac{\beta_0}{2M}$, we arrive at

$$\ddot{u} + 2\delta\dot{u} + \omega_0^2 u = 0. \tag{12}$$

The quality factor of the system, or Q-factor, is a dimensionless parameter that is related to the loss within the AFM cantilever itself [8]. It is proportional to the ratio of the stored energy of a system, $E(t)$, versus the energy lost in that system over a period of time T. If $\triangle E_T = E(t) - E(t+T)$, then it is positive when energy is dissipated. The Q-factor characterizes the rate of energy transformation in the cantilever, and is defined by

$$Q = \frac{2\pi E(t)}{\triangle E_T}. \tag{13}$$

When there is very little internal damping ($\omega_0 \gg \delta$) the total energy of the system is

$$E(t) = E_i e^{-2\delta t}, \tag{14}$$

where $E_i = \frac{1}{2} M \omega_0^2 Z^2$ is the initial magnitude of the stored energy in the system and

$$Z = \sqrt{u^2(0) + \left(\frac{\dot{u}(0) + \delta u(0)}{\sqrt{\omega_0^2 - \delta^2}} \right)^2}. \tag{15}$$

Now, by combining Equations (13) and (14) and expanding the exponential function, we get

$$Q = \frac{2\pi}{1 - e^{-2\delta T}} = \frac{2\pi}{1 - (1 - 2\delta T + 2(\delta T)^2 + \cdots)} \approx \frac{\pi}{\delta T} = \frac{\Omega}{2\delta} \approx \frac{\omega_0}{2\delta}, \tag{16}$$

where $\Omega = \frac{2\pi}{T} = \sqrt{\omega_0^2 - \delta^2}$ and $\delta T \ll 1$. Therefore, the Q-factor defines the internal damping of the oscillations in the system. Thus, Equation (11) can be rewritten as

$$M\ddot{u} + \frac{M\omega_0}{Q}\dot{u} + ku = 0. \tag{17}$$

Now, we need to add the oscillations of the cantilever into the model. There are three main methods to create the cantilever tapping. The first method is by tuning the feedback control voltage on the AFM piezo crystal near the ringing conditions. The second is by applying an alternating voltage to the piezo crystal in the z-direction. The third method is to illuminate the cantilever with a modulated laser at appro-

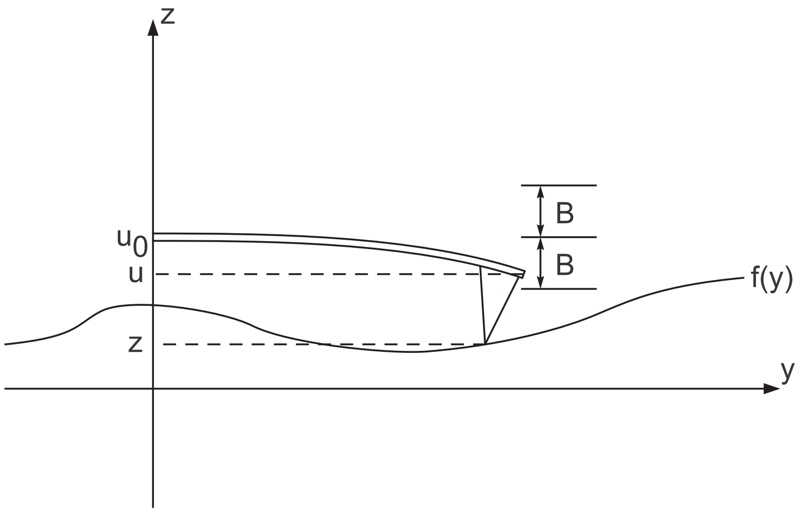

Figure 4. The 2-dimensional cantilever system with a free end oscillation of $B\sin(\omega t)$.

priate frequencies. For the sake of simplicity, all of the preceding methods can be mathematically represented by $B\sin(\omega t)$, where B is the amplitude of oscillation and ω is the frequency of oscillation.

If we oscillate the free end of the cantilever, and we translate the coordinate system by shifting the beam in the positive z-direction a distance u_0, as shown in Figure 4, we get the free end displacement equation

$$M\ddot{u} + \beta_0\dot{u} + ku = k(u_0 + B\sin(\omega t)). \tag{18}$$

Next, we will assume that the height of the surface can be represented by the function $f(y)$ as shown in Figure 4. We will also assume that the surface has a potential, V, that is homogeneous in the y-direction, i.e., the potential only depends on the height above the surface and not on the location along the surface. We are adding a potential into the model in order to obtain a parameter to control the interaction force between the beam tip and the surface. This force can come from a number of sources including molecular attractions and repulsions. We note that $-\nabla V$ is the force from the potential but, the only pertinent force for our equation is that which is in the z-direction. Thus, adding the force from this potential to Equation (18) gives

$$M\ddot{u} + \beta_0\dot{u} + ku = k(u_0 + B\sin(\omega t)) - V'(u - u_0 - f(y)), \tag{19}$$

where the prime means the derivative with respect to the argument.

Since we are only interested in the movement at the tip, we will make the substitution, $u(t) = y(t) + L_{tip}$, where L_{tip} is the length of the AFM tip. Note, that $\dot{u} = \dot{y}$ and $\ddot{u} = \ddot{y}$. Thus, the equation of tip motion is

$$M\ddot{y} + \beta_0\dot{y} + k(y + L_{tip}) = k(u_0 + B\sin(\omega t)) - V'(y(t) + L_{tip} - u_0 - f(y)). \tag{20}$$

We will now make the assumption that our cantilever tip is always in direct contact with the surface, which means that $u_0 = L_{tip}$. Making this substitution into Equation (20) and rearranging terms yields

$$M\ddot{y} + \beta_0\dot{y} + ky = kB\sin(\omega t) - V'(y(t) - f(y)). \tag{21}$$

Equation (21) is the one-dimensional, simplified equation of motion for the AFM movement with a potential function.

The initial conditions are chosen so that the tip has no initial displacement and no initial velocity, i.e., $y(0) = \dot{y}(0) = 0$. This means the surface, $f(y)$, is assumed to pass through the point $(y, z) = (0, 0)$. Now, divide Equation (21) by M, and substitute

$\beta_0 = \frac{M\omega_0}{Q}$ and $\omega_0 = \sqrt{\frac{k}{M}}$. This yields

$$\ddot{y} + \frac{\omega_0}{Q}\dot{y} + \omega_0^2 y = \omega_0^2 B \sin(\omega t) - \frac{1}{M}V'(y(t) - f(y)). \tag{22}$$

Next, introduce the dimensionless time, $\tau = \omega_0 t$, and define the new dependent variable $x(\tau) = y(t)$. Note that $\dot{y} = \omega_0 \dot{x}$ and $\ddot{y} = \omega_0^2 \ddot{x}$, where the dot is differentiation with respect to the argument. After making this change of variables, and dividing through by ω_0^2, we obtain

$$\ddot{x}(\tau) + \frac{1}{Q}\dot{x}(\tau) + x(\tau) = B \sin\left(\frac{\omega}{\omega_0}\tau\right) - \frac{1}{k}V'\left(x(\tau) - f(y)\right). \tag{23}$$

Further, the initial conditions become $x(0) = \dot{x}(0) = 0$, and are still quiescent.

Equation (23) with the above initial conditions can be converted to a nonlinear Volterra integral equation of the second kind. In Equation (23) we assume that $Q > \frac{1}{2}$, which is feasible because as we saw earlier in Equation (16), $Q \approx \frac{\pi}{\delta T}$, where $\delta T \ll 1$. Hence, our integral equation is

$$x(\tau) = \int_0^\tau \frac{1}{\sqrt{1 - (1/2Q)^2}} F(x(\xi), \xi) e^{\frac{-1}{2Q}(\tau - \xi)} \sin\left(\sqrt{1 - (1/2Q)^2}(\tau - \xi)\right) d\xi, \tag{24}$$

where

$$F(x(\xi), \xi) = B \sin\left(\frac{\omega}{\omega_0}\xi\right) - \frac{1}{k}V'\left(x(\xi) - f(y)\right). \tag{25}$$

Equations (24) and (25) represent the cantilever tip position in terms of an oscillating forcing function and a potential function. We will now proceed to look at modeling the tip to surface interaction through adhesive forces.

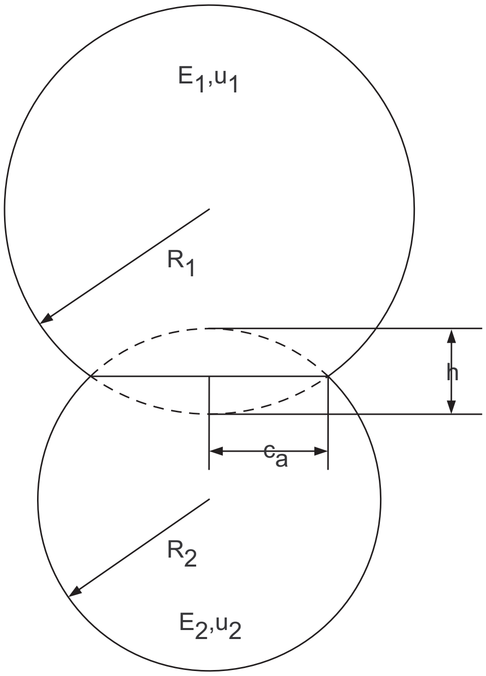

Figure 5. A diagram of the contact of two spheres.

2.1.2 Surface Adhesion.

Another method to model the AFM tip's interaction with the surface is through adhesion. Adhesion is when two surfaces in contact with each other, stick together based on the differing nature of their materials. There have been several different surface adhesion theories developed. The major difference between these theories is the way in which they idealize the contact interaction between two surfaces.

Before contending with adhesive models, we will examine the Hertz model for the contact between two curved surfaces. The Hertzian contact model [39] was developed by Heinrich Hertz in 1882. It models the contact stresses and deformation that occur when two curved surfaces are pressed together under a constant loading. The model assumes that the deformation of the two surfaces is small compared to their radii of curvature, and that the materials of the two surfaces are isotropic and elastic. An elastic isotropic material means that the material has properties that are identical in any direction, and each material can be described by only two elastic parameters.

The Hertzian contact model says that the penetration depth, h, is equal to the square of the contact area radius, c_a, divided by the effective radius, $R = \frac{R_1 R_2}{R_1 + R_2}$. This gives

$$h = \frac{c_a^2}{R}, \tag{26}$$

where R_1 and R_2 are the radii of each of the spheres. A diagram of this is shown in Figure 5. Hertz also related the loading force, F, to the contact area radius by

$$F = \frac{\kappa c_a^3}{R}, \tag{27}$$

where κ is the effective Young's modulus of the two materials. The effective Young's modulus, κ, can be calculated from the equation

$$\frac{1}{\kappa} = \frac{3}{4}\left[\frac{1-\mu_1^2}{E_1} + \frac{1-\mu_2^2}{E_2}\right], \tag{28}$$

where μ_1 and μ_2 are the Poisson's ratios of each of the spheres, and E_1 and E_2 are the Young's moduli of the spheres. The Hertz model is an elastic model which does not contain adhesion. So, with this model as our basis, we will now turn our focus toward adhesive models.

Johnson, Kendall, and Roberts (JKR) [48] used an energy balance approach to create the first model of adhesive forces between two elastic spheres. The force of adhesion, F_{adh}, can be written as

$$F_{adh} = \frac{\kappa c_a^3}{R} - \sqrt{6\pi W_a \kappa c_a^3}, \tag{29}$$

where $R = \frac{R_1 R_2}{R_1 + R_2}$ is the effective radius, κ is the effective Young's modulus, W_a is the work of adhesion, and c_a is the contact area radius. The effective Young's modulus, κ, is defined by Equation (28). It is important to note that c_a is parametrically defined by Equation (29) and the equation

$$h = \frac{c_a^2}{R} - \frac{2}{3}\sqrt{\frac{6\pi W_a c_a}{\kappa}}, \tag{30}$$

where h is the penetration depth.

The work of adhesion is defined as

$$W_a = \gamma_1 + \gamma_2 + \gamma_{12}, \tag{31}$$

where γ_1 and γ_2 are the surface energies of the two adhering spheres, and γ_{12} is the interfacial energy between the two spheres. Surface energy is a material property that is defined as the minimum energy per unit area to form a surface from the bulk. Higher surface energies indicate stronger intermolecular forces. The interfacial energy between two solids is the energy between the interface of the two solids per unit area. While surface energies are easier to measure, the interfacial energies depend on what two surfaces are adhering and are much harder to obtain. Therefore, we often estimate the work of adhesion. Berthelot [80] used the geometric mean to estimate the work of adhesion as

$$W_a \approx \sqrt{W_{11} W_{22}}, \tag{32}$$

where W_{11} and W_{22} are the works of cohesion of the two solids. The work of cohesion is the work per unit area to break the bonds of a solid with itself. So, $W_{11} = 2\gamma_1$ and $W_{22} = 2\gamma_2$. Thus, Equation (32) can be rewritten as

$$W_a \approx 2\sqrt{\gamma_1 \gamma_2}. \tag{33}$$

The JKR model applies to tips with large radius of curvature and cantilevers of small stiffness. The model works well for highly adhesive systems [34]. The surface forces involved within the JKR model act only within the contact area and include the influence of van der Waals' forces. The model is based on the assumption that the cohesive zone is infinitesimally small. The cohesive zone is the area just outside the region of contact that is subjected to adhesive traction.

Later, Derjaguin, Muller, and Toporov (DMT) [18] also solved the problem of the adhesive forces between two elastic spheres. The force of adhesion for DMT can be written as

$$F_{adh} = \frac{\kappa c_a^3}{R} - 2\pi R W_a, \tag{34}$$

where all the quantities are defined the same as in JKR except the contact area radius, c_a, which is simply defined as

$$c_a = \sqrt{hR}. \tag{35}$$

The DMT model applies to tips with small radius of curvature and cantilevers of high stiffness. The model works well for low adhesion systems [34]. The surface forces involved within the DMT model act only outside the contact area and do not include the influence of van der Waals' forces.

Maugis [62] then showed that JKR and DMT were on opposite sides of the solution spectrum, and he also came up with an analytical solution to span the transition from JKR to DMT. The Maugis solution can be applied to any system spanning the high to low adhesion range. The amount of adhesion is determined by the parameter

$$\lambda = \frac{2.06}{\xi_0} \left(\frac{R {W_a}^2}{\pi \kappa^2} \right)^{\frac{1}{3}}, \tag{36}$$

where ξ_0 is the equilibrium interatomic distance between the two spheres. As $\lambda \to 0$ the system adhesion decreases and the stiffness of the materials increases so, the model behaves like DMT. As $\lambda \to \infty$ the system adhesion increases and the materials become more compliant so, the model behaves like JKR. Maugis' model assumes that the adhesion force acts within an annulus at the contact area border.

Now, we will go back to Equation (21). From here we will insert the force of adhesion from JKR in place of the potential function. Since, we are dealing with the cantilever tip radius in contact with a surface which when compared to the cantilever tip, can be taken to be flat, i.e., $R_2 = \infty$, then $R = R_1$. Including the force of adhesion in the one-dimensional AFM model produces

$$M\ddot{y} + \beta_0\dot{y} + ky = kB\sin(\omega t) + \frac{\kappa c_a^3}{R} - \sqrt{6\pi W_a \kappa c_a^3}. \tag{37}$$

To solve this equation, we will proceed as we did in the last section. First, we are going to choose the same initial conditions, i.e., $y(0) = \dot{y}(0) = 0$. Next, we need to divide through by M in Equation (37) and make the substitutions $\beta_0 = \frac{M\omega_0}{Q}$ and $\omega_0 = \sqrt{\frac{k}{M}}$. This gives

$$\ddot{y} + \frac{\omega_0}{Q}\dot{y} + \omega_0^2 y = \omega_0^2 B\sin(\omega t) + \frac{\kappa c_a^3}{MR} - \frac{1}{M}\sqrt{6\pi W_a \kappa c_a^3}. \tag{38}$$

Now, we introduce the dimensionless time, $\tau = \omega_0 t$, and define the new dependent variable $x(\tau) = y(t)$. After making this change of variables, and dividing through by ω_0^2, we arrive at

$$\ddot{x}(\tau) + \frac{1}{Q}\dot{x}(\tau) + x(\tau) = B\sin\left(\frac{\omega}{\omega_0}\tau\right) + \frac{\kappa c_a^3}{kR} - \frac{1}{k}\sqrt{6\pi W_a \kappa c_a^3}, \tag{39}$$

where $\dot{x} = \frac{dx}{d\tau}$ and the initial conditions become $x(0) = \dot{x}(0) = 0$.

Equation (39) with the above initial conditions converts to a nonlinear Volterra integral equation of the second kind. While solving Equation (39) we again assume that $Q > \frac{1}{2}$, and our integral equation emerges as

$$x(\tau) = \int_0^\tau \frac{1}{\sqrt{1-(1/2Q)^2}} F(x(\xi),\xi) e^{\frac{-1}{2Q}(\tau-\xi)} \sin\left(\sqrt{1-(1/2Q)^2}(\tau-\xi)\right) d\xi, \quad (40)$$

where

$$F(x(\xi),\xi) = B\sin\left(\frac{\omega}{\omega_0}\xi\right) + \frac{\kappa c_a^3}{kR} - \frac{1}{k}\sqrt{6\pi W_a \kappa c_a^3}. \quad (41)$$

We must also remember that we will need to simultaneously satisfy the equation

$$h = f(y) - x(\tau) = \frac{c_a^2}{R} - \frac{2}{3}\sqrt{\frac{6\pi W_a c_a}{\kappa}}, \quad (42)$$

as well. Here, $f(y)$ represents the height of the surface at the current cantilever tip position as shown in Figure 4.

Equations (40)-(42) represent the cantilever tip position in terms of an oscillating forcing function and adhesion defined by JKR. We will now proceed to look at modeling the tip to surface interaction through surface stresses.

2.1.3 Surface Stress and Deformation.

The final method of producing a model of the AFM is to include the stress the surface induces on the AFM tip and the resulting surface deformations. As the AFM tip contacts the surface, it generates a stress, σ, in the surface based on the magnitude and direction of the force caused by the tip. Stress is an applied force per unit area that causes a deformation per unit length, or strain ϵ, in a body. The stress generated is what causes the surface to deform. This surface deformation generates a force, $F_\sigma(t)$, on the AFM tip as illustrated in Figure 6. This leads to the one-dimensional AFM equation

$$M\ddot{y} + \beta_0\dot{y} + ky = kB\sin(\omega t) + F_\sigma(t). \quad (43)$$

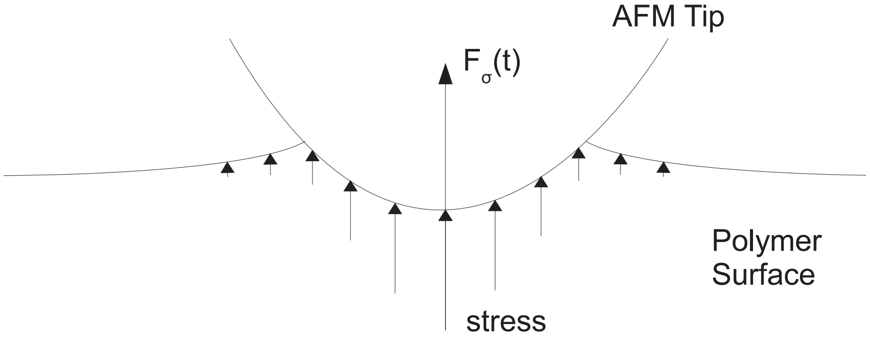

Figure 6. Surface stress within the material, and the resulting force vector on the AFM tip.

The force F_σ includes the viscoelastic surface forces as well as the adhesion forces. This force serves to couple the AFM model with the material model, and is highly dependent on the geometry of the AFM tip. It can be represented by

$$F_\sigma(t) = \int_0^{2\pi} \int_0^{\infty} \sigma_{zz}(r, \theta, z, t) \bigg|_{z=0} r dr d\theta. \tag{44}$$

Here, $\sigma_{zz}(r, \theta, z, t)$ represents the surface stress normal to the z-direction in cylindrical coordinates. The reason we only include the surface forces in the z-direction is because this is a one-dimensional representation of the AFM so, only the forces in that direction affect the model.

For the general viscoelastic constitutive case [16, 57],

$$\begin{aligned} \sigma_{zz}(r, \theta, z, t) = \int_{-\infty}^{t} [\lambda(t-\tau) + 2\mu(t-\tau)] \frac{\partial}{\partial \tau} \left[\frac{\partial u_z}{\partial z} \right] d\tau \\ + \int_{-\infty}^{t} \lambda(t-\tau) \frac{\partial}{\partial \tau} \left[\frac{\partial u_r}{\partial r} + \frac{u_r}{r} + \frac{1}{r} \frac{\partial u_\theta}{\partial \theta} \right] d\tau, \end{aligned} \tag{45}$$

where u_r, u_θ, and u_z are each functions of r, θ, z, and t. They represent the linear displacement of the surface at a given point, in each of their respective directions.

The displacement is written in vector notation as

$$\vec{u}(r,\theta,z,t)=\begin{bmatrix} u_r(r,\theta,z,t) \\ u_\theta(r,\theta,z,t) \\ u_z(r,\theta,z,t) \end{bmatrix}. \tag{46}$$

The Lamé constants, $\lambda(t)$ and $\mu(t)$, represent the viscoelastic properties of the surface. Their time dependence means that their past history affects their current values.

2.2 Choosing the AFM Model

Now that we have discussed the differing methods to represent the AFM's interaction with the material, we can choose an appropriate model to represent the experiment and the material parameters. The AFM model is coupled to the material model by way of the force generated by the stresses within the material. So, we will generalize Equation (43) a little further. Since, the experiment consists of a static preload and a dynamic forcing, we will introduce a static forcing displacement, $\hat{B}_0$, to represent the displacement from the preload, and define $\hat{B}$ to be the dynamic forcing amplitude. In addition, we will introduce a phase shift, ϕ, that will be defined later. The phase shift occurs because the stress waves move at differing rates in different materials. So, the AFM model equation we will use is

$$M\ddot{y}+\beta_0\dot{y}+ky=k\left[\hat{B}_0+\hat{B}\sin\left(\omega t+\phi\right)\right]+F_\sigma(t). \tag{47}$$

In summary, this chapter presented a mathematical way to represent the AFM as a simple, spring-mass system. We then discussed three possible methods to model the interaction of the AFM tip with the sample surface. When this interaction was modeled as either a potential function or an adhesive force, an analytical solution in the form of a Volterra integral equation of the second kind was found for the spring-mass system. When the interaction is modeled as a balance of forces caused by the stress in the material, then we must couple the AFM equation to a material model equation. This method allows the most freedom to solve for particular model parameters and to compare with the experimental data. Thus, the AFM model coupled to a material model will be used to model the experiment.

III. The Material

As a material is acted upon by outside forces, structural changes and effects take place on and within the material. These changes are based upon the magnitude and direction of the forces, as well as the properties of the material itself. This chapter will present the different models of material behavior under load. Then, a general three-dimensional model of a viscoelastic material with boundary conditions is created to match with the experiment. The model is non-dimensionalized to more easily identify properties from, and work with, the equations.

3.1 Material Behaviors

Materials can demonstrate three main types of behavior. These behaviors occur under differing loading conditions. The material behaviors can be classified as elastic, plastic, and viscoelastic. We call a material an elastic material, a plastic material, or a viscoelastic material, if the material exhibits that type of behavior. A material may exhibit more than one type of material behavior depending on the loading. When a load is applied to a material that behaves elastically, the material exhibits an immediate strain. When the load is removed, the strain is immediately removed from the material. We say a material is plastic if it exhibits strain when a stress is applied but, when the stress is removed, some of the strain remains permanently. Plastic deformation is defined to be independent of time [24]. The third material behavior is viscoelasticity. A viscoelastic material exhibits an initially elastic response upon loading but, as time goes on, there is a slow and continuous increase of strain. When the loading is removed, the strain immediately decreases but, not to zero. The strain then continuously decreases from there but, may never fully recover, leaving some permanent deformation. It is important to note that viscoelastic materials are very time dependent. The longer a load is applied, the more strain that will occur in the material, and the longer the material will take to recover after the load is removed.

For this research, the dynamic nanoindentation experiment only deals with polymers as the sample surface. Since polymers behave viscoelastically, we will primarily concern ourselves with the modeling of these material behaviors. As the AFM tip moves while in contact with a viscoelastic surface, the surface continually deforms. This deformation of the surface is the primary cause of the stress within the material. Because of the time dependent nature of the material, and the time dependent position of the tip, the stress field within the material continually changes.

In order to ensure that we can generate an analytical model, we will only focus on linear material models. Linear material models have been shown to be useful in modeling the mechanics of some materials [24]. Many materials behave linearly, or nearly linearly, under small amounts of stress. A material is considered to be linear if, at a given time, stress is proportional to strain, and the principle of linear superposition holds.

Linear viscoelastic models can be represented as being made up of two types of elements, linear springs and/or linear viscous dashpots. In these models, inertial effects are neglected. A linear spring has the form

$$\sigma(t) = E\epsilon(t), \tag{48}$$

where E is the Young's modulus constant of the viscoelastic material. The value of E can also be interpreted as a linear spring constant. A linear viscous dashpot takes the form

$$\sigma(t) = \eta\dot{\epsilon}(t), \tag{49}$$

where η is the constant coefficient of viscosity of the viscoelastic material, and $\dot{\epsilon}$ is the time derivative of the strain, ϵ. Viscosity is the measure of the resistance of a fluid to deformation.

Two simple, linear, viscoelastic material models, are the Maxwell model and the Kelvin-Voigt model [24]. The Maxwell model consists of two elements connected in series. It contains both a linear spring and a linear viscous dashpot. This model is written as

$$\dot{\epsilon} = \frac{\dot{\sigma}}{E} + \frac{\sigma}{\eta}. \tag{50}$$

The Maxwell model has no time dependent recovery, meaning when the stress is removed, the linear spring element goes to zero but, the linear viscous dashpot remains, and is constant. This means that there is an instantaneous recovery to a state of permanent strain after the load is removed.

The Kelvin-Voigt model consists of the same two elements in parallel. It can be written as

$$\dot{\epsilon} + \frac{E}{\eta}\epsilon = \frac{\sigma}{\eta}. \tag{51}$$

This model does not describe permanent strain after unloading, meaning that when the load is removed, the material eventually fully recovers. This model also does not describe the instantaneous strain when a material is loaded and the instantaneous partial relaxation when the load is removed.

Burgers later combined a Kelvin-Voigt and a Maxwell model in series to create a four element model [24]. Zener also created a similar, three element model, called the linear standard solid model [24]. He did this by combining a linear spring and a linear viscous dashpot in parallel, and then he combined that system in series with another linear spring. There are also several other three and four element models. The Kelvin-Voigt and Maxwell models, and any other model based on linear springs and linear viscous dashpots, can be generalized into the form [24]

$$p_0\sigma + p_1\dot{\sigma} + p_2\ddot{\sigma} + \cdots = q_0\epsilon + q_1\dot{\epsilon} + q_2\ddot{\epsilon} + \cdots \ , \tag{52}$$

where p_i and q_i $(i = 0, 1, 2, \ldots)$ are the appropriate coefficients for the model being used.

All of these models can be generalized even further if we begin to use fractional derivatives. We will start by looking at the element

$$\sigma = p\frac{d^\alpha}{dt^\alpha}\epsilon, \tag{53}$$

where p is a proportionality factor and $0 \leq \alpha \leq 1$. When $\alpha = 0$, Equation (53) refers to a linear spring element, where p is the spring stiffness. When $\alpha = 1$, Equation (53) refers to a linear viscous dashpot, where p is the viscosity. When α is any value in between 0 and 1, we get a transition element that acts somewhere in between a linear spring and a linear viscous dashpot. Equation (53) was originally studied by Bagley and Torvik [6]. Koeller [50] later coined the term a spring-pot. The spring-pot leads to the general three element fractional derivative model, which is

$$p_0\sigma + p_1\frac{d^\alpha}{dt^\alpha}\sigma = q_0\epsilon + q_1\frac{d^\alpha}{dt^\alpha}\epsilon, \tag{54}$$

where $0 \leq \alpha \leq 1$.

Now that we have discussed the differing viscoelastic models, we will be better able to choose a model that best captures the material properties we seek to model. We can now focus on modeling the behavior of the material itself.

3.2 Material Behavior Model

Since the indentor of our surface is the AFM tip, which is a symmetric geometric shape, we will use cylindrical coordinates. The three-dimensional equations from the balance of linear momentum in a viscoelastic surface are [16]

$$\begin{aligned}\int_{-\infty}^{t} \left[\lambda(t-\tau) + 2\mu(t-\tau)\right] \frac{\partial}{\partial \tau} \left[\nabla \nabla \cdot \vec{u}\right] d\tau \\ - \int_{-\infty}^{t} \mu(t-\tau) \frac{\partial}{\partial \tau} \left[\nabla \times \nabla \times \vec{u}\right] d\tau = \bar{\rho} \frac{\partial^2 \vec{u}}{\partial t^2}, \quad (55)\end{aligned}$$

where $\bar{\rho}$ represents the density of the material. For a discussion on cylindrical coordinates, see Appendix A.

In addition to Equation (55), we need four boundary conditions for the material model. The first set of boundary conditions is at the surface $z = 0$, which is where the AFM interacts with the surface. At this surface, one of the boundary conditions is a mixed boundary condition. That is, it has a displacement representation from $0 < r < c_a(t)$, and a stress condition for $r > c_a(t)$. Here, $c_a(t)$ represents the contact area radius of the AFM with the surface. The boundary conditions at $z = 0$ are

$$u_z(r, \theta, 0, t) = y(t) - f(r), \qquad 0 < r < c_a(t), \qquad (56a)$$

$$\sigma_{zz}(r, \theta, 0, t) = 0, \qquad c_a(t) < r, \qquad (56b)$$

$$\sigma_{rz}(r, \theta, 0, t) = 0, \qquad \text{for all } r. \qquad (56c)$$

Here, $f(r)$ represents the geometry of the AFM tip. For the experiment we are modeling, the AFM tip geometry can be approximated by a paraboloid of radius R thus, $f(r) = \frac{r^2}{2R}$. Equation (56a) represents a coupling of the AFM to the surface, and assumes that the AFM remains in contact with the surface at all times. It also says that the AFM tip acts as a perfectly rigid indentor. Equation (56b) represents the fact that outside the contact area is a free boundary surface. If we were to set this equal to some exponentially decaying function, or the negative gradient of a potential function, it would represent the force of adhesion for forces acting over a short range, and the longer range forces (i.e., van der Waals forces, etc.) acting at a distance. Finally, Equation (56c) says that the tangential surface tractions vanish thus, $f(r)$ must be a smooth function.

The normal surface stress, $\sigma_{zz}(r, \theta, z, t)$, is defined in Equation (45), and the shear stress, $\sigma_{rz}(r, \theta, z, t)$, is defined as

$$\sigma_{rz}(r, \theta, z, t) = \int_{-\infty}^{t} \mu(t-\tau) \frac{\partial}{\partial \tau} \left[\frac{\partial u_r}{\partial z} + \frac{\partial u_z}{\partial r} \right] d\tau. \tag{57}$$

The second set of boundary conditions occur at the bottom of the polymer surface, where the polymer is attached to an ideally stiff substrate. The material thickness is represented by M_L. Since the polymer material is perfectly bonded to the substrate, and the substrate is perfectly rigid, there is no displacement in either the r or z-direction at M_L. This yields the boundary conditions at $z = M_L$ to be

$$u_r(r, \theta, M_L, t) = 0, \qquad \text{for all } r, \tag{58a}$$

$$u_z(r, \theta, M_L, t) = 0, \qquad \text{for all } r. \tag{58b}$$

Now that we have setup the general three-dimensional material model, we can focus on non-dimensionalizing both the material model and the AFM model.

3.3 Scaling the Models

Before we begin non-dimensionalizing the models, we must first identify some fundamental properties of both the AFM and the material. These properties can be seen in Table 1. The important AFM properties are the effective spring constant,

Table 1. Typical parameters for the experiment.

Parameter	Value
R	30 nm
k	0.06 N/m
ω_0	25 kHz
Q	~ 100
$\bar{\rho}$	1.05 g/cm^3
E_0	3 GPa
ν	$\frac{1}{3}$

$k = 0.06$ N/m; the resonant frequency, $\omega_0 = 25$ kHz; the quality factor, $Q \sim 100$; and the tip curvature radius, $R = 30$ nm. The substrate material is polystyrene, which has a density $\bar{\rho} = 1.05$ g/cm^3, an elastic modulus of $E_0 = 3$ GPa, and a Poisson's ratio of $\nu = \frac{1}{3}$. Now that some of the fundamental properties are known, we can begin to scale the models.

In order to scale the models, we must look at several natural length scales, and several natural frequencies, which correspond to time scales. There are three natural length scales that arise. They are the sample thickness, M_L; the initial contact area radius, c_a^0; and the change in contact area radius, $\bar{\delta}_a$, caused by the modulation. Here, we choose to write $c_a(t) = c_a^0 + \bar{\delta}_a \bar{c}_a^1(t)$, and note that since the preload is much greater than the dynamic loading, then $\bar{\delta}_a \ll c_a^0$. There are also three natural frequencies. The first is the undamped natural frequency of the AFM, ω_0. This leads to the time scale, $T_1 = \frac{1}{\omega_0} \equiv \sqrt{\frac{M}{k}}$. The second is the modulation frequency, ω_2. This produces the time scale, $T_2 = \frac{1}{\omega_2}$. Finally, the third time scale comes from the elastic wave propagation time through a distance ℓ for the elastic modulus of the surface, E_0. This leads to $T_3 = \ell\sqrt{\frac{\bar{\rho}}{E_0}}$, where ℓ will be determined from one of the length scales.

Now, let $t = t^* T$, $r = \ell\rho$, and $z = \ell\xi$, where T and ℓ are to be determined from one of the time and length scales, respectively. The time t^* is a dimensionless time, and ρ and ξ are dimensionless lengths. It is not necessary to scale θ since it is already dimensionless. However, we need to scale our model variables so they are dimensionless. To this end, let $y(t) = \ell(q_0 + q(t^*))$, $u_r(r,\theta,z,t) = \ell v_\rho(\rho,\theta,\xi,t^*)$, $u_\theta(r,\theta,z,t) = \ell v_\theta(\rho,\theta,\xi,t^*)$, and $u_z(r,\theta,z,t) = \ell v_\xi(\rho,\theta,\xi,t^*)$. The variables q_0 and $q(t^*)$ represent the dimensionless static displacement and the dimensionless dynamic displacement, respectively. In addition, we will scale out the elastic constant, E_0, from the Lamé constants. Thus, we let $\mu(t) = E_0\bar{\mu}(t^*)$ and $\lambda(t) = E_0\bar{\lambda}(t^*)$. Finally, let $c_a(t) = c_a^0(1 + \delta_a c_a^1(t^*))$, where $\delta_a = \frac{\bar{\delta}_a}{c_a^0} \ll 1$ is an unknown dimensionless parameter, and $\bar{c}_a^1(t) = \bar{c}_a^1(t^*T) = c_a^1(t^*)$.

Next, we will scale Equation (47). In addition to the above scalings, we will let $\beta_0 = \frac{\sqrt{kM}}{Q}$, and note that we can write $\frac{1}{M} = \frac{1}{kT_1^2}$. Also, we will divide through by $\frac{M\ell}{T^2}$, to yield

$$\ddot{q}(t^*) + \frac{1}{Q}\left(\frac{T}{T_1}\right)\dot{q}(t^*) + \left(\frac{T}{T_1}\right)^2[q(t^*) + q_0] = \frac{1}{k\ell}\left(\frac{T}{T_1}\right)^2 F_\sigma(t^*T) + \left(\frac{T}{T_1}\right)^2\left[\frac{\hat{B}_0}{\ell} + \frac{\hat{B}}{\ell}\sin(\omega_2 t^* T + \phi)\right]. \quad (59)$$

Now, applying these scalings to Equation (44) produces

$$F_\sigma(t^*T) = \ell^2 \int_0^{2\pi}\int_0^\infty \sigma_{\xi\xi}(\rho,\theta,\xi,t^*)\bigg|_{\xi=0} \rho d\rho d\theta, \quad (60)$$

where

$$\sigma_{\xi\xi}(\rho,\theta,\xi,t^*) = E_0\left[\int_{-\infty}^{t^*}\left[\bar{\lambda}(t^*-\tau^*) + 2\bar{\mu}(t^*-\tau^*)\right]\frac{\partial}{\partial\tau^*}\left[\frac{\partial v_\xi}{\partial\xi}\right]d\tau^* + \int_{-\infty}^{t^*}\bar{\lambda}(t^*-\tau^*)\frac{\partial}{\partial\tau^*}\left[\frac{\partial v_\rho}{\partial\rho} + \frac{v_\rho}{\rho} + \frac{1}{\rho}\frac{\partial v_\theta}{\partial\theta}\right]d\tau^*\right]. \quad (61)$$

Introducing these scalings into Equation (55) and dividing through by $\frac{E_0}{\ell}$ yields

$$\int_{-\infty}^{t^*} \left[\bar{\lambda}(t^* - \tau^*) + 2\bar{\mu}(t^* - \tau^*)\right] \frac{\partial}{\partial \tau^*} \left[\nabla\nabla \cdot \vec{v}\right] d\tau^* \\ - \int_{-\infty}^{t^*} \bar{\mu}(t^* - \tau^*) \frac{\partial}{\partial \tau^*} \left[\nabla \times \nabla \times \vec{v}\right] d\tau^* = \left(\frac{T_3}{T}\right)^2 \frac{\partial^2 \vec{v}}{\partial t^{*2}}, \quad (62)$$

where the cylindrical coordinate unit vectors are now $\hat{\rho}$, $\hat{\theta}$, and $\hat{\xi}$. The displacement vector is now written as

$$\vec{v}(\rho, \theta, \xi, t^*) = \begin{bmatrix} v_\rho(\rho, \theta, \xi, t^*) \\ v_\theta(\rho, \theta, \xi, t^*) \\ v_\xi(\rho, \theta, \xi, t^*) \end{bmatrix}. \quad (63)$$

Introducing the scalings into Equation (56), the boundary conditions at $\xi = 0$ become

$$v_\xi(\rho, \theta, 0, t^*) = q_0 + q(t^*) - \frac{f(\ell\rho)}{\ell}, \qquad 0 < \rho < \frac{c_a^0}{\ell}(1 + \delta_a c_a^1(t^*)), \quad (64a)$$

$$\sigma_{\xi\xi}(\rho, \theta, 0, t^*) = 0, \qquad \frac{c_a^0}{\ell}(1 + \delta_a c_a^1(t^*)) < \rho, \quad (64b)$$

$$\sigma_{\rho\xi}(\rho, \theta, 0, t^*) = 0, \qquad \text{for all } \rho, \quad (64c)$$

where

$$\sigma_{\rho\xi}(\rho, \theta, \xi, t^*) = E_0 \int_{-\infty}^{t^*} \bar{\mu}(t^* - \tau^*) \frac{\partial}{\partial \tau^*} \left[\frac{\partial v_\rho}{\partial \xi} + \frac{\partial v_\xi}{\partial \rho}\right] d\tau^*. \quad (65)$$

At the bottom boundary, $\xi = \frac{M_L}{\ell}$, Equation (58) becomes

$$v_\rho(\rho, \theta, \tfrac{M_L}{\ell}, t^*) = 0, \qquad \text{for all } \rho, \quad (66a)$$

$$v_\xi(\rho, \theta, \tfrac{M_L}{\ell}, t^*) = 0, \qquad \text{for all } \rho. \quad (66b)$$

Now, we will choose ℓ based on our length scales. Since, we are interested in what occurs under the tip of our AFM, we will choose $\ell = c_a^0$. Next, we choose T based on our time scales. Before we do so, we recall that the experimental modulation frequency, ω_2, occurs between 1 Hz and 1 kHz. Thus, $\omega_2 \ll \omega_0$, therefore, $T_1 \ll T_2$. This means that the AFM will behave quasi-statically. Also, the experiment is assumed to run at a fixed frequency for a sufficiently long enough time so that we are at equilibrium. So again, we see that the model will have a quasi-static solution. Looking at the time scales in more detail, $T_1 = \frac{1}{\omega_0} \approx 10^{-5}$s, $T_2 = \frac{1}{\omega_2}$ has a range from about 10^{-3}s to 1s, and $T_3 = c_a^0\sqrt{\frac{\bar{\rho}}{E_0}} \approx 10^{-12}$s. So, we'll choose $T = T_2$ in order to capture the large time scale, quasi-static behavior.

Define $\beta_1 = \frac{T_2}{T_1} = \frac{\omega_0}{\omega_2}$, which ranges from 25 to 25×10^3, and $\beta_2 = \frac{T_3}{T_2} = c_a^0\omega_2\sqrt{\frac{\bar{\rho}}{E_0}}$, which ranges from approximately 10^{-9} to 10^{-12}. Introducing all of the above into Equations (59)-(66) we get the dimensionless equations for the general, three-dimensional model of the experiment.

The dimensionless equation for the AFM model is

$$\ddot{q} + \frac{1}{Q}\beta_1\dot{q} + \beta_1^2\left[q + q_0\right] = \beta_1^2\left[B_0 + B\sin(t^* + \phi)\right] + \chi\beta_1^2\bar{F}_\sigma, \tag{67}$$

where $\bar{F}_\sigma(t^*) = \frac{F_\sigma(t^*/\omega_2)}{E_0{c_a^0}^2}$, $B_0 = \frac{\hat{B}_0}{c_a^0}$, and $B = \frac{\hat{B}}{c_a^0}$. The parameter $\chi = \frac{c_a^0 E_0}{k}$ is the ratio of two forces. To see this, we can write $\chi = \frac{{c_a^0}^2 E_0}{c_a^0 k}$. The force, ${c_a^0}^2E_0$, is proportional to the elastic force the polymer exerts on the tip of the AFM while the AFM is at its initial penetration depth. The force, c_a^0k, is the force that the AFM spring would exert when extended the length of c_a^0 into the polymer.

The dimensionless equations for the material behavior model are

$$\begin{aligned}\int_{-\infty}^{t^*}\left[\bar{\lambda}(t^* - \tau^*) + 2\bar{\mu}(t^* - \tau^*)\right]\frac{\partial}{\partial\tau^*}\left[\nabla\nabla\cdot\vec{v}\right]d\tau^* \\ - \int_{-\infty}^{t^*}\bar{\mu}(t^* - \tau^*)\frac{\partial}{\partial\tau^*}\left[\nabla\times\nabla\times\vec{v}\right]d\tau^* = \beta_2^2\frac{\partial^2\vec{v}}{\partial {t^*}^2},\end{aligned} \tag{68}$$

and the dimensionless boundary conditions are

$$v_\xi(\rho,\theta,0,t^*) = q_0 + q(t^*) - \bar{f}(\rho), \qquad 0 < \rho < 1 + \delta_a c_a^1(t^*), \tag{69a}$$

$$\sigma_{\xi\xi}(\rho,\theta,0,t^*) = 0, \qquad 1 + \delta_a c_a^1(t^*) < \rho, \tag{69b}$$

$$\sigma_{\rho\xi}(\rho,\theta,0,t^*) = 0, \qquad \text{for all } \rho, \tag{69c}$$

and

$$v_\rho(\rho,\theta,\bar{M}_L,t^*) = 0, \qquad \text{for all } \rho, \tag{70a}$$

$$v_\xi(\rho,\theta,\bar{M}_L,t^*) = 0, \qquad \text{for all } \rho, \tag{70b}$$

where $\bar{M}_L = \frac{M_L}{c_a^0}$, and $\bar{f}(\rho) = \frac{f(c_a^0\rho)}{c_a^0}$. For a parabolic tip shape, $\bar{f}(\rho) = \frac{c_a^0\rho^2}{2R}$.

In summary, this chapter discussed the different types of material behaviors, and the properties they exhibit. The main focus was on the linear viscoelastic behavior of materials, and how they can be modeled. We created a viscoelastic material model with boundary conditions that represent the experiment. The material model, boundary conditions, and the AFM model from the last chapter, were then scaled to capture the quasi-static nature of the experiment at the AFM tip.

IV. Reduced Three-Dimensional Model

Three-dimensional material models of physical systems are often complicated and need to be solved numerically. The goal of this chapter is to make appropriate assumptions so that our model still contains the pertinent physics but, has an analytical solution. The assumptions that we will make for our model are that we can approximate the material thickness by a semi-infinite half-space, and that we have axisymmetry. Before delving into the math and the reasons behind these assumptions, we will first present some important background information.

4.1 Infinite and Semi-Infinite Half-Space Models

Contact problems in the theory of elasticity generally assume that a rigid body acts on an elastic half-space. More recently, it has become increasingly important to study viscoelastic surfaces. In a book by Sneddon [83], static theories based on both elastic half-spaces and semi-infinite half-spaces are derived. N. N. Lebedev and Ia. S. Ufliand [51] developed solutions for an axisymmetric rigid body acting upon an elastic layer. They were able to express both the stresses and displacements in terms of a single function which, is the solution of a Fredholm integral equation. R. Y. S. Pak [69] presented a method based on potentials for the dynamic response of an elastic half-space to an arbitrary, time-harmonic, finite, buried source. An arbitrary set of transformed stress-potential and displacement-potential relations were developed and can be used in a multitude of wave propagation problems. He specifically looked at an embedded source of uniform distributions. Later, Pak and Guzina[70] derived fundamental Green's functions for the elastodynamic half-space problem involving mixed boundary conditions and multilayered media. They solved three-dimensional problems using a method of displacement potentials with a set of generalized transmission-reflection matrices and internal source fields. Their solutions encompassed both elastic and viscoelastic cases.

In the theory of viscoelasticity, the contact problem is defined by mixed boundary conditions which vary for the region of contact and the region of no contact. In general, the contact region varies with time. Lee and Radok [52] showed the solution of the viscoelastic counterpart of the Hertz problem in elasticity can be deduced from the elastic solution. The solution is obtained for general linear viscoelastic operators on a half-space. T. C. T. Ting [93] derived an explicit solution of an integral equation which arises in multiple contact problems for linear viscoelastic half-spaces. His solution is valid for a contact area which is a multiply-connected region or regions. Additionally, the time-dependent contact area can be any arbitrary function of time.

4.2 Dual Integral Equations

Dual integral equations often arise when dealing with mixed boundary value problems. The general form of dual integral equations is

$$\begin{aligned} \int_0^\infty K_1(xt)\left[1+w(t)\right]\Phi(t)dt &= f(x), && 0<x<1, \\ \int_0^\infty K_2(xt)\Phi(t)dt &= g(x), && x>1, \end{aligned} \tag{71}$$

where $K_1(xt)$ and $K_2(xt)$ are the kernel functions. These kernels can be trigonometric functions, Bessel functions of the first or second kind, or modified Bessel functions of the first or second kind. $\Phi(t)$ is the unknown function, and $w(t)$ is an arbitrary weight function. Finally, $f(x)$ and $g(x)$ are known functions that arise from the boundary conditions of the problem being solved.

When the problem being modeled has axisymmetric, mixed boundary conditions, such as the experiment we are modeling, the dual integral equations that arise often have Bessel functions as their kernels. For this reason, we will focus on dual integral equations that have Bessel functions of the first kind as their kernel. The general form of dual integral equations involving Bessel functions of the first kind is

$$\begin{aligned} \int_0^\infty t^{-2\alpha} J_\nu(xt) \left[1 + w(t)\right] \Phi(t) dt &= f(x), && 0 < x < 1, \\ \int_0^\infty t^{-2\beta} J_\mu(xt) \Phi(t) dt &= g(x), && x > 1, \end{aligned} \tag{72}$$

where α and β are known constants, ν and μ are the known orders of the Bessel functions, $w(t)$ is an arbitrary known weight function, $f(x)$ and $g(x)$ are known functions valid over their particular region, and $\Phi(t)$ is the unknown function to be determined.

There have been many methods used to study dual integral equations of this class. Some methods are based on particular solutions such as Titchmarsh [94], where in Equation (72), $w(t) = 0$. Noble [65] used a multiplying factor method on a class of dual integral equations, where the Bessel functions are of the same order ($\nu = \mu$). Nasim [64] used the properties of Mellin transforms to reduce the dual integral equations to a single integral equation which can be solved using Hankel transforms. Most methods use some form of the integral operator to reduce the dual integral equation to a single integral equation, which can be solved using a different method [61]. Mandal [60] used Sonine's integrals to reduce Equation (72) to a Fredholm integral equation of the second kind. Mandal's method is the most general and applies to all the possibilities of Equation (72). Since we will use the results from Mandal [60], a brief summary of that paper is given in Appendix B.

4.3 Axisymmetry

We will now make assumptions based on the physics of the experiment so that we may simplify the model for the experimental system. Recall the scaled, three-dimensional model of the experimental system that we created last chapter. The first assumption we will make is that the AFM tip forces produce axisymmetric loading. This is a valid assumption since we only have AFM tip movement in the z-direction, and the AFM tip is modeled as a paraboloid of revolution. As a result, there is no θ dependence for any parameter, u_θ is identically zero, and all derivatives with respect to θ vanish. Equation (67) remains as

$$\ddot{q} + \frac{1}{Q}\beta_1\dot{q} + \beta_1^2\left[q + q_0\right] = \beta_1^2\left[B_0 + B\sin(t^* + \phi)\right] + \chi\beta_1^2\bar{F}_\sigma, \tag{73}$$

however, $\bar{F}_\sigma$ is now written as

$$\bar{F}_\sigma(t^*) = \frac{2\pi}{E_0}\int_0^\infty \sigma_{\xi\xi}(\rho,\xi,t^*)\bigg|_{\xi=0}\rho d\rho. \tag{74}$$

If we define the linear operator $L_\rho g = \frac{\partial g}{\partial \rho} + \frac{g}{\rho} = \frac{1}{\rho}\frac{\partial}{\partial \rho}(\rho g)$, then Equation (61) becomes

$$\begin{aligned}\sigma_{\xi\xi}(\rho,\xi,t^*) = E_0\Bigg[\int_{-\infty}^{t^*}\left[\bar{\lambda}(t^*-\tau^*) + 2\bar{\mu}(t^*-\tau^*)\right]\frac{\partial}{\partial\tau^*}\left[\frac{\partial v_\xi}{\partial \xi}\right]d\tau^* \\ + \int_{-\infty}^{t^*}\bar{\lambda}(t^*-\tau^*)\frac{\partial}{\partial\tau^*}\left[L_\rho v_\rho\right]d\tau^*\Bigg].\end{aligned} \tag{75}$$

Equation (68) remains as

$$\begin{aligned}\int_{-\infty}^{t^*}\left[\bar{\lambda}(t^*-\tau^*) + 2\bar{\mu}(t^*-\tau^*)\right]\frac{\partial}{\partial\tau^*}\left[\nabla\nabla\cdot\vec{v}\right]d\tau^* \\ - \int_{-\infty}^{t^*}\bar{\mu}(t^*-\tau^*)\frac{\partial}{\partial\tau^*}\left[\nabla\times\nabla\times\vec{v}\right]d\tau^* = \beta_2^2\frac{\partial^2\vec{v}}{\partial {t^*}^2},\end{aligned} \tag{76}$$

where we keep in mind that all derivatives with respect to θ vanish, and the displacement vector is now written as

$$\vec{v}(\rho, \xi, t^*) = \begin{bmatrix} v_\rho(\rho, \xi, t^*) \\ 0 \\ v_\xi(\rho, \xi, t^*) \end{bmatrix}. \tag{77}$$

The boundary conditions, Equations (69) and (70), become

$$v_\xi(\rho, 0, t^*) = q_0 + q(t^*) - \bar{f}(\rho), \qquad 0 < \rho < 1 + \delta_a c_a^1(t^*), \tag{78a}$$

$$\sigma_{\xi\xi}(\rho, 0, t^*) = 0, \qquad 1 + \delta_a c_a^1(t^*) < \rho, \tag{78b}$$

$$\sigma_{\rho\xi}(\rho, 0, t^*) = 0, \qquad \text{for all } \rho, \tag{78c}$$

and

$$v_\rho(\rho, \bar{M}_L, t^*) = 0, \qquad \text{for all } \rho, \tag{79a}$$

$$v_\xi(\rho, \bar{M}_L, t^*) = 0, \qquad \text{for all } \rho, \tag{79b}$$

respectively. The shear stress is now given by

$$\sigma_{\rho\xi}(\rho, \xi, t^*) = E_0 \int_{-\infty}^{t^*} \bar{\mu}(t^* - \tau^*) \frac{\partial}{\partial \tau^*} \left[\frac{\partial v_\rho}{\partial \xi} + \frac{\partial v_\xi}{\partial \rho} \right] d\tau^*. \tag{80}$$

Equations (73)-(80) represent the reduced axisymmetric model of the system.

4.4 The Hankel Transform

We will now make use of the Hankel transform by defining

$$v_\rho(\rho, \xi, t^*) = \int_0^\infty \beta J_1(\beta\rho) g_\rho(\xi, \beta, t^*) d\beta \tag{81}$$

and

$$v_\xi(\rho, \xi, t^*) = \int_0^\infty \beta J_0(\beta\rho) g_\xi(\xi, \beta, t^*) d\beta. \tag{82}$$

The associated inverse Hankel transforms of Equations (81) and (82) are defined to be

$$g_\rho(\xi, \beta, t^*) = \int_0^\infty \rho J_1(\beta\rho) v_\rho(\rho, \xi, t^*) d\rho \tag{83}$$

and

$$g_\xi(\xi, \beta, t^*) = \int_0^\infty \rho J_0(\beta\rho) v_\xi(\rho, \xi, t^*) d\rho. \tag{84}$$

The requirement for the existence of Equations (81) and (82) are that the functions $\sqrt{\beta} g_\rho(\xi, \beta, t^*)$ and $\sqrt{\beta} g_\xi(\xi, \beta, t^*)$ be piecewise continuous and absolutely integrable for $\beta \in (0, \infty)$ [2].

Applying Equations (81) and (82), we see that, Equations (73) and (74) remain unchanged while, Equation (75) is transformed to

$$\begin{aligned} \sigma_{\xi\xi}(\rho, \xi, t^*) = \\ E_0 \Bigg[\int_{-\infty}^{t^*} \int_0^\infty \beta J_0(\beta\rho) \left[\bar{\lambda}(t^* - \tau^*) + 2\bar{\mu}(t^* - \tau^*) \right] \frac{\partial}{\partial \tau^*} g'_\xi(\xi, \beta, \tau^*) d\beta d\tau^* \\ + \int_{-\infty}^{t^*} \int_0^\infty \beta^2 J_0(\beta\rho) \bar{\lambda}(t^* - \tau^*) \frac{\partial}{\partial \tau^*} g_\rho(\xi, \beta, \tau^*) d\beta d\tau^* \Bigg], \end{aligned} \tag{85}$$

where $'$ denotes $\frac{\partial}{\partial \xi}$, and we have used the property $L_\rho J_1(\beta\rho) = \frac{1}{\rho} \frac{\partial}{\partial \rho} \left[\rho J_1(\beta\rho) \right] = \beta J_0(\beta\rho)$ [12].

Substituting Equation (85) into Equation (74), interchanging the order of integration, and evaluating the ρ integral yields

$$\begin{aligned}\bar{F}_\sigma(t^*) &= 2\pi(1+\delta_a c_a^1(t^*)) \\ &\times \left[\int_{-\infty}^{t^*}\int_0^\infty J_1(\beta(1+\delta_a c_a^1(t^*)))\left[\bar{\lambda}(t^*-\tau^*)+2\bar{\mu}(t^*-\tau^*)\right]\frac{\partial}{\partial\tau^*}g_\xi'(0,\beta,\tau^*)d\beta d\tau^*\right. \\ &\qquad \left. + \int_{-\infty}^{t^*}\int_0^\infty \beta J_1(\beta(1+\delta_a c_a^1(t^*)))\bar{\lambda}(t^*-\tau^*)\frac{\partial}{\partial\tau^*}g_\rho(0,\beta,\tau^*)d\beta d\tau^*\right]. \quad (86)\end{aligned}$$

Here, we have taken advantage of the fact that $\sigma_{\xi\xi}=0$ for $\rho > 1+\delta_a c_a^1(t^*)$. We have also used the relationship $\rho J_0(\beta\rho) = \frac{1}{\beta}\frac{\partial}{\partial\rho}\left[\rho J_1(\beta\rho)\right]$ [12].

Applying our Hankel transforms to Equation (76), separating into two non-zero components, and using the properties $L_\rho J_1(\beta\rho) = \beta J_0(\beta\rho)$ and $\frac{\partial}{\partial\rho}J_0(\beta\rho) = -\beta J_1(\beta\rho)$ [12], produces

$$\begin{aligned}&-\int_{-\infty}^{t^*}\int_0^\infty \beta J_1(\beta\rho)\left[\bar{\lambda}(t^*-\tau^*)+2\bar{\mu}(t^*-\tau^*)\right]\frac{\partial}{\partial\tau^*}\left[\beta^2 g_\rho(\xi,\beta,\tau^*)+\beta g_\xi'(\xi,\beta,\tau^*)\right]d\beta d\tau^* \\ &\qquad + \int_{-\infty}^{t^*}\int_0^\infty \beta J_1(\beta\rho)\bar{\mu}(t^*-\tau^*)\frac{\partial}{\partial\tau^*}\left[\beta g_\xi'(\xi,\beta,\tau^*)+g_\rho''(\xi,\beta,\tau^*)\right]d\beta d\tau^* \\ &\qquad\qquad = \beta_2^2\int_0^\infty \beta J_1(\beta\rho)\frac{\partial^2 g_\rho}{\partial {t^*}^2}(\xi,\beta,\tau^*)d\beta, \quad (87)\end{aligned}$$

and

$$\begin{aligned}&\int_{-\infty}^{t^*}\int_0^\infty \beta J_0(\beta\rho)\left[\bar{\lambda}(t^*-\tau^*)+2\bar{\mu}(t^*-\tau^*)\right]\frac{\partial}{\partial\tau^*}\left[\beta g_\rho'(\xi,\beta,\tau^*)+g_\xi''(\xi,\beta,\tau^*)\right]d\beta d\tau^* \\ &\qquad - \int_{-\infty}^{t^*}\int_0^\infty \beta J_0(\beta\rho)\bar{\mu}(t^*-\tau^*)\frac{\partial}{\partial\tau^*}\left[\beta^2 g_\xi(\xi,\beta,\tau^*)+\beta g_\rho'(\xi,\beta,\tau^*)\right]d\beta d\tau^* \\ &\qquad\qquad = \beta_2^2\int_0^\infty \beta J_0(\beta\rho)\frac{\partial^2 g_\xi}{\partial {t^*}^2}(\xi,\beta,\tau^*)d\beta. \quad (88)\end{aligned}$$

Now, we can take the appropriate inverse Hankel transforms of Equations (87) and

(88) to obtain

$$
\begin{aligned}
-\int_{-\infty}^{t^*} \left[\bar{\lambda}(t^*-\tau^*)+2\bar{\mu}(t^*-\tau^*)\right] \frac{\partial}{\partial\tau^*}\left[\beta^2 g_\rho(\xi,\beta,\tau^*)+\beta g'_\xi(\xi,\beta,\tau^*)\right] d\tau^* \\
+\int_{-\infty}^{t^*} \bar{\mu}(t^*-\tau^*)\frac{\partial}{\partial\tau^*}\left[\beta g'_\xi(\xi,\beta,\tau^*)+g''_\rho(\xi,\beta,\tau^*)\right] d\tau^* = \beta_2^2\frac{\partial^2 g_\rho}{\partial {t^*}^2}(\xi,\beta,\tau^*), \quad (89)
\end{aligned}
$$

and

$$
\begin{aligned}
\int_{-\infty}^{t^*} \left[\bar{\lambda}(t^*-\tau^*)+2\bar{\mu}(t^*-\tau^*)\right] \frac{\partial}{\partial\tau^*}\left[\beta g'_\rho(\xi,\beta,\tau^*)+g''_\xi(\xi,\beta,\tau^*)\right] d\tau^* \\
-\int_{-\infty}^{t^*} \bar{\mu}(t^*-\tau^*)\frac{\partial}{\partial\tau^*}\left[\beta^2 g_\xi(\xi,\beta,\tau^*)+\beta g'_\rho(\xi,\beta,\tau^*)\right] d\tau^* = \beta_2^2\frac{\partial^2 g_\xi}{\partial {t^*}^2}(\xi,\beta,\tau^*). \quad (90)
\end{aligned}
$$

Substituting Equation (82) into Equation (78a) yields

$$
\int_0^\infty \beta J_0(\beta\rho) g_\xi(0,\beta,\tau^*)d\beta = q_0 + q(t^*) - \bar{f}(\rho), \qquad 0<\rho<1+\delta_a c_a^1(t^*), \qquad (91)
$$

and substituting Equation (85) into Equation (78b), and dividing both sides by E_0, yields

$$
\begin{aligned}
\int_{-\infty}^{t^*}\int_0^\infty \beta J_0(\beta\rho)\left[\bar{\lambda}(t^*-\tau^*)+2\bar{\mu}(t^*-\tau^*)\right]\frac{\partial}{\partial\tau^*} g'_\xi(0,\beta,\tau^*)d\beta d\tau^* \\
+\int_{-\infty}^{t^*}\int_0^\infty \beta^2 J_0(\beta\rho)\bar{\lambda}(t^*-\tau^*)\frac{\partial}{\partial\tau^*} g_\rho(0,\beta,\tau^*)d\beta d\tau^* = 0, \qquad 1+\delta_a c_a^1(t^*)<\rho. \quad (92)
\end{aligned}
$$

Applying the Hankel transforms, Equations (81) and (82), to Equation (80), and using the property $\frac{\partial}{\partial\rho}J_0(\beta\rho) = -\beta J_1(\beta\rho)$ [12], admits the equation

$$
\sigma_{\rho\xi}(\rho,\xi,t^*) = E_0\int_{-\infty}^{t^*}\int_0^\infty \beta J_1(\beta\rho)\bar{\mu}(t^*-\tau^*)\frac{\partial}{\partial\tau^*}\left[g'_\rho(\xi,\beta,\tau^*)-\beta g_\xi(\xi,\beta,\tau^*)\right] d\beta d\tau^*. \qquad (93)
$$

Substituting Equation (93) into Equation (78c), dividing both sides by E_0, and taking the appropriate inverse Hankel transform yields

$$\int_{-\infty}^{t^*} \bar{\mu}(t^* - \tau^*) \frac{\partial}{\partial \tau^*} \left[g_\rho'(0, \beta, \tau^*) - \beta g_\xi(0, \beta, \tau^*) \right] d\tau^* = 0. \tag{94}$$

Since $\bar{\mu}$ is a Lamé parameter, and is a function of the material properties, then it must not be zero everywhere. Thus, Equation (94) yields

$$g_\rho'(0, \beta, \tau^*) - \beta g_\xi(0, \beta, \tau^*) = 0. \tag{95}$$

Finally, applying our Hankel transforms to Equation (79) we see that it is necessary for

$$g_\rho(\bar{M}_L, \beta, \tau^*) = 0, \tag{96a}$$

$$g_\xi(\bar{M}_L, \beta, \tau^*) = 0. \tag{96b}$$

4.5 The Fourier Transform

In order to solve Equations (73) and (86)-(96), we will need to take their Fourier transforms. We define the Fourier transformation of a function, $f(t^*)$, as

$$\hat{f}(\omega) = \int_{-\infty}^{\infty} f(t^*) e^{-i\omega t^*} dt^*, \tag{97}$$

and we define the inverse Fourier transform as

$$f(t^*) = \frac{1}{2\pi} \int_{-\infty}^{\infty} \hat{f}(\omega) e^{i\omega t^*} d\omega. \tag{98}$$

It is required that $f(t^*)$ be piecewise smooth and absolutely integrable on $(-\infty, \infty)$ [2].

Taking the Fourier transform of Equation (73), dividing through by β_1^2, and rearranging, yields

$$L_0(\omega;\beta_1,Q)\hat{q}(\omega) = 2\pi\delta(\omega)\left[B_0 - q_0\right] + BS(\omega,\phi) + \chi\hat{F}_\sigma(\omega), \tag{99}$$

where $\delta(\omega)$ is the Dirac delta function,

$$S(\omega,\phi) = -i\pi\left[e^{i\phi}\delta(\omega-1) - e^{-i\phi}\delta(\omega+1)\right], \tag{100}$$

which is the Fourier transform of the shifted sine function, and

$$L_0(\omega;\beta_1,Q) = -\left(\frac{\omega}{\beta_1}\right)^2 + i\frac{1}{Q}\left(\frac{\omega}{\beta_1}\right) + 1. \tag{101}$$

Now, before we take the Fourier transform of Equation (86), we will recall from Section 3.3 that $\delta_a \ll 1$. So, $1+\delta_a c_a^1(t^*) \approx 1$, and by a Taylor series expansion around β, $J_1(\beta(1+\delta_a c_a^1(t^*))) \approx J_1(\beta) + \frac{\beta\delta_a}{2}c_a^1(t^*)\left[J_0(\beta) - J_2(\beta)\right] + \mathcal{O}(\beta\delta_a)^2$. Thus, to leading order, the Fourier transform of Equation (86) is

$$\hat{F}_\sigma(\omega) = 2\pi\left[\hat{\lambda}(\omega) + 2\hat{\mu}(\omega)\right]\int_0^\infty J_1(\beta)\left[\hat{g}'_\xi(0,\beta,\omega) + \bar{\alpha}(\omega)\beta\hat{g}_\rho(0,\beta,\omega)\right]d\beta + \mathcal{O}(\delta_a), \tag{102}$$

where $\hat{g}_\rho(\xi,\beta,\omega)$ and $\hat{g}_\xi(\xi,\beta,\omega)$ are the Fourier transformations of $g_\rho(\xi,\beta,t^*)$ and $g_\xi(\xi,\beta,t^*)$, respectively, and $\bar{\alpha}(\omega) = \frac{\hat{\lambda}(\omega)}{\hat{\lambda}(\omega)+2\hat{\mu}(\omega)}$. In addition,

$$\hat{\lambda}(\omega) = i\omega\int_0^\infty e^{-i\omega t^*}\bar{\lambda}(t^*)dt^*, \tag{103}$$

and

$$\hat{\mu}(\omega) = i\omega\int_0^\infty e^{-i\omega t^*}\bar{\mu}(t^*)dt^*. \tag{104}$$

We define the Fourier transformed viscoelastic Lamé parameters, Equations (103) and (104), in this way so that we have the possibility of using the elastic-viscoelastic correspondence principle. As you will see later, we will not use the correspondence principle, and in doing so, we can attain an analytic solution to the linear approximation of our problem.

Taking the Fourier transforms of Equations (89) and (90), and collecting like terms yields

$$\hat{g}_\rho''(\xi,\beta,\omega)+\left[k_s^2-\frac{\beta^2}{\alpha(\omega)}\right]\hat{g}_\rho(\xi,\beta,\omega)+\frac{\beta(\alpha(\omega)-1)}{\alpha(\omega)}\hat{g}_\xi'(\xi,\beta,\omega)=0, \tag{105}$$

and

$$\hat{g}_\xi''(\xi,\beta,\omega)+\left[k_p^2-\alpha(\omega)\beta^2\right]\hat{g}_\xi(\xi,\beta,\omega)+\beta(1-\alpha(\omega))\hat{g}_\rho'(\xi,\beta,\omega)=0, \tag{106}$$

where $\alpha(\omega)=\frac{\hat{\mu}(\omega)}{\hat{\lambda}(\omega)+2\hat{\mu}(\omega)}$. Observe that $\bar{\alpha}(\omega)=1-2\alpha(\omega)$. The dimensionless shear wave number is represented by $k_s^2=\frac{\beta_2^2\omega^2}{\hat{\mu}(\omega)}$, and the dimensionless compressive wave number is $k_p^2=\frac{\beta_2^2\omega^2}{\hat{\lambda}(\omega)+2\hat{\mu}(\omega)}$. Note that $k_p^2=\alpha(\omega)k_s^2$.

Next, the Fourier transform of Equations (95) and (96), yield

$$\hat{g}_\rho'(0,\beta,\omega)=\beta\hat{g}_\xi(0,\beta,\omega), \tag{107}$$

and

$$\hat{g}_\rho(\bar{M}_L,\beta,\omega)=0, \tag{108a}$$

$$\hat{g}_\xi(\bar{M}_L,\beta,\omega)=0, \tag{108b}$$

respectively. Again, taking advantage of the fact that $\delta_a \ll 1$ so, $1+\delta_a c_a^1(t^*)\approx 1$, and Fourier transforming the linear approximation of the last two boundary conditions, Equations (91) and (92), produces the dual integral equations

$$\int_0^\infty \beta J_0(\beta\rho)\hat{g}_\xi(0,\beta,\omega)d\beta = 2\pi\delta(\omega)\left[q_0 - \bar{f}(\rho)\right] + \hat{q}(\omega), \qquad 0 < \rho < 1, \tag{109}$$

and

$$\int_0^\infty \beta J_0(\beta\rho)\left[\hat{g}'_\xi(0,\beta,\omega) + \bar{\alpha}(\omega)\beta\hat{g}_\rho(0,\beta,\omega)\right]d\beta = 0, \qquad 1 < \rho, \tag{110}$$

where we have divided through by $\hat{\lambda}(\omega) + 2\hat{\mu}(\omega)$ in the latter equation.

Equations (99)-(110) represent the linear approximation to the fully transformed, scaled, and reduced model of our experimental system. The equations show a reduced three-dimensional model of the material behavior coupled through the boundary conditions to a one-dimensional model of the AFM system. We can now move on to solving this system of equations.

4.6 Reducing the Experimental Model to a Dual Integral Equation

In this section, the coupled system of second order differential equations for $\hat{g}_\xi(\xi,\beta,\omega)$ and $\hat{g}_\rho(\xi,\beta,\omega)$ is reduced to a system of first order equations. The standard eigenvalue and eigenvector representation of the solution is exhibited with expansion coefficients determined through the boundary conditions. This will lead to the dual integral equation problem which is evaluated in the next section.

First, Equations (105) and (106) can be transformed to the system

$$\vec{G}' = \begin{bmatrix} \hat{g}'_\xi \\ \hat{g}'_\rho \\ \hat{g}''_\xi \\ \hat{g}''_\rho \end{bmatrix} = D\vec{G} = \begin{bmatrix} 0 & 0 & 1 & 0 \\ 0 & 0 & 0 & 1 \\ \alpha\beta^2 - k_p^2 & 0 & 0 & \beta(\alpha-1) \\ 0 & (\frac{\beta^2}{\alpha} - k_s^2) & \frac{\beta(1-\alpha)}{\alpha} & 0 \end{bmatrix} \begin{bmatrix} \hat{g}_\xi \\ \hat{g}_\rho \\ \hat{g}'_\xi \\ \hat{g}'_\rho \end{bmatrix}. \tag{111}$$

The solution to this system is of the form

$$\vec{G} = \sum_{i=1}^{4} A_i(\beta, \omega)\vec{v}_i e^{\lambda_i \xi}, \tag{112}$$

where the A_i's are the coefficients determined from the boundary conditions, and λ_i and $\vec{v}_i$ are the eigenvalues and the associated eigenvectors for the matrix D.

For this system, define

$$\begin{aligned} \lambda_p &= (\beta^2 - k_p^2)^{1/2}, \\ \lambda_s &= (\beta^2 - k_s^2)^{1/2}, \end{aligned} \tag{113}$$

which represent the complex wave speeds associated with the mode shape given by $J_0(\beta\rho)$. Further, the positive branch of the square root is chosen. Thus, the eigenvalues are

$$\begin{aligned} \lambda_1 &= -\lambda_p, \\ \lambda_2 &= \lambda_s, \\ \lambda_3 &= -\lambda_s, \\ \lambda_4 &= \lambda_p, \end{aligned} \tag{114}$$

with associated eigenvectors

$$\begin{aligned} \vec{v}_1 &= \left[\frac{-1}{\beta}, \frac{-1}{\lambda_p}, \frac{\lambda_p}{\beta}, 1\right]^T, \\ \vec{v}_2 &= \left[\frac{-\beta}{\lambda_s^2}, \frac{1}{\lambda_s}, \frac{-\beta}{\lambda_s}, 1\right]^T, \\ \vec{v}_3 &= \left[\frac{-\beta}{\lambda_s^2}, \frac{-1}{\lambda_s}, \frac{\beta}{\lambda_s}, 1\right]^T, \\ \vec{v}_4 &= \left[\frac{-1}{\beta}, \frac{1}{\lambda_p}, \frac{-\lambda_p}{\beta}, 1\right]^T. \end{aligned} \tag{115}$$

Inserting these values, Equations (114) and (115), into Equation (112), $\hat{g}_\xi$ and $\hat{g}_\rho$ become

$$\begin{aligned}\hat{g}_\xi &= -\frac{1}{\beta}\left[A_1 e^{-\lambda_p \xi} + A_4 e^{\lambda_p \xi}\right] - \frac{\beta}{\lambda_s^2}\left[A_2 e^{\lambda_s \xi} + A_3 e^{-\lambda_s \xi}\right],\\ \hat{g}_\rho &= -\frac{1}{\lambda_p}\left[A_1 e^{-\lambda_p \xi} - A_4 e^{\lambda_p \xi}\right] + \frac{1}{\lambda_s}\left[A_2 e^{\lambda_s \xi} - A_3 e^{-\lambda_s \xi}\right].\end{aligned} \tag{116}$$

To determine the A_i's, Equations (107)-(110) are required. First, we examine the boundary conditions at $\bar{M}_L = \frac{M_L}{c_a^0}$, which are Equations (108). Since M_L for the experiment is 30 nm, 70 nm, or 220 nm, and $c_a^0 \approx 2$ nm then, typical values of $\bar{M}_L$ are in the 10 - 100 range. Also note that the contact area radius is much smaller than the thickness of the sample thus, $M_L \gg c_a^0$. Further, because the positive branch of the square root function is used, $\Re(\lambda_p), \Re(\lambda_s) \geq 0$, for all β. This means $e^{\lambda_p \xi}$ and $e^{\lambda_s \xi}$ will see exponential growth as ξ becomes large while, $e^{-\lambda_p \xi}$ and $e^{-\lambda_s \xi}$ will see exponential decay. Therefore, to satisfy Equations (108), both A_2 and A_4 must be exponentially small. We choose to set $A_2 = A_4 = 0$ which, is equivalent to letting $\bar{M}_L \to \infty$. This is valid as long as $M_L \gg c_a^0$. Now, Equations (116) are reduced to

$$\begin{aligned}\hat{g}_\xi &= -\frac{1}{\beta} A_1 e^{-\lambda_p \xi} - \frac{\beta}{\lambda_s^2} A_3 e^{-\lambda_s \xi},\\ \hat{g}_\rho &= -\frac{1}{\lambda_p} A_1 e^{-\lambda_p \xi} - \frac{1}{\lambda_s} A_3 e^{-\lambda_s \xi}.\end{aligned} \tag{117}$$

Using Equations (117) along with Equations (113) in Equation (107) produces the relation

$$A_1(\beta,\omega) = -\frac{1}{2\lambda_s^2}\left(2\beta^2 - k_s^2\right) A_3(\beta,\omega). \tag{118}$$

The final coefficient, A_3, is found using Equations (109) and (110). To this end, define

$A(\beta,\omega)$ by

$$-\alpha A(\beta,\omega) = \hat{g}'_\xi(0,\beta,\omega) + \bar{\alpha}\beta\hat{g}_\rho(0,\beta,\omega) = -\alpha A_3\left[\frac{(2\beta^2 - k_s^2)^2}{2\beta\lambda_s^2\lambda_p} - \frac{2\beta}{\lambda_s}\right], \qquad (119)$$

and $w(\beta)$ by

$$\left[1 + w(\beta)\right] A(\beta,\omega) = \beta\hat{g}_\xi(0,\beta,\omega) = -\frac{k_s^2}{2\lambda_s^2}A_3. \qquad (120)$$

In the above definitions we have made use of the facts that $\bar{\alpha} = 1 - 2\alpha$ and $k_p^2 = \alpha k_s^2$. Combining Equations (119) and (120) yields

$$1 + w(\beta) = \frac{\beta k_s^2\lambda_p}{4\beta^2\lambda_s\lambda_p - (2\beta^2 - k_s^2)^2}. \qquad (121)$$

Now, the boundary conditions given in Equations (109) and (110) are reduced to solving the dual integral equations

$$\int_0^\infty \beta A(\beta,\omega)J_0(\beta\rho)d\beta = 0, \qquad 1 < \rho, \qquad (122)$$

and

$$\int_0^\infty A(\beta,\omega)J_0(\beta\rho)\left[1 + w(\beta)\right]d\beta$$
$$= 2\pi\delta(\omega)\left[q_0 - \bar{f}(\rho)\right] + \hat{q}(\omega), \qquad 0 < \rho < 1, \qquad (123)$$

for the unknown function $A(\beta,\omega)$. Having determined $A(\beta,\omega)$, Equations (118) and (120) are used to produce

$$A_1(\beta,\omega) = \frac{2\beta^2 - k_s^2}{k_s^2}\left[1 + w(\beta)\right]A(\beta,\omega), \qquad (124)$$

and

$$A_3(\beta,\omega) = -\frac{2\lambda_s^2}{k_s^2}\left[1 + w(\beta)\right] A(\beta,\omega). \qquad (125)$$

This completes the solution to the transformed system, Equation (111), with $\hat{g}_\xi(\xi,\beta,\omega)$ and $\hat{g}_\rho(\xi,\beta,\omega)$ given by Equation (117) along with Equations (124) and (125). All that remains is the determination of $A(\beta,\omega)$ from Equations (122) and (123).

4.7 Reduction of the Dual Integral Equation

In this section, the dual integral equations, Equations (122) and (123), will be transformed to a Fredholm integral equation of the second kind following a method presented by Mandal [60] and reviewed in Appendix B.

Comparing Equations (122) and (123) to Equation (236), we see that $A(\beta,\omega)$ represents the unknown function $\Phi(\beta)$. Also, $f(\rho) = f_1(\rho,\omega) = 2\pi\delta(\omega)\left[q_0 - \bar{f}(\rho)\right] + \hat{q}(\omega)$ and $g(\rho) = 0$. Additionally, $\alpha^* = 0$, $\beta^* = -\frac{1}{2}$, and $\mu = \nu = 0$. Thus, from Equations (238), $\lambda = \gamma = -\frac{1}{2}$. We choose $s = 0$, since that would yield $\lambda + s = -\frac{1}{2} > -1$. So, from Equations (239) with $s = 0$, $F_1(r) = F(r)$ and $G_1(r) = G(r)$.

Now, from Equations (241), $\xi = \ell - \frac{3}{2}$ and $\eta = m - \frac{1}{2}$. Therefore, we choose $\ell = 1$ and $m = 0$ so that $\xi = \eta = -\frac{1}{2} > -1$. From Equations (240), $G(r) = 0$ and

$$F(r;\omega) = \sqrt{\frac{2}{\pi r}}\frac{\partial}{\partial r}\int_0^r \rho(r^2 - \rho^2)^{-\frac{1}{2}} f_1(\rho,\omega)d\rho. \qquad (126)$$

Recall that for a parabolic tip shape, $\bar{f}(\rho) = \frac{c_a^0\rho^2}{2R}$. Using this along with $f_1(\rho,\omega)$, Equation (126) becomes

$$\begin{aligned} F(r;\omega) &= \sqrt{\frac{2}{\pi r}}\frac{\partial}{\partial r}\left[(2\pi\delta(\omega)q_0 + \hat{q}(\omega))\int_0^r \rho(r^2-\rho^2)^{-\frac{1}{2}}d\rho \right. \\ &\qquad \left. - \left(2\pi\delta(\omega)\frac{c_a^0}{2R}\right)\int_0^r \rho^3(r^2-\rho^2)^{-\frac{1}{2}}d\rho\right] \\ &= \sqrt{\frac{2}{\pi r}}\left[2\pi\delta(\omega)q_0 + \hat{q}(\omega) - 2\pi\delta(\omega)\frac{c_a^0 r^2}{R}\right]. \end{aligned} \tag{127}$$

Now, applying all of the above information to Equation (237) yields

$$\begin{aligned} A(\rho,\omega) = \rho^{\frac{1}{2}} &\left[\int_0^1 rF(r;\omega)J_{-\frac{1}{2}}(r\rho)dr \right. \\ &\left. - \int_0^\infty u^{\frac{1}{2}}w(u)A(u,\omega)\left[\frac{uJ_{\frac{1}{2}}(u)J_{-\frac{1}{2}}(\rho) - \rho J_{\frac{1}{2}}(\rho)J_{-\frac{1}{2}}(u)}{u^2-\rho^2}\right]\right] du. \end{aligned} \tag{128}$$

If we use the facts that $J_{-1/2}(x) = \sqrt{\frac{2}{\pi x}}\cos(x)$ and $J_{1/2}(x) = \sqrt{\frac{2}{\pi x}}\sin(x)$ then, we can rewrite Equation (128) as

$$\begin{aligned} A(\rho,\omega) = &\int_0^1 \sqrt{\frac{2r}{\pi}}F(r;\omega)\cos(r\rho)dr \\ &- \frac{2}{\pi}\int_0^\infty w(u)A(u,\omega)\left[\frac{u\sin(u)\cos(\rho) - \rho\sin(\rho)\cos(u)}{u^2-\rho^2}\right] du. \end{aligned} \tag{129}$$

Substituting Equation (127) into Equation (129), and rearranging terms yields

$$\begin{aligned} A(\rho,\omega) = &\frac{2}{\pi}\left[2\pi\delta(\omega)\left(q_0 - \frac{c_a^0}{R}\right) + \hat{q}(\omega)\right]\left[\frac{\sin(\rho)}{\rho}\right] \\ &+ \frac{2}{\pi}\left[2\pi\delta(\omega)\frac{2c_a^0}{R}\right]\left[\frac{\sin(\rho)}{\rho^3} - \frac{\cos(\rho)}{\rho^2}\right] \\ &- \frac{2}{\pi}\int_0^\infty w(u)A(u,\omega)\left[\frac{u\sin(u)\cos(\rho) - \rho\sin(\rho)\cos(u)}{u^2-\rho^2}\right] du. \end{aligned} \tag{130}$$

In order to simplify the notation, we will introduce the spherical Bessel functions of zero and second order. These functions have a relationship to the trigonometric functions as follows [1]

$$j_0(x) = \frac{\sin(x)}{x}, \tag{131a}$$

$$j_2(x) = 3\frac{\sin(x)}{x^3} - 3\frac{\cos(x)}{x^2} - \frac{\sin(x)}{x}. \tag{131b}$$

Therefore, we can rewrite Equation (130) as

$$A(\rho,\omega) = c_0(\omega)j_0(\rho) + c_2(\omega)j_2(\rho) - \frac{1}{\pi}\int_0^\infty w(u)A(u,\omega)K(\rho,u)du, \tag{132}$$

where the kernel function is

$$\begin{aligned} K(\rho,u) &= 2\frac{u\sin(u)\cos(\rho) - \rho\sin(\rho)\cos(u)}{u^2-\rho^2} \\ &= \frac{(u-\rho)(\sin(u)\cos(\rho)+\sin(\rho)\cos(u)) + (u+\rho)(\sin(u)\cos(\rho)-\sin(\rho)\cos(u))}{u^2-\rho^2} \\ &= \frac{(u-\rho)\sin(u+\rho) + (u+\rho)\sin(u-\rho)}{u^2-\rho^2} \\ &= \frac{\sin(u+\rho)}{u+\rho} + \frac{\sin(u-\rho)}{u-\rho} \\ &= j_0(u+\rho) + j_0(u-\rho), \end{aligned} \tag{133}$$

and

$$c_0(\omega) = \frac{2}{\pi}\left[2\pi\delta(\omega)\left(q_0 - \frac{c_a^0}{3R}\right) + \hat{q}(\omega)\right], \tag{134a}$$

$$c_2(\omega) = \frac{2}{\pi}\left[2\pi\delta(\omega)\frac{2c_a^0}{3R}\right]. \tag{134b}$$

This concludes the reduction of the dual integral equations, Equations (122) and (123), to a Fredholm integral equation of the second kind, Equations (132)-(134). In the next section, we will make a linear approximation to the Fredholm integral equation of the second kind, and solve for the linear approximation of the unknown, $A(\rho, \omega)$.

4.8 Approximation of the Fredholm Integral Equation

In order to estimate the integral in Equation (132), we must first take a look at the weight function, $w(\beta)$. Recall from Section 4.5 that $k_s^2 = \frac{\beta_2^2 \omega^2}{\hat{\mu}(\omega)}$. In addition, from Section 3.3, we have that β_2^2 ranges from 10^{-18} to 10^{-24}. Since, ω and $\hat{\mu}(\omega)$ are normalized quantities, then they are order 1. Thus, $\|k_s\| \ll 1$. So, we will perform an asymptotic expansion for $\beta \gg \|k_s\|$ on the weight function. First, Equation (113) can be rewritten as

$$\begin{aligned} \lambda_p &= \left(\beta^2 - k_p^2\right)^{1/2} = \beta \left(1 - \alpha \frac{k_s^2}{\beta^2}\right)^{1/2}, \\ \lambda_s &= \left(\beta^2 - k_s^2\right)^{1/2} = \beta \left(1 - \frac{k_s^2}{\beta^2}\right)^{1/2}, \end{aligned} \tag{135}$$

where we used the fact that $k_p^2 = \alpha k_s^2$. Using a binomial series expansion with $\beta \gg \|k_s\|$ on Equation (135) we obtain

$$\begin{aligned} \lambda_p &= \beta \left(1 - \frac{\alpha}{2} \frac{k_s^2}{\beta^2} - \frac{\alpha^2}{8} \frac{k_s^4}{\beta^4} + \mathcal{O}\left(\frac{k_s^6}{\beta^6}\right)\right), \\ \lambda_s &= \beta \left(1 - \frac{1}{2} \frac{k_s^2}{\beta^2} - \frac{1}{8} \frac{k_s^4}{\beta^4} + \mathcal{O}\left(\frac{k_s^6}{\beta^6}\right)\right). \end{aligned} \tag{136}$$

This allows us to write the asymptotic expansion with $\beta \gg \|k_s\|$ for $\lambda_s \lambda_p$ as

$$\lambda_s \lambda_p = \beta^2 \left[1 - \frac{1}{2} \frac{k_s^2}{\beta^2} (1 + \alpha) - \frac{1}{4} \frac{k_s^4}{\beta^4} \left(\frac{1}{2} - \alpha + \frac{\alpha^2}{2}\right) + \mathcal{O}\left(\frac{k_s^6}{\beta^6}\right)\right]. \tag{137}$$

We may now rewrite Equation (121) as

$$\begin{aligned} w(\beta) &= -1 + \frac{\beta^2 k_s^2 \left[1 - \frac{\alpha}{2}\frac{k_s^2}{\beta^2} - \frac{\alpha^2}{8}\frac{k_s^4}{\beta^4} + \mathcal{O}\left(\frac{k_s^6}{\beta^6}\right)\right]}{4\beta^4 \left[\frac{1}{2}\frac{k_s^2}{\beta^2}(1-\alpha) - \frac{1}{4}\frac{k_s^4}{\beta^4}\left(\frac{3}{2} - \alpha + \frac{\alpha^2}{2}\right) + \mathcal{O}\left(\frac{k_s^6}{\beta^6}\right)\right]} \\ &= -1 + \frac{\left[1 - \frac{\alpha}{2}\frac{k_s^2}{\beta^2} - \frac{\alpha^2}{8}\frac{k_s^4}{\beta^4} + \mathcal{O}\left(\frac{k_s^6}{\beta^6}\right)\right]}{2\left[(1-\alpha) - \frac{1}{2}\frac{k_s^2}{\beta^2}\left(\frac{3}{2} - \alpha + \frac{\alpha^2}{2}\right) + \mathcal{O}\left(\frac{k_s^4}{\beta^4}\right)\right]} \\ &= -1 + \frac{1}{2(1-\alpha)}\left[1 - \frac{\alpha}{2}\frac{k_s^2}{\beta^2} + \mathcal{O}\left(\frac{k_s^4}{\beta^4}\right)\right]\left[\frac{1}{1 - \frac{k_s^2}{\beta^2}\left(\frac{3-2\alpha+\alpha^2}{4(1-\alpha)}\right) + \mathcal{O}\left(\frac{k_s^4}{\beta^4}\right)}\right]. \end{aligned} \tag{138}$$

Using the geometric series expansion for $\frac{k_s^2}{\beta^2} \ll 1$ on the last term in Equation (138) admits

$$\begin{aligned} w(\beta) = -1 + \frac{1}{2(1-\alpha)}&\left[1 - \frac{\alpha}{2}\frac{k_s^2}{\beta^2} + \mathcal{O}\left(\frac{k_s^4}{\beta^4}\right)\right] \\ &\times \left[1 + \frac{k_s^2}{\beta^2}\left(\frac{3-2\alpha+\alpha^2}{4(1-\alpha)}\right) + \mathcal{O}\left(\frac{k_s^4}{\beta^4}\right)\right]. \end{aligned} \tag{139}$$

Therefore, we can write the asymptotic expansion of the weight function for $\beta \gg \|k_s\|$ as

$$w(\beta) = w_1 + \frac{k_s^2}{\beta^2}\left[\frac{3\alpha^2 - 4\alpha + 3}{8(1-\alpha)^2}\right] + \mathcal{O}\left(\frac{k_s^4}{\beta^4}\right), \tag{140}$$

where

$$w_1 = \frac{2\alpha - 1}{2(1-\alpha)}. \tag{141}$$

We will now rewrite Equation (132) as

$$A(\rho,\omega) = A_0(\rho,\omega) - \frac{1}{\pi}\int_0^\infty w_1 A(u,\omega) K(\rho,u)\,du + I_1(A), \tag{142}$$

where

$$A_0(\rho,\omega) = c_0(\omega)j_0(\rho) + c_2(\omega)j_2(\rho), \tag{143}$$

and

$$I_1(A) = -\frac{1}{\pi}\int_0^\infty [w(u) - w_1]\, A(u,\omega)K(\rho,u)du. \tag{144}$$

We will now put a bound on $I_1(A)$ in order to see if we can approximate Equation (132). Thus,

$$\begin{aligned} |I_1(A)| &= \left| -\frac{1}{\pi}\int_0^\infty [w(u) - w_1]\, A(u,\omega)K(\rho,u)du \right| \\ &\le \frac{1}{\pi}\int_0^\infty |w(u) - w_1|\, |A(u,\omega)|\, |K(\rho,u)|\, du. \end{aligned} \tag{145}$$

Now, for any point ρ, we have

$$|K(\rho,u)| = |j_0(u+\rho) + j_0(u-\rho)| \le |j_0(u+\rho)| + |j_0(u-\rho)| \le 1 + 1 = 2. \tag{146}$$

In addition, assuming $A(u)$ continuous and bounded on the interval $u \in (0,\infty)$, then let $M_A = \max_{u\in(0,\infty)} |A(u)|$. Thus,

$$\begin{aligned} |I_1(A)| &\le \frac{2}{\pi} M_A \int_0^\infty |w(u) - w_1|\, du \\ &= \frac{2}{\pi} M_A \left[\int_0^{\beta^*} |w(u) - w_1|\, du + \int_{\beta^*}^\infty |w(u) - w_1|\, du \right], \end{aligned} \tag{147}$$

where $\beta^* \in (0,\infty)$ is an arbitrary point to be chosen later.

Since, $w(u)$ and w_1 continuous on $u \in (0,\beta^*)$, then let $M_w = \max_{u\in(0,\beta^*)} |w(u) - w_1|$. Therefore,

$$\int_0^{\beta^*} |w(u) - w_1|\, du \le \beta^* M_w. \tag{148}$$

Also, for $\beta^* \gg \|k_s\|$ and from Equations (140) and (141) we obtain

$$\int_{\beta^*}^{\infty} |w(u) - w_1|\, du = \int_{\beta^*}^{\infty} \left| \frac{k_s^2}{u^2} \left[\frac{3\alpha^2 - 4\alpha + 3}{8(1-\alpha)^2} \right] + \mathcal{O}\left(\frac{k_s^4}{u^4} \right) \right| du = \mathcal{O}\left(\frac{k_s^2}{\beta^*} \right). \quad (149)$$

Hence,

$$\begin{aligned} |I_1(A)| &\leq \frac{2}{\pi} M_A \left[\beta^* M_w + \mathcal{O}\left(\frac{k_s^2}{\beta^*} \right) \right] \\ &= \frac{2}{\pi} M_A \beta^* \left[M_w + \mathcal{O}\left(\frac{k_s^2}{{\beta^*}^2} \right) \right]. \end{aligned} \quad (150)$$

Therefore, choose $\beta^* = \|k_s\|^\epsilon$, where $0 < \epsilon < 1$. This yields

$$|I_1(A)| \leq \frac{2}{\pi} M_A \|k_s\|^\epsilon \left[M_w + \mathcal{O}\left(\|k_s\|^{2(1-\epsilon)} \right) \right]. \quad (151)$$

Thus, we can choose ϵ such that ϵ is as close to 1 as possible so that we still satisfy $\beta^* \gg \|k_s\|$. Hence, $I_1(A)$ is small and we can approximate Equation (132) to be

$$A(\rho, \omega) = A_0(\rho, \omega) - \frac{1}{\pi} \int_0^\infty w_1 A(u, \omega) K(\rho, u) du. \quad (152)$$

4.9 Solving the Approximation of the Fredholm Integral Equation

We are now going to solve Equation (152) using an integral equation Neumann series. For further explanation of an integral equation Neumann series, see Appendix C. First, define $\lambda^* = -\frac{w_1}{\pi}$, and define the operator

$$Kf(x) = \int_0^\infty K(x, u) f(u) du. \quad (153)$$

Therefore, Equation (152) is now written as

$$A(\beta) = A_0(\beta) + \lambda^* K A(\beta), \quad (154)$$

where we have suppressed the ω dependence where appropriate. Next, define

$$TA = A_0 + \lambda^* KA. \tag{155}$$

Thus, Equation (154) is now written as

$$TA = A. \tag{156}$$

Now, if ϕ_1 and ϕ_2 are in the subspace spanned by $\{j_0, j_2\}$, then

$$\|K\phi_1 - K\phi_2\| = \|K\left(\phi_1 - \phi_2\right)\| = \|\int_0^\infty K(\beta, u)\left(\phi_1(u) - \phi_2(u)\right) du\|. \tag{157}$$

From Appendix D, Equations (255) and (256), we obtain

$$\int_0^\infty K(\beta, u)\left(\phi_1(u) - \phi_2(u)\right) du = \pi\left(\phi_1(\beta) - \phi_2(\beta)\right). \tag{158}$$

Thus,

$$\|K\phi_1 - K\phi_2\| = \|\pi\left(\phi_1 - \phi_2\right)\| = \pi\|\phi_1 - \phi_2\|. \tag{159}$$

Therefore, we see from Appendix C that for uniqueness and convergence we require that $|\lambda^*|\pi < 1$. Thus, in order to use the integral equation Neumann series we require that $|w_1| < 1$.

Let's assume for now that $|w_1| < 1$. By the integral equation Neumann series we obtain

$$A = A_0 + \lambda^* KA_0 + \lambda^{*2} K^2 A_0 + \cdots + \lambda^{*n} K^n A_0 + \cdots. \tag{160}$$

Using Equations (255) and (256) from Appendix D, we obtain

$$KA_0 = \pi A_0, \tag{161}$$

$$K^2 A_0 = \pi K A_0 = \pi^2 A_0, \tag{162}$$

and

$$K^n A_0 = \pi^n A_0. \tag{163}$$

Thus,

$$A = A_0 - w_1 A_0 + (-w_1)^2 A_0 + \cdots + (-w_1)^n A_0 + \cdots = A_0 \sum_{k=0}^{\infty} (-w_1)^k . \tag{164}$$

Using the assumption that $|w_1| < 1$, the definition of an infinite geometric series, and Equation (141), we can write Equation (164) as

$$A = A_0 \frac{1}{1 + w_1} = 2(1 - \alpha) A_0. \tag{165}$$

Here, we recall that $\alpha = \frac{\hat{\mu}}{\hat{\lambda} + 2\hat{\mu}}$. So, $w_1 = \frac{-\hat{\lambda}}{2(\hat{\lambda} + \hat{\mu})}$ or $|w_1| = \frac{1}{2} \left| \frac{\hat{\lambda}}{\hat{\lambda} + \hat{\mu}} \right|$. We will show that $|w_1| < 1$ in Section 4.11.

With an approximation to $A(\beta)$, we can obtain all the $A_i(\beta)$'s using Equations (124) and (125). Thus, using Equation (112), we can calculate $\vec{G}$. Assuming we can take the appropriate inverses then, we have a solution to our reduced, three-dimensional material model.

4.10 Finite Stress at the Contact Area Boundary

In order to relate the static penetration depth to properties of the AFM and surface system, we will go back and take a closer look at the normal stress in the Fourier transform domain at the boundary $\xi = 0$. To do this, examine the Fourier transform of Equation (85) with $\xi = 0$ then,

$$\hat{\sigma}_{\xi\xi}(\rho, 0, \omega) = E_0 \left[\hat{\lambda}(\omega) + 2\hat{\mu}(\omega) \right] \int_0^{\infty} \beta J_0(\beta\rho) \left[\hat{g}_{\xi}'(0) + \bar{\alpha}\beta \hat{g}_{\rho}(0) \right] d\beta. \tag{166}$$

Next, recall from Equation (119) that $\hat{g}'_\xi(0) + \bar{\alpha}\beta\hat{g}_\rho(0) = -\alpha A(\beta)$. Also, using Equation (165), $-\alpha A(\beta) \approx -2\alpha(1-\alpha)A_0(\beta)$. So, Equation (166) becomes

$$\hat{\sigma}_{\xi\xi}(\rho, 0, \omega) \approx -2E_0\hat{\mu}(\omega)(1-\alpha)\int_0^\infty \beta J_0(\beta\rho)\left[c_0 j_0(\beta) + c_2 j_2(\beta)\right] d\beta, \tag{167}$$

where we have used the facts that $\alpha = \frac{\hat{\mu}}{\hat{\lambda}+2\hat{\mu}}$ and $A_0(\beta) = c_0 j_0(\beta) + c_2 j_2(\beta)$. Now, using Equations (257) and (258) from Appendix D yields

$$\hat{\sigma}_{\xi\xi}(\rho, 0, \omega) \approx -2E_0\hat{\mu}(\omega)\frac{(1-\alpha)}{\sqrt{1-\rho^2}}\begin{cases} c_0 + c_2\left(2 - 3\rho^2\right), & 0 < \rho < 1, \\ 0, & 1 < \rho. \end{cases} \tag{168}$$

Substituting Equations (134) into Equation (168) produces

$$\begin{aligned}\hat{\sigma}_{\xi\xi}(\rho, 0, \omega) &\approx -\frac{4}{\pi}E_0\hat{\mu}(\omega)\frac{(1-\alpha)}{\sqrt{1-\rho^2}}\left[2\pi\delta(\omega)\left(q_0 + \frac{c_a^0}{R}(1-2\rho^2)\right) + \hat{q}(\omega)\right] \\ &= \hat{\sigma}^s_{\xi\xi}(\rho, 0) + \hat{\sigma}^d_{\xi\xi}(\rho, 0, \omega),\end{aligned} \tag{169}$$

for $0 < \rho < 1$. Since the forcing function for the experiment is made up of a static preload and a dynamic tapping piece, we would expect that for this linear model, the stress will also be composed of a static piece and a dynamic piece. Thus,

$$\hat{\sigma}^s_{\xi\xi}(\rho, 0) = -\frac{4}{\pi}E_0\hat{\mu}(\omega)\frac{(1-\alpha)}{\sqrt{1-\rho^2}}\left[2\pi\delta(\omega)\left(q_0 + \frac{c_a^0}{R}(1-2\rho^2)\right)\right] \tag{170}$$

represents the static component of the stress, and

$$\hat{\sigma}^d_{\xi\xi}(\rho, 0, \omega) = -\frac{4}{\pi}E_0\hat{\mu}(\omega)\frac{(1-\alpha)}{\sqrt{1-\rho^2}}\left[\hat{q}(\omega)\right] \tag{171}$$

represents the dynamic component of the stress.

Notice that at the edge of the contact region, $\rho = 1$, the stress becomes infinite unless q_0 is chosen appropriately. In addition, the solution should be continuous at the contact boundary. To keep the static component of stress finite at the contact boundary, q_0 is chosen such that the static stresses vanish at $\rho = 1$. This leads to the choice $q_0 = \frac{c_a^0}{R}$. The choice of finite and continuous stress at the contact boundary is the same as the approximation made by Hertz [84]. The equation for normal stress at the boundary, $\xi = 0$, and within the contact area, $0 < \rho < 1$, becomes

$$\hat{\sigma}_{\xi\xi}(\rho, 0, \omega) \approx \frac{-8c_a^0}{\pi R} E_0 \hat{\mu}(\omega)(1-\alpha) \left[2\pi\delta(\omega)\sqrt{1-\rho^2} + \frac{R}{2c_a^0} \frac{\hat{q}(\omega)}{\sqrt{1-\rho^2}} \right]. \tag{172}$$

Although there is no term that we may choose to balance the dynamic stress at $\rho = 1$, we shall see that over the total contact area, the force generated by the dynamic stress is finite. This also means that the dynamic contact stress between the parabolic tip and the surface, when the static force is much greater than the dynamic force, is equivalent to that of a rigid flat punch with the surface [90, 84, 91].

In order to calculate the force generated by the dynamic stress, we combine Equations (102), (119), and (165) to obtain

$$\hat{F}_\sigma(\omega) \approx -4\pi\hat{\mu}(\omega)(1-\alpha) \int_0^\infty J_1(\beta) \left[c_0 j_0(\beta) + c_2 j_2(\beta) \right] d\beta, \tag{173}$$

where we have used the facts that $\alpha = \frac{\hat{\mu}}{\hat{\lambda}+2\hat{\mu}}$ and $A_0(\beta) = c_0 j_0(\beta) + c_2 j_2(\beta)$. Now, using Equations (259) and (260) from Appendix D, and Equations (134), we can write

$$\hat{F}_\sigma(\omega) \approx -8\hat{\mu}(\omega)(1-\alpha) \left[2\pi\delta(\omega) \left(\frac{2c_a^0}{3R} \right) + \hat{q}(\omega) \right]. \tag{174}$$

We have now reduced the system of equations to the solution of Equations (99)-(104), where the transformed force exerted by the surface on the AFM tip is approximated as in Equation (174).

4.11 Solving the Reduced Model

Since we are interested in solving for the movement of the AFM tip in order to compare our mathematical model to the experimental data then, we will solve the reduced system of Equations (99)-(104) along with Equation (174). In order to do this, we will need to take the inverse Fourier transform of our system of equations. To do this, we need to fix Poisson's ratio to be a constant, then we can write $\hat{\lambda}(\omega)$ and $\hat{\mu}(\omega)$ in terms of Poisson's ratio, ν, and the Young's modulus of the material, $\hat{E}(\omega)$. This also allows us to calculate $\alpha(\omega) = \alpha = \frac{\hat{\mu}}{\hat{\lambda}+2\hat{\mu}}$, where α is no longer a function of frequency.

For a viscoelastic material, Poisson's ratio is usually a function of frequency because the transverse strain may be out of phase with the longitudinal strain. For the solution of the current system of equations, we assume that this difference in strains is minimal so that Poisson's ratio is a constant with respect to frequency. It will also be important to note that $-1 < \nu < .5$. So, from Findley et al. [24] we have

$$\hat{\lambda}(\omega) = \frac{-\nu \hat{E}(\omega)}{(1+\nu)(2\nu-1)} \tag{175}$$

and

$$\hat{\mu}(\omega) = \frac{\hat{E}(\omega)}{2(1+\nu)}. \tag{176}$$

This admits to

$$\alpha = \frac{1-2\nu}{2(1-\nu)}. \tag{177}$$

At this point, we shall take a look at $w_1 = \frac{-\hat{\lambda}}{2(\hat{\lambda}+\hat{\mu})}$. Recall from Section 4.9 that we require $|w_1| < 1$. Using Equations (175) and (176) we obtain

$$w_1 = -\nu. \tag{178}$$

Thus, $|w_1| < 1$.

Substituting Equations (175)-(177) into Equation (174) yields

$$\hat{F}_\sigma(\omega) \approx \frac{-2\hat{E}(\omega)}{1-\nu^2}\left[2\pi\delta(\omega)\left(\frac{2c_a^0}{3R}\right) + \hat{q}(\omega)\right]. \tag{179}$$

The static piece from the above equation is precisely the viscoelastic correspondence of the Hertz solution in terms of force [84].

Now, substituting Equation (179) into Equation (99), using the fact that $q_0 = \frac{c_a^0}{R}$, and collecting terms gives

$$\left[L_0(\omega) + P_0(\omega)\right]\hat{q}(\omega) = 2\pi\delta(\omega)\left[B_0 - \frac{c_a^0}{R}\left(1 + \frac{2}{3}P_0(\omega)\right)\right] + BS(\omega, \phi), \tag{180}$$

where

$$P_0(\omega) = \frac{2\hat{E}(\omega)}{(1-\nu^2)}\chi. \tag{181}$$

Recall from Section 3.3 that $\chi = \frac{c_a^0 E_0}{k}$.

So, taking the inverse Fourier transform of Equation (180), and equating the static and dynamic terms gives

$$B_0 = \frac{c_a^0}{R}\left[1 + \frac{2}{3}P_0(0)\right], \tag{182}$$

and

$$q(t^*) = \left(\frac{B}{2i(L_0(1) + P_0(1))}\right)e^{i(t^*+\phi)} - \left(\frac{B}{2i(L_0(-1) + P_0(-1))}\right)e^{-i(t^*+\phi)}. \tag{183}$$

Equations (181)-(183) represent the solution to the scaled, reduced, three-dimensional system.

4.12 Analysis of the Reduced Three-Dimensional Model

Let's start off by taking a closer look at $L_0(\omega)$ from Equation (101). First, we recall that β_1 is the ratio of the resonant frequency of the AFM, ω_0, to the modulation frequency, ω_2, so that $\beta_1 = \frac{\omega_0}{\omega_2}$ is in the range of 25 to 25×10^3 which, is large compared to unity. Also note that $Q \sim 100$. So, Equation (101) can be approximated by $L_0(\omega) \approx 1$ for $\omega = 0, \pm 1$.

In addition, define $E_0^* = \frac{E_0}{1-\nu^2}$, which is the elastic, plane strain Young's modulus. Thus, Equation (181) can be written as

$$P_0(\omega) = 2\chi^* \hat{E}(\omega), \tag{184}$$

where $\chi^* = \frac{c_a^0 E_0^*}{k}$ is a dimensionless ratio. Therefore, we can write Equation (182) as

$$B_0 = \frac{c_a^0}{R} + \frac{4{c_a^0}^2 E_0^*}{3Rk}\hat{E}(0). \tag{185}$$

Here we note that $\hat{E}(0)$ represents the static, normalized viscoelastic Young's modulus so, $\hat{E}(0) = 1$. Thus, Equation (185) becomes

$$B_0 = \frac{c_a^0}{R} + \frac{4{c_a^0}^2 E_0^*}{3Rk}. \tag{186}$$

So, the difference between B_0 and $q_0 = \frac{c_a^0}{R}$ yields

$$B_0 - \frac{c_a^0}{R} = \frac{4{c_a^0}^2 E_0^*}{3Rk}. \tag{187}$$

Here, $q_0 = \frac{c_a^0}{R}$ represents the dimensionless penetration depth of the AFM tip into the surface, and B_0 represents the dimensionless distance caused by the static loading, i.e., the preload. Thus, the left hand side of Equation (187) represents the difference of the static loading and the tip penetration into the material. We know that this difference is caused by various physical properties of the AFM and the material. Examples of these are the AFM's tip curvature radius and its effective stiffness, as well as the contact area radius and the Young's modulus of the material.

The right hand side of Equation (187), is a ratio of forces. The numerator represents the force the material exerts on the tip over the whole contact area. The denominator represents the force of the effective AFM spring constant the length of the tip curvature radius. In other words, we have the ratio of the force the surface exerts on the tip to the force the tip exerts on the surface. Note, that all the terms in this ratio are properties of the AFM and the material, as we expected.

Moving on to the dynamic portion of the system, we see that Equation (183) becomes

$$q(t^*) = \frac{B}{2i}\left[\left(\frac{1}{1+2\chi^*\hat{E}(1)}\right)e^{i(t^*+\phi)} - \left(\frac{1}{1+2\chi^*\hat{E}(-1)}\right)e^{-i(t^*+\phi)}\right]. \tag{188}$$

If $\hat{E}(1)$ and $\hat{E}(-1)$ are complex conjugates, which is the case for the viscoelastic Kelvin-Voigt and Maxwell models, as well as the generalized viscoelastic polynomial model, then we can write Equation (188) as

$$q(t^*) = \frac{B}{|1+2\chi^*\hat{E}(1)|}\sin(t^*+\phi+\phi_1), \tag{189}$$

where

$$\phi_1 = \arctan\left(\frac{\Im\left(\frac{1}{1+2\chi^*\hat{E}(1)}\right)}{\Re\left(\frac{1}{1+2\chi^*\hat{E}(1)}\right)}\right). \tag{190}$$

Here, we see that the amplitude of the dimensionless, dynamic penetration depth, $q(t^*)$, is directly proportional to the dynamic forcing amplitude, B. We also see that the amplitude depends on material properties and AFM properties through χ^*

and $\hat{E}(1)$. Both of these observations make sense physically. We would expect the dynamic penetration depth to be smaller in magnitude than the dynamic forcing amplitude because the surface will resist the tip, causing the tip to not penetrate to the full depth of the forcing amplitude. We would also expect that the material properties and the AFM properties would help to determine the penetration depth.

We also see that the dynamic tip movement is sinusoidal as is the forcing but, the material properties and the AFM properties add a phase shift. This is to be expected as the system is not an instantaneous elastic system but, rather it's a viscoelastic system. We also observe that ϕ_1 is a function of our forcing frequency, ω_2, by means of the viscoelastic modulus, $\hat{E}(1)$.

This chapter presented some background material on infinite and semi-infinite, three-dimensional material models and dual integral equations. We then made appropriate assumptions in order to reduce the system of equations that represents the experiment. These assumptions eventually allowed us to solve the equations in the transform domain. We then inverted the transformed equations to obtain the solution to the system in an analytical form. Finally, we analyzed the system. In the next chapter, we will present a new model that will allow us to bring together the system model and the actual experimental setup. We will then compare the combined model to experimental data.

V. Application of Models to AFM Measurements

In order to compare the reduced three-dimensional model to the AFM experimental data, we will introduce a model called the “error model”. This model will allow us to solve for the penetration depth of the AFM tip into a material using AFM experimental data. This will allow us to directly equate the analytical system model solution for the penetration depth to the error model solution for the penetration depth. This will yield an analytical solution for the viscoelastic material parameters in terms of AFM experimental data. We note that the analytical solution may have wide applicability to other problems but, we will make application to a specific problem. In particular, we will present results from data collected for a polystyrene thin film on a silicon substrate.

5.1 Error Model

Recall that the experiment we have been modeling is described in section 1.2. Let the initial state of the system be with the AFM cantilever tip ‘just resting’ on the sample surface, i.e., with no applied loading. Let the surface to air boundary be at $z = 0$, with the positive z-direction in the inward normal direction to the surface. A laser beam is reflected off the tip end of the cantilever and onto the AFM detector. In the initial state, the AFM detector records a small voltage due to surface adhesion and other small forces between the surface and the AFM tip. The AFM detector actually measures the position of the top of the cantilever. However, assuming the length of the tip of the cantilever remains constant throughout the experiment, the voltage recorded at the AFM detector is the position of the tip relative to the original surface, denoted $z(t; \omega_2)$, where t is time and ω_2 is a tapping frequency.

In the experiment, an initial DC voltage, $\hat{Q}_{DC}$, is applied to the piezo. Assuming the silicon base, which rests atop the piezo, is perfectly rigid and perfectly bonded to the sample, the piezo movement is transferred into the sample. Further, the top surface of the sample moves the exact same distance. This distance is determined via $\frac{\hat{Q}_{DC}}{g_p}$ through the calibration constant g_p, which converts the voltage of the piezo into a displacement. For the piezo used in this experiment, $g_p = \frac{24}{5368}$ volts per nanometer. The AFM bends against and slightly penetrates the surface but, because of the viscoelasticity of the surface, there is some creep after the initial voltage displacement. After some time, the AFM tip and the surface reach "near" equilibrium, i.e., steady state with a small drift. When this equilibrium position is measured at the AFM detector, we call this the set point voltage, or preload voltage, $\hat{L}$.

A manual gain is set at the AFM detector called the modulation voltage bias, $\hat{\gamma}$. This tells the closed-loop, computer controlled feedback system within what range of the preload voltage to achieve, when measured at the AFM detector. After equilibrium is reached, an initial sinusoidal voltage is applied to the piezo at a frequency of ω_2. The closed-loop, computer controlled feedback system determines an amplitude of forcing and a phase shift that modifies the initial modulation in order to maintain the set point voltage to within the modulation voltage bias. The modulation voltage bias is established as the reference phase. The first lock-in-amplifier records the AC error voltage amplitude, $\hat{P}(\omega_2)$, and phase, $\theta_p(\omega_2)$, which are the differences in voltage amplitudes and phases between the modulation voltage bias and the voltage measured at the AFM detector. This represents the error signal between the cantilever tip location, as driven by the computer controller, and the actual tip position. This error signal is attributable to properties of the surface and the piezo system.

In addition to the calibration constant g_p, which converts piezo voltages into displacements, there is another calibration constant g_a, which converts the voltages of the error signal and modulation voltage to cantilever displacements. For the experiment being examined $g_a = \frac{1}{84}$ volts per nanometer.

The DC part of the error displacement, $\frac{\hat{P}_{DC}}{g_a}$, is the difference between the set point displacement, $\frac{\hat{L}}{g_a}$, and the static AFM, $z(t;0)$, i.e.,

$$\frac{\hat{P}_{DC}}{g_a} = \frac{\hat{L}}{g_a} - z(t;0). \tag{191}$$

At equilibrium, $\hat{P}_{DC} = 0$, so it follows that $z(t;0) = \frac{\hat{L}}{g_a}$.

The entire experimental system is nonlinear, which means the total response of the system has multiple natural modes of oscillation, i.e., the tapping frequency is the sole forcing function whereas the resultant system response occurs at multiple frequencies, including the tapping frequency. For the experiment, the response of the error and the computer controlled feedback is measured by means of a LIA only at the forced oscillation frequency, ω_2. Thus, the error of the system can be represented by

$$\frac{\hat{P}_{DC}}{g_a} + \frac{\hat{P}(\omega_2)}{g_a}\sin\left(\omega_2 t + \theta_p(\omega_2)\right) = \frac{\hat{L}}{g_a} + \frac{\hat{\gamma}}{g_a}\sin\left(\omega_2 t\right) - z(t;\omega_2). \tag{192}$$

The left hand side of Equation (192) represents the error, while the first two terms on the right hand side represent the piezo movement. Finally, $z(t;\omega_2)$ is the AFM movement relative to the original surface position.

Solving Equation (192) for the position of the cantilever tip produces

$$z(t) = \frac{\hat{L}}{g_a} + \frac{\hat{C}}{g_a}\sin\left(\omega_2 t + \theta_C\right), \tag{193}$$

where

$$\hat{C} = \left[\hat{\gamma}^2 + \hat{P}^2 - 2\hat{\gamma}\hat{P}\cos\left(\theta_p\right)\right]^{1/2}, \tag{194}$$

and

$$\theta_C = \arctan\left(\frac{-\hat{P}\sin(\theta_p)}{\hat{\gamma} - \hat{P}\cos(\theta_p)}\right). \tag{195}$$

Note, we have suppressed the ω_2 dependence on the appropriate variables, and taken advantage of the fact that $\hat{P}_{DC} = 0$. The term $\hat{C}$ represents the voltage amplitude of the AFM tip position, and θ_C represents the phase shift of the AFM tip in reference to the driving signal. Both terms can be calculated from experimental data.

In order to relate the reduced three-dimensional model from Chapter IV, to the error model, it is necessary to relate the AFM tip movement to the penetration depth. To this end, let $z(t) = z_0 + z_1(t)$ be the AFM tip displacement, and $y(t) = y_0 + y_1(t)$ be the penetration depth, then z_0 and y_0 represent the static tip location and the penetration depth of the cantilever tip based solely on the preload voltage, respectively. Further, $z_1(t)$ and $y_1(t)$ represent the dynamic portion of the cantilever tip movement and the dynamic penetration depth based on the modulation signal, respectively. When the system reaches dynamic equilibrium, the surface of the material in contact with the AFM has moved in the negative z-direction, a distance $\frac{\hat{Q}_{DC}}{g_p}$. So, the static penetration depth of the AFM tip is

$$y_0 = \frac{\hat{Q}_{DC}}{g_p} - z_0 = \frac{\hat{Q}_{DC}}{g_p} - \frac{\hat{L}}{g_a}. \tag{196}$$

Here, y_0 represents the positive, static, penetration depth of the AFM tip into the sample surface.

After static equilibrium is reached, the initial modulation and the computer feedback voltages are applied to the piezo. The second lock-in-amplifier measures this combined piezo forcing. Specifically, the LIA measures the piezo amplitude voltage, $\hat{Q}(\omega_2)$, and piezo phase shift, $\theta_Q(\omega_2)$. Since the piezo is a crystal, there is a time delay associated with contraction or expansion due to an applied voltage. This delay in contraction or expansion is called the piezo delay time, $\tau_p(\omega_2)$, and it is a function of the forcing frequency. Because of the assumed perfectly rigid silicon base, and perfect bonding to the sample, all the piezo movement is transferred into surface movement. This surface movement doesn't occur until after the piezo delay time. Thus, the dynamic AFM tip position is not affected until after the piezo delay time. This leads to the equation for the dynamic penetration depth as

$$\begin{aligned} y_1(t) &= \frac{\hat{Q}}{g_p}\sin\left(\omega_2(t-\tau_p)+\theta_Q\right) - z_1(t) \\ &= \frac{\hat{Q}}{g_p}\sin\left(\omega_2(t-\tau_p)+\theta_Q\right) - \frac{\hat{C}}{g_a}\sin\left(\omega_2 t+\theta_C\right). \end{aligned} \tag{197}$$

Here, $y_1(t)$ is the oscillation of the tip penetration depth around the static tip penetration depth, y_0.

Recalling from Section 3.3 that $y(t) = c_a^0(q_0 + q(t^*))$, Equations (196) and (197) can be written as dimensionless equations. This leads to the cantilever movement based on the error model as

$$q_0 = Q_{DC} - L, \tag{198}$$

from Equation (196), and

$$q(t^*) = Q\sin\left(t^* - \tau_p^* + \theta_Q\right) - C\sin\left(t^* + \theta_C\right), \tag{199}$$

from Equation (197). Here, $Q_{DC} = \frac{\hat{Q}_{DC}}{g_p c_a^0}$, $L = \frac{\hat{L}}{g_a c_a^0}$, $Q = \frac{\hat{Q}}{g_p c_a^0}$, $C = \frac{\hat{C}}{g_a c_a^0}$, $t^* = \omega_2 t$, and $\tau_p^* = \omega_2\tau_p$. The terms Q_{DC} and L are the dimensionless static distances generated by the piezo and the preload, respectively. The terms Q and C are the dimensionless dynamic displacement amplitudes generated by the piezo and the AFM movement, respectively. Finally, t^* is dimensionless time, and τ_p^* is the dimensionless piezo delay time.

5.2 Equating the Models

Now, the dimensionless penetration depth from the reduced three-dimensional model, and the dimensionless penetration depth from the error model, can be equated. Before doing so, we must first define B_0, B, and ϕ, as in Equation (67), in terms of the error model parameters. Recalling Equation (67), we see that B_0 represents the dimensionless static loading that occurs at the AFM, B represents the dimensionless dynamic amplitude that occurs at the AFM, and ϕ represents the phase shift at the AFM, as compared to the reference phase. Since, Q_{DC} represents the dimensionless displacement due to static loading at the piezo, and the substrate is assumed perfectly bonded to a perfectly rigid silicon base, the movement at the top ($z = 0$) of the material surface is Q_{DC}. So, the dimensionless static forcing is $B_0 = Q_{DC}$. By the same argument, the dimensionless dynamic amplitude of the system is $B = Q$. When a voltage is applied to the piezo crystal, movement at the top surface of the sample is delayed by the piezo delay time, τ_p. In addition, the voltage applied to the piezo is phase shifted from the reference signal by θ_Q. Thus, the phase shift is $\phi = \theta_Q - \tau_p^*$.

The static portion of the reduced three-dimensional model, Equation (186), is now written as

$$Q_{DC} = \frac{c_a^0}{R} + \frac{4{c_a^0}^2 E_0^*}{3Rk}. \tag{200}$$

Substituting Equation (200) into Equation (198), and using the fact that $q_0 = \frac{c_a^0}{R}$, we can solve for the dimensionless preload as

$$L = \frac{4{c_a^0}^2 E_0^*}{3Rk} = \frac{4}{3} q_0 \chi^*. \tag{201}$$

Equation (201) says that the dimensionless preload, L, is equal to a constant times the ratio of the force the surface exerts on the tip, ${c_a^0}^2 E_0^*$, to the force the tip exerts on the surface, Rk. Using Equations (198) and (201), we can solve for the unknown,

χ^*, producing

$$\chi^* = \frac{3}{4}\left[\frac{L}{Q_{DC} - L}\right] = \frac{3}{4}\left[\frac{\hat{L}}{\frac{g_a}{g_p}\hat{Q}_{DC} - \hat{L}}\right]. \tag{202}$$

Equation (202) allows for the calculation of χ^* based on experimental data. This constant, χ^*, is independent of frequency and is strictly a positive, real number. Additionally, using $q_0 = \frac{c_a^0}{R}$, we can solve Equation (198) for c_a^0 to obtain

$$c_a^0 = \left[R\left(\frac{\hat{Q}_{DC}}{g_p} - \frac{\hat{L}}{g_a}\right)\right]^{1/2}. \tag{203}$$

Using Equations (202) and (203), and solving for E_0^* based on the experimental data results in

$$E_0^* = \frac{3k\hat{L}}{4}\left[\frac{g_a}{R}\right]^{1/2}\left[\frac{g_a}{g_p}\hat{Q}_{DC} - \hat{L}\right]^{-3/2}. \tag{204}$$

The dynamic portion of the reduced three-dimensional model, Equation (189), is now written as

$$q(t^*) = \frac{Q}{|1 + 2\chi^*\hat{E}(1)|}\sin(t^* + \theta_Q - \tau_p^* + \phi_1). \tag{205}$$

Substituting Equation (205) into Equation (199) yields

$$\frac{Q}{|1 + 2\chi^*\hat{E}(1)|}\sin(t^* + \theta_Q - \tau_p^* + \phi_1) = Q\sin\left(t^* + \theta_Q - \tau_p^*\right) - C\sin\left(t^* + \theta_C\right). \tag{206}$$

Here, the left hand side of Equation (206) represents the dynamic portion of the penetration depth from the reduced three-dimensional model, and the right hand side represents the dynamic portion of the penetration depth from the error model. For convenience, let $x = t^* + \theta_Q - \tau_p^*$, and combine the sine terms on the right hand side of Equation (206), to obtain

$$\frac{Q}{|1 + 2\chi^*\hat{E}(1)|}\sin(x + \phi_1) = D\sin\left(x + \phi_2\right), \tag{207}$$

where

$$D = \left[Q^2 + C^2 - 2CQ\cos\left(\theta_C - \theta_Q + \tau_p^*\right)\right]^{1/2}, \tag{208}$$

and

$$\phi_2 = \arctan\left(\frac{-C\sin(\theta_C - \theta_Q + \tau_p^*)}{Q - C\cos(\theta_C - \theta_Q + \tau_p^*)}\right). \tag{209}$$

For equality to hold in Equation (207), the amplitudes and the phases must match. This leads to

$$\frac{Q}{|1 + 2\chi^*\hat{E}(1)|} = D, \tag{210}$$

and

$$\phi_1 = \arctan\left(\frac{\Im\left(\frac{1}{1+2\chi^*\hat{E}(1)}\right)}{\Re\left(\frac{1}{1+2\chi^*\hat{E}(1)}\right)}\right) = \arctan\left(\frac{-C\sin(\theta_C - \theta_Q + \tau_p^*)}{Q - C\cos(\theta_C - \theta_Q + \tau_p^*)}\right) = \phi_2. \tag{211}$$

From Equation (211) we get

$$\frac{\Im\left(\frac{1}{1+2\chi^*\hat{E}(1)}\right)}{\Re\left(\frac{1}{1+2\chi^*\hat{E}(1)}\right)} = \frac{-C\sin(\theta_C - \theta_Q + \tau_p^*)}{Q - C\cos(\theta_C - \theta_Q + \tau_p^*)}. \tag{212}$$

Equations (202), (210), and (212) represent the analytical solution to the experimental system. The remaining unknowns to be solved for are the model parameters from whichever viscoelastic model we choose to represent the sample surface.

5.3 Analysis of the Experimental Model

Now that we have the solution to the experimental system, Equations (202), (210), and (212), we can proceed to analyze the model and solve for the unknown viscoelastic material parameters. First, observe from Equation (202), we have the solution for χ^* in terms of the experimental data, $\hat{L}$ and $\hat{Q}_{DC}$. Next, we analyze Equations (210) and (212), by letting the term $1 + 2\chi^*\hat{E}(1) = a + bi$, a complex number. Note, that both

a and b can be frequency dependent, and $a = 1 + 2\chi^* \Re(\hat{E}(1))$ and $b = 2\chi^* \Im(\hat{E}(1))$. Thus, we can write Equation (212) as

$$\frac{-b}{a} = \frac{-C \sin(\theta_x)}{Q - C \cos(\theta_x)}, \tag{213}$$

where we have let $\theta_x = \theta_C - \theta_Q + \tau_p^*$. Solving this equation for b in terms of a yields

$$b = a \frac{C \sin(\theta_x)}{Q - C \cos(\theta_x)}. \tag{214}$$

Turning our attention to Equation (210), produces

$$\left(\frac{Q}{D} \right)^2 = a^2 + b^2. \tag{215}$$

Substituting Equation (214) into Equation (215) we obtain

$$\left(\frac{Q}{D} \right)^2 = a^2 \left[1 + \left(\frac{C \sin(\theta_x)}{Q - C \cos(\theta_x)} \right)^2 \right] = a^2 \left[\frac{D}{Q - C \cos(\theta_x)} \right]^2. \tag{216}$$

Solving Equation (216) for a yields

$$a = \frac{Q \left(Q - C \cos(\theta_x) \right)}{D^2}. \tag{217}$$

Equation (217) is related to the real part of the viscoelastic model in terms of experimental data. We may now substitute Equation (217) into Equation (214) to obtain

$$b = \frac{CQ \sin(\theta_x)}{D^2}. \tag{218}$$

Equation (218) is related to the imaginary part of the viscoelastic model in terms of experimental data.

Up until this point, no specific material model has been imposed, i.e., $\hat{\lambda}(\omega)$ and

$\hat{\mu}(\omega)$ were related through Poisson's ratio to $\hat{E}(\omega)$. This relationship is stated in Equations (175) and (176). From the discussion in Section 3.1, $\hat{E}(\omega)$ can take on many forms, which depend on the behavior of the material. In order to obtain meaningful information from Equations (217) and (218), we will choose to represent the viscoelastic model as a general polynomial model as in Equation (52). Thus, let $\hat{E}(\omega) = p(\omega\omega_2) + iq(\omega\omega_2)$. Therefore, $\hat{E}(1) = p(\omega_2) + iq(\omega_2)$. We note that $\hat{E}(0) = p(0) + iq(0)$. Recall from Section 4.12 that we require $\hat{E}(0) = 1$, which leads to $p(0) = 1$ and $q(0) = 0$. Therefore, equating a and b to the general viscoelastic model gives

$$a = 1 + 2\chi^* p(\omega_2), \tag{219}$$

and

$$b = 2\chi^* q(\omega_2). \tag{220}$$

Using Equations (217) and (219) we can solve for $p(\omega_2)$ to obtain

$$p(\omega_2) = \frac{CQ\cos(\theta_x) - C^2}{2\chi^* D^2}. \tag{221}$$

In addition, using Equation (218) and (220), we can solve for $q(\omega_2)$ to obtain

$$q(\omega_2) = \frac{CQ\sin(\theta_x)}{2\chi^* D^2}. \tag{222}$$

Equations (221) and (222) represent the solution to the viscoelastic model parameters in terms of experimental data. Keep in mind that we require $p(0) = 1$ and $q(0) = 0$. We will address these issues in the following section but, before we do so, we must first discuss the experimental data.

5.4 Further Analysis and Comparison to the Experimental Data

Now that we have the solution of the model parameters related to the experimental data, Equations (202), (221), and (222), we can use the experimental data to generate useful information about the nanoscale surface material properties. We shall analyze the model and the experiment in two pieces. These are the static piece, and the dynamic piece.

5.4.1 Static Piece.

First, we shall concentrate on χ^*, which comes from the static portion of the experimental data. In the experiment, Q_{DC} was not measured so, we will have to assume that we know one of the model parameters. In this case, the material in the experiment is polystyrene. Polystyrene has a published value for the Young's modulus of about 3 GPa, and a Poisson's ratio of about $\frac{1}{3}$. Thus, the plane strain Young's modulus for polystyrene is $E_0^* = 3.375$ GPa.

Under the assumption that E_0^* is known, we will use Equation (201) to solve for the unknown parameter, c_a^0, to obtain

$$c_a^0 = \left[\frac{3Rk\hat{L}}{4g_a E_0^*}\right]^{\frac{1}{3}}, \tag{223}$$

where we have used the fact that $L = \frac{\hat{L}}{g_a c_a^0}$. Next, substitute Equation (223) into $\chi^* = \frac{c_a^0 E_0^*}{k}$ to obtain

$$\chi^* = \left[\frac{3R\hat{L}}{4g_a}\right]^{\frac{1}{3}} \left[\frac{E_0^*}{k}\right]^{\frac{2}{3}}. \tag{224}$$

This allows us to estimate χ^* given the surface's plane strain Young's modulus, E_0^*.

Knowing the effective cantilever stiffness for the experiment, $k = 0.06$ N/m, the tip curvature radius, $R = 30$ nm, and the preload voltage, $\hat{L} = 0.25$ V, we can use

Table 2. χ^* **at various preloads.**

$\hat{L}$	χ^*
0.25 V	114.34
0.5 V	144.07
1.0 V	181.51
2.0 V	228.69
3.0 V	261.78

Equation (224) to estimate $\chi^* = 114.34$. In the experiment, various preloads that range in value from .25 V to 5.4 V were used. Table 2 lists several estimated values of χ^*.

We see from Table 2 and from Equation (224) that as the preload is increased, χ^* also increases. Since the effective cantilever spring constant and the plane strain Young's modulus of the material remain constant, c_a^0 is directly proportional to χ^* through $c_a^0 = \chi^* \frac{k}{E_0^*}$. Thus, as we increase our preload voltage, the average contact area radius must increase. This is precisely what we would expect to happen when we apply a greater DC loading.

5.4.2 Dynamic Piece.

Now that we have estimated the values of χ^* for various preload voltages, we can move on to looking at the viscoelastic material model parameters. First, we must examine the data taken from the experiment. This data is represented in terms of the error amplitude, $\hat{P}$, and phase, θ_p, as well as the piezo signal amplitude, $\hat{Q}$, and phase, θ_Q. Three sets of data were collected. Each set of data corresponds to a different thickness of the polystyrene surface. The surfaces were 30 nm, 70 nm, and 220 nm thick. All of the following results remain consistent over any of the surface thicknesses. For this reason, we will only present our results for the 220 nm thick substrate.

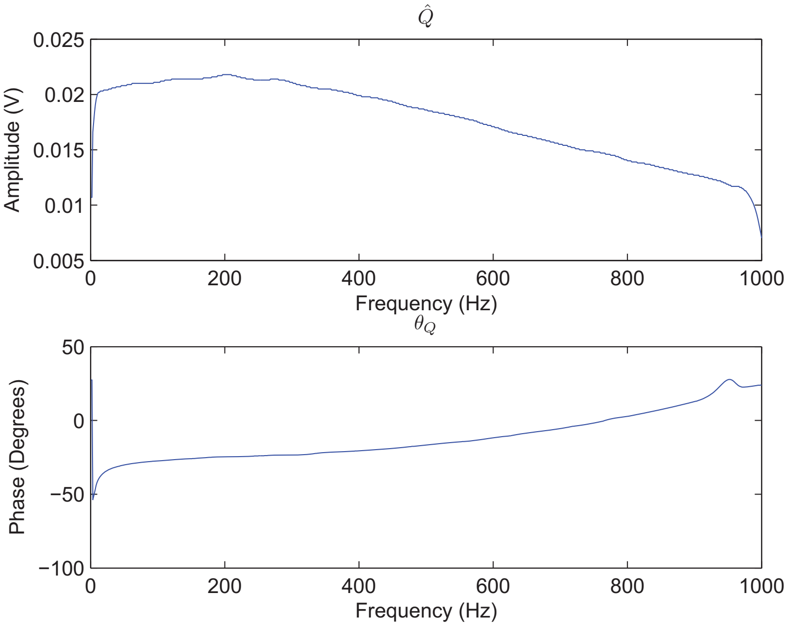

Figure 7. The top plot is the modulation frequency in Hertz versus the amplitude in Volts of the piezo drive signal. The bottom plot is the modulation frequency in Hertz versus the phase in degrees of the piezo drive signal. The experimental data was taken with a preload of 0.25 V on a 220 nm thick polystyrene surface.

The data was collected by setting the AFM tip on the surface, and applying a DC voltage. Since we are dealing with a viscoelastic surface, there is an initial creep before 'near' equilibrium is reached. During the viscoelastic creep, five to six data points are collected. A data point is a measure of amplitude in volts, or phase in degrees. After equilibrium is reached, the sinusoidal modulation voltage bias, $\hat{\gamma} = 0.05$ V, is applied at a frequency of 1000 Hz. The system is allowed to reach steady state, then another data point is collected. After which, the frequency is lowered and the process is repeated. This is done in a sweep from 1000 Hz to 1 Hz in 801 equal increments. After the last data point is recorded, a new preload is applied, and the frequency sweep is repeated. This is done for 10 to 15 preloads, which range from 0.25 V to 5.4 V.

So, we must first eliminate the first five to six data points from our data set

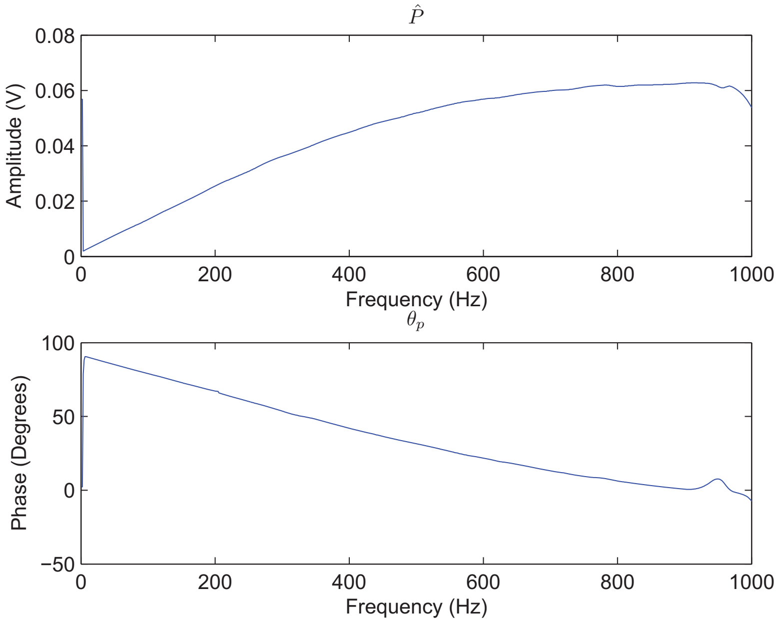

Figure 8. The top plot is the modulation frequency in Hertz versus the amplitude in Volts of the error signal. The bottom plot is the modulation frequency in Hertz versus the phase in degrees of the error signal. The experimental data was taken with a preload of 0.25 V on a 220 nm thick polystyrene surface.

because this is when the viscoelastic creep is occurring. After that, the data set is divided into individual frequency sweeps. This yields a set of data for each preload. Examples of the data for a 220 nm thick polystyrene layer with a preload of 0.25 V are given in Figures 7 and 8.

Examining the amplitude and phase of the piezo drive signal in Figure 7, we see that as the driving frequency increases, there is a slight initial increase in amplitude. This is followed by an almost linear decrease in amplitude starting from about 200 Hz. The quick drop offs at near zero frequency and at near 1000 Hz are the result of the changeover between the differing frequency data sweeps. The phase of the piezo is seen to steadily increase as the tapping frequency is increased. The small jump in phase at around 950 Hz is an as yet unexplained anomaly. Turning to the error data in Figure 8, we see that at near zero frequency, there is almost no error in

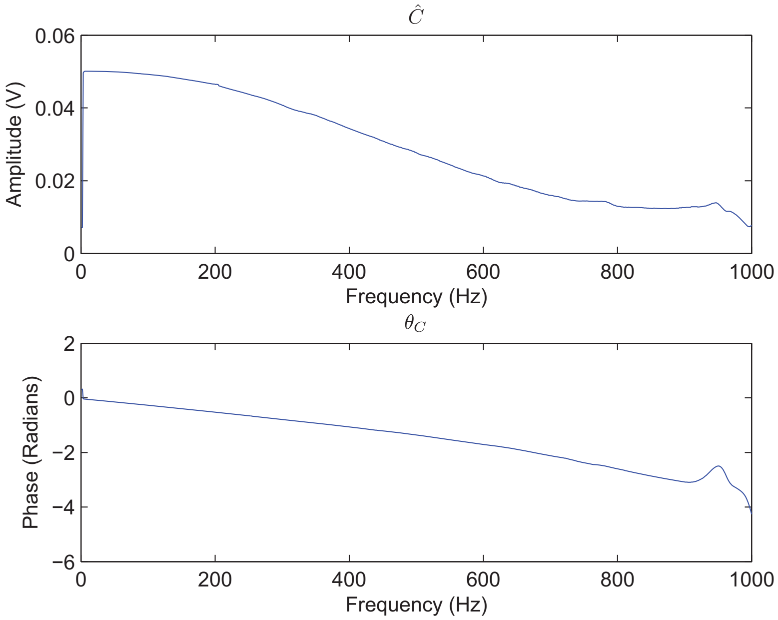

Figure 9. These plots are calculated results from our model. The top plot is the modulation frequency in Hertz versus the amplitude in Volts of the AFM tip position. The bottom plot is the modulation frequency in Hertz versus the phase in radians of the AFM tip position.

the amplitude. This means that at low frequency, the AFM has the same amplitude as the driving amplitude. As the frequency is increased, there is a steady increase in the error amplitude. The phase near zero frequency is about 90 degrees. As the driving frequency is increased, the phase steadily decreases. Again, we note the as yet unexplained anomalous jump around 950 Hz.

Now, we are going to calculate the dynamic cantilever tip position amplitude, $\hat{C}$, from Equation (194). We will also calculate the phase, θ_C, of the cantilever tip position from Equation (195). Plots of the tip position amplitude and phase are shown in Figure 9.

From Figure 9 we can see that as we approach zero frequency, the AFM tip moves at the driving amplitude and phase. Exactly as we would expect since, the material response time will be faster than the driving frequency. This means that the surface

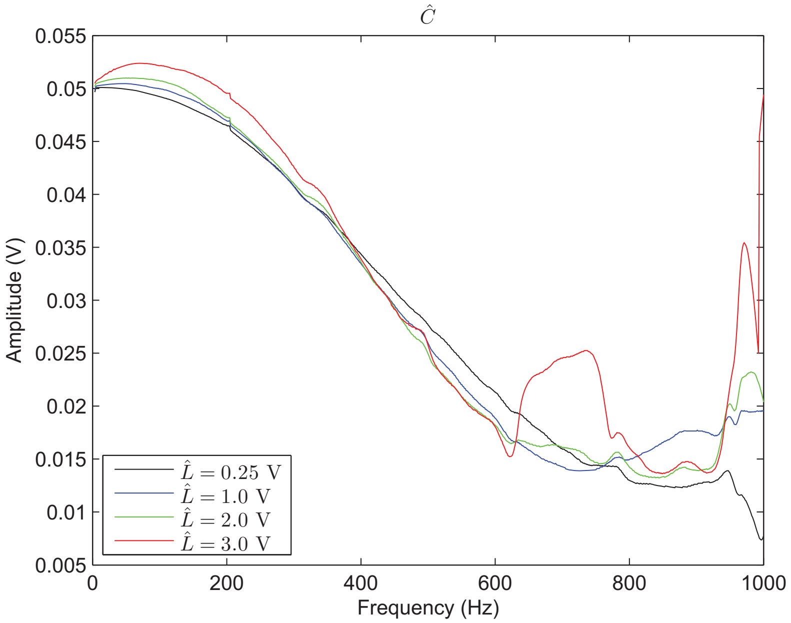

Figure 10. This plot is calculated results from our model. This plot is the modulation frequency in Hertz versus the amplitude in Volts of the AFM tip position for various preload voltages.

responds fast enough, and the cantilever moves in phase and at the same amplitude as our modulation voltage. As the frequency increases, we see the viscoelasticity of the surface lowers the amplitude of the tip movement. We also see the phase shift increases in magnitude as we increase in frequency.

We will now present more results for the calculated AFM tip position amplitude, $\hat{C}$, and its phase, θ_C, based on the data for various preloads at 220nm. The calculated AFM tip position amplitude for various preloads is shown in Figure 10. At lower frequencies, the cantilever tip position is larger when there is a higher preload. As we increase in frequency, the AFM tip position amplitude begins to decrease regardless of the preload. Also, the slope of the amplitude curve is greater for higher preloads.

Looking at the phase from the cantilever tip movement, in Figure 11, we see that at low driving frequencies the AFM tip is in phase with the surface. As the driving frequency is increased, the phase shift decreases. The larger the preload voltage, the

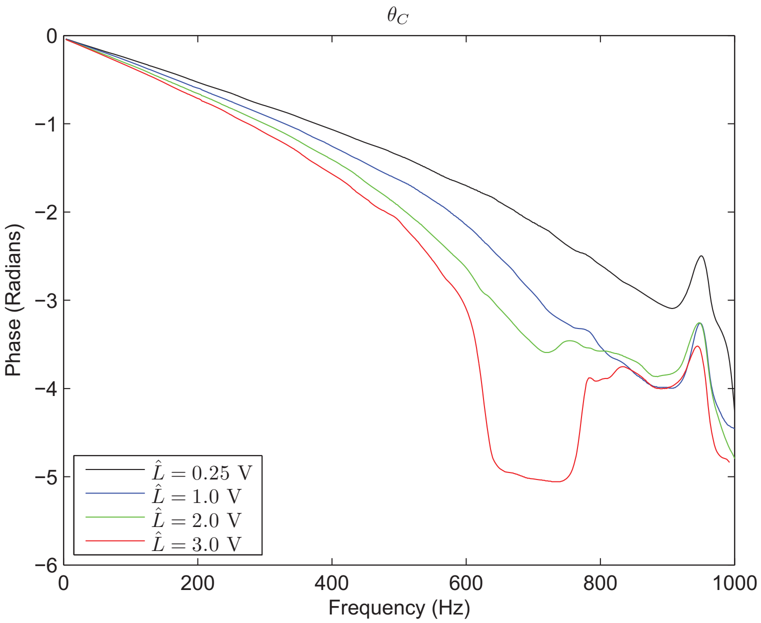

Figure 11. This plot is the modulation frequency in Hertz versus the phase in radians of the AFM tip position for various preload voltages.

greater the rate of decrease in the phase shift. At just over 600 Hz for a 3 volt preload, we see a jump in the phase and the amplitude of the tip position. This is because the tip has such a high preload and is 180 degrees out of phase with the driving voltage. We believe the tip actually left the surface, which is why there is a jump in both the amplitude and phase. Observe that the unexplained anomalous phase jump around 950 Hz presents itself in the AFM phase data as well.

Next, we examine the viscoelastic model parameters. Since the piezo delay time was not measured, we can only analyze the viscoelastic parameters from a purely mathematical standpoint. First, recall that we need to satisfy $p(0) = 1$ and $q(0) = 0$ in the viscoelastic model, Equations (221) and (222). Note from Figures 7 and 9 that both the piezo amplitude, $\hat{Q}$, and AFM amplitude, $\hat{C}$, are continuous with respect to frequency. Also, approaching zero tapping frequency $\hat{C}, \hat{Q} > 0$. Therefore, as long as $D(0) \neq 0$, then Equation (222) requires $\theta_x(0) = 0$ in order to satisfy $q(0) = 0$.

To demonstrate that $D(0) \neq 0$, suppose not. For $D^2(0) = 0$, using Equation (208) requires $\cos(\theta_x(0)) = \frac{Q^2(0)+C^2(0)}{2C(0)Q(0)}$. Thus,

$$\sin(\theta_x(0)) = \left[1 - \left(\frac{Q^2(0) + C^2(0)}{2C(0)Q(0)}\right)^2\right]^{1/2} = i\frac{Q^2(0) - C^2(0)}{2C(0)Q(0)}. \tag{225}$$

Since both $C(0)$ and $Q(0)$ are real, then Equation (225) can only be satisfied if $\theta_x(0)$ is complex. However, $\theta_x = \theta_C - \theta_Q + \tau_p^*$ is a real number. Therefore, $D^2(0) \neq 0$.

Now, using the requirements that $p(0) = 1$ and $\theta_x(0) = 0$, along with Equation (221) we obtain

$$\chi^* = \frac{C(0)}{2(Q(0) - C(0))}. \tag{226}$$

This allows us to estimate χ^* without having to know Q_{DC} as was necessary in Equation (202). The only requirement is that τ_p^* approaches $\theta_Q - \theta_C$ near zero tapping frequency. Since the viscoelastic material has a faster wave speed than the driving frequency near zero (see Figure 9 and the argument given earlier in this section), then we also have a way of estimating the piezo delay time near zero tapping frequency.

Although the preceding analysis means that the mathematical model is consistent with the experiment, without the actual measurements of the DC piezo loading, $\hat{Q}_{DC}$, and the piezo delay time, τ_p, we cannot truly give any more material properties. Since τ_p is a function of the driving frequency, then knowing an estimate of the delay time near zero frequency will not help to calculate the frequency dependent, viscoelastic material properties. In addition, the variability in how the data is collected makes it very difficult, and possibly inaccurate, to estimate χ^* based on Equation (226). That being said, an estimate was attempted using a linear fit, and for a preload of 0.25 V, $\chi^* \approx 50$. Using Equation (224) this means that $E_0^* \approx 1$ GPa, which is of the same order of magnitude as our estimate based on published values.

In summary, this chapter sets up an error model that allows us to calculate the penetration depth of the AFM tip into the material based on the experimental data. We then equated this solution to our analytical solution for the penetration depth from the last chapter. This allowed the production of an analytical solution of the viscoelastic material parameters in terms of experimental data. We then presented our calculated data and made observations based on our results. The next chapter will present our conclusions and other possible future extensions and applications of this analytical AFM model.

VI. Conclusions

Modeling the AFM dynamic nanoindentation experiment that was described in Section 1.2 provides us with a wealth of information. The model of the experimental setup was divided into two models that are coupled by boundary conditions. The two models created were an AFM model and a material model.

For the AFM model, we initially assume we can model the AFM probe as a cantilevered beam. This leads us to a one-dimensional spring-mass representation of the AFM. The forcing functions used in the spring-mass system are a static force, a sinusoidal force, and the force generated by the surface stresses over the area of the AFM tip. The surface stress forces are used to couple the AFM model to the surface. The static and sinusoidal forces are generic and in the analytical model solution they represent the piezo forcing of the system. It should be noted that AFM's and nanoindentation systems can both be modeled as spring-mass systems, and with very little modification, the analytical model produced from this research can be modified to incorporate either system. This shows the possibility of broad application of our analytical model.

The material model is based on viscoelastic material behavior. The model assumes an axisymmetric indenter which indents a semi-infinite half-space. The indentation is assumed to be a static displacement superposed with a much smaller dynamic displacement. Specific boundary conditions are chosen to represent an AFM dynamic nanoindentation experiment which, as it turns out, are the same conditions as a (non-AFM) nanoindentation experiment. The analytical solution of the material model for the penetration depth of the indenter contains a static and a dynamic piece. The static piece corresponds directly to the viscoelastic extension of Sneddon's solution [52, 84], which lends us to believe the dynamic piece is correct. Current solutions only modify the viscoelastic extension of Sneddon's solution in light of small dynamic displacements. This violates certain assumptions in the problems formulation, and is mathematically incorrect.

The coupled AFM and material models are then analytically solved for the penetration depth of the AFM tip into a viscoelastic surface. The viscoelastic model is assumed to be represented by a polynomial in frequency, and can be chosen after the experimental data is analyzed. Current solutions assume a viscoelastic model beforehand, and are then pigeonholed by the formulation of the model. It should be noted that the solution for the penetration depth is under the assumption of forcing at low frequencies. The solution can easily be modified to incorporate forcing at higher frequencies.

A third model we called the error model was then created to relate the raw experimental data to the penetration depth of the AFM tip. The analytical solution for the penetration depth of the coupled AFM and material model was then equated to the error model solution. This allowed us to produce a simple analytical model that relates raw experimental data to viscoelastic material parameters. The manipulated data can then be fit with a polynomial model, and the coefficients of the fit can be interpreted.

As an illustration, viscoelastic properties for a polystyrene thin film on a silicon substrate are calculated and presented using the analytical solution. Because of lack of experimental measurements, not all calculations were possible. It is our assertion that given all the necessary experimental data, our simple analytical model will provide viscoelastic properties of near-surface materials from AFM dynamic nanoindentation experiments. The novelty of our analytical model is that it admits different stress-strain materials descriptions than current models.

In addition to the extensions in applications of this model to broader experiments, as described above, the model may be extended in other ways. Possible extensions include the incorporation of adhesion to the material model, though this will likely produce integrals with only numerical solutions. Other possibilities include the calculation of the next, smaller term in the linear approximation of the material model. The next term will contain convolutions of functions and in light of the currently modeled experiment was considered negligibly small.

This research in nanoscale viscoelastic material properties allows for the advancement of study in nanomaterials and has applications in many areas. Of particular interest to the United States Air Force and the Department of Defense are, high-altitude long-endurance ISR airships, prompt theater-range ISR/strike systems, direct forward air delivery and resupply, energy-efficient partially buoyant cargo airlifters, fuel-efficient hybrid wing-body aircraft, and hyperprecision low-collateral damage munitions [17]. This research will help further all fields that are associated with nanomechanical properties.

Appendix A. Cylindrical Coordinates

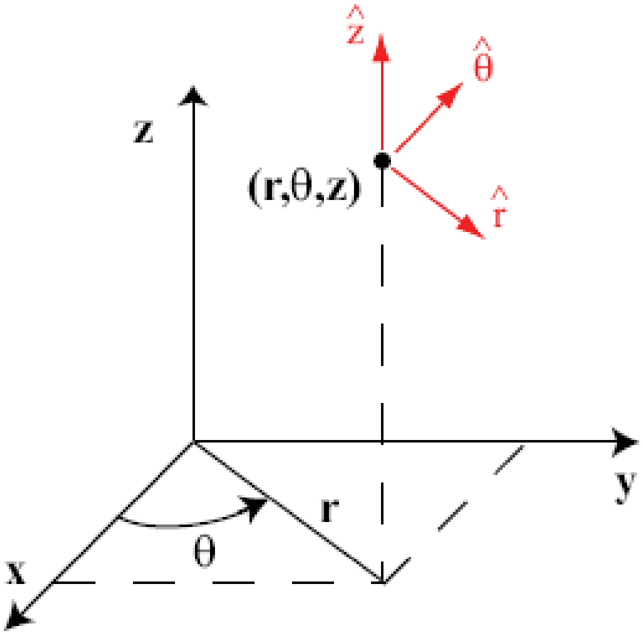

Figure 12. The cylindrical coordinate system.

The cylindrical coordinate system is a generalization of polar coordinates to three dimensions. The representation of a point in cylindrical coordinates is (r, θ, z), as can be seen in Figure 12. Simple formulas exist to convert from the rectangular coordinates (x, y, z) to the cylindrical coordinates (r, θ, z). These formulas are

$$r = \sqrt{x^2 + y^2}, \tag{227}$$

$$\theta = \arctan\left(\frac{y}{x}\right), \tag{228}$$

and

$$z = z, \tag{229}$$

where $r \in [0, \infty)$, $\theta \in [0, 2\pi)$, and $z \in (-\infty, \infty)$. The inverse tangent function must be defined in order to take the correct quadrant of (x, y) into account.

In order to convert from the cylindrical coordinates (r, θ, z) to the rectangular coordinates (x, y, z), we use the formulas

$$x = r\cos(\theta), \tag{230}$$

$$y = r\sin(\theta), \tag{231}$$

and

$$z = z. \tag{232}$$

The unit vectors in cylindrical coordinates are $\hat{r}$, $\hat{\theta}$, and $\hat{z}$. They define the directions of the coordinate terms, and can be seen in Figure 12. We define the gradient as

$$\nabla = \hat{r}\frac{\partial}{\partial r} + \hat{\theta}\frac{1}{r}\frac{\partial}{\partial \theta} + \hat{z}\frac{\partial}{\partial z}. \tag{233}$$

The divergence is defined as

$$\nabla \cdot \vec{u} = \frac{1}{r}\frac{\partial}{\partial r}(ru_r) + \frac{1}{r}\frac{\partial u_\theta}{\partial \theta} + \frac{\partial u_z}{\partial z}. \tag{234}$$

The curl is defined by

$$\nabla \times \vec{u} = \left(\frac{1}{r}\frac{\partial u_z}{\partial \theta} - \frac{\partial u_\theta}{\partial z}\right)\hat{r} + \left(\frac{\partial u_r}{\partial z} - \frac{\partial u_z}{\partial r}\right)\hat{\theta} + \frac{1}{r}\left(\frac{\partial}{\partial r}(ru_\theta) - \frac{\partial u_r}{\partial \theta}\right)\hat{z}. \tag{235}$$

Appendix B. Dual Integral Equations

This appendix shows a brief overview, without derivation, of the results of Mandal [60]. For a complete derivation, please refer to that paper.

The general form of dual integral equations involving Bessel functions of the first kind is

$$\begin{aligned} \int_0^\infty \beta^{-2\alpha^*} J_\nu(\rho\beta)\left[1+w(\beta)\right]\Phi(\beta)d\beta &= f(\rho), && 0<\rho<1, \\ \int_0^\infty \beta^{-2\beta^*} J_\mu(\rho\beta)\Phi(\beta)d\beta &= g(\rho), && \rho>1, \end{aligned} \tag{236}$$

where α^* and β^* are known constants, ν and μ are the known orders of the Bessel functions, $w(\beta)$ is an arbitrary weight function, $f(\rho)$ and $g(\rho)$ are known functions valid over their particular region, and $\Phi(\beta)$ is the unknown function to be determined.

Through the use of Sonine's integrals and Hankel inversion, Mandal reduced Equation (236) to a Fredholm integral equation of the second kind. This equation in $\Phi(\rho)$ is

$$\begin{aligned} \Phi(\rho) = \rho^{\gamma-s+1}\Bigg[&\int_0^1 rF_1(r)J_{\lambda+s}(r\rho)dr + \int_1^\infty rG_1(r)J_{\lambda+s}(r\rho)dr \\ &- \int_0^\infty u^{-\gamma+s}w(u)\Phi(u)\frac{uJ_{\lambda+s+1}(u)J_{\lambda+s}(\rho)-\rho J_{\lambda+s+1}(\rho)J_{\lambda+s}(u)}{u^2-\rho^2}du\Bigg], \end{aligned} \tag{237}$$

where λ and γ are defined by

$$\lambda = \frac{\mu+\nu}{2}+\beta^*-\alpha^*, \tag{238a}$$

$$\gamma = \frac{\mu-\nu}{2}+\beta^*+\alpha^*, \tag{238b}$$

and s is a nonnegative integer we choose so that $\lambda+s>-1$. $F_1(r)$ and $G_1(r)$ are functions that are defined by

$$F_1(r) = (-1)^s r^{\lambda+s} \left(\frac{1}{r}\frac{d}{dr}\right)^s \left[r^{-\lambda} F(r)\right], \tag{239a}$$

$$G_1(r) = (-1)^s r^{\lambda+s} \left(\frac{1}{r}\frac{d}{dr}\right)^s \left[r^{-\lambda} G(r)\right]. \tag{239b}$$

Here, the functions $F(r)$ and $G(r)$ are defined as

$$F(r) = \frac{2^{-\xi}}{\Gamma(\xi+1)} r^{-\xi-\nu-1+\ell} \left(\frac{1}{r}\frac{d}{dr}\right)^\ell \int_0^r \rho^{\nu+1} \left(r^2 - \rho^2\right)^\xi f(\rho) d\rho, \tag{240a}$$

$$G(r) = \frac{(-1)^m 2^{-\eta}}{\Gamma(\eta+1)} r^{\mu-\eta-1+m} \left(\frac{1}{r}\frac{d}{dr}\right)^m \int_r^\infty \rho^{-\mu+1} \left(\rho^2 - r^2\right)^\eta g(\rho) d\rho, \tag{240b}$$

where $\Gamma(z)$ is the Gamma function and

$$\xi = \frac{\mu-\nu}{2} + \beta^* - \alpha^* - 1 + \ell, \tag{241a}$$

$$\eta = \frac{\mu-\nu}{2} + \alpha^* - \beta^* - 1 + m. \tag{241b}$$

The terms ℓ and m are nonnegative integers that we choose so that $\xi > -1$ and $\eta > -1$. The requirements that certain terms are greater than -1 are because of the Hankel inversions used to solve Equation (236).

Appendix C. Integral Equation Neumann Series [41]

An integral equation Neumann Series is used to solve Fredholm integral equations of the second kind. A Fredholm integral equation of the second kind takes the form

$$\phi(x) = f(x) + \lambda \int_a^b K(x,t)\phi(t)dt, \tag{242}$$

where $a, b \in \mathbb{R}$ and $\lambda \in \mathbb{R} - \{0\}$. Define the operator K by

$$K\phi(x) = \int_a^b K(x,t)\phi(t)dt. \tag{243}$$

Therefore, we can write Equation (242) as

$$T\phi = \phi, \tag{244}$$

where

$$T\phi = f + \lambda K\phi. \tag{245}$$

If f is in a Hilbert space H, and K is a bounded linear operator with the property

$$\|K\phi_1 - K\phi_2\| \leq M\|\phi_1 - \phi_2\|, \tag{246}$$

then Equation (244) has a unique solution for all f provided that $|\lambda|M < 1$. In addition, if f is in $L_2[a,b]$, then

$$\phi(x) = \lim_{n\to\infty} T^n f_0(x), \tag{247}$$

where $f_0(x) \in L_2[a,b]$ is an arbitrary initial function. So,

$$Tf_0 = f + \lambda K f_0, \tag{248}$$

$$T^2 f_0 = T\left[f + \lambda K f_0\right] = f + \lambda K f + \lambda^2 K^2 f_0, \tag{249}$$

and

$$T^n f_0 = f + \lambda K f + \lambda^2 K^2 f + \cdots + \lambda^{n-1} K^{n-1} f + \lambda^n K^n f_0. \tag{250}$$

Therefore,

$$\phi = f + \lambda K f + \lambda^2 K^2 f + \cdots + \lambda^n K^n f + \cdots . \tag{251}$$

We define the integral operator K^n as

$$K^n f(x) = \int_a^b K_n(x, y) f(y) dy, \tag{252}$$

where $K_n(x, y)$ is defined recursively by

$$K_n(x, y) = \int_a^b K(x, z) K_{n-1}(z, y) dz, \qquad n = 2, 3, \ldots, \tag{253}$$

and

$$K_1(x, y) = K(x, y). \tag{254}$$

Appendix D. Some Integrals

This appendix includes some important integrals and their derivations.

$$\int_0^\infty \left[j_0(u+\beta)+j_0(u-\beta)\right] j_0(u)du = \pi j_0(\beta). \tag{255}$$

$$\int_0^\infty \left[j_0(u+\beta)+j_0(u-\beta)\right] j_2(u)du = \pi j_2(\beta). \tag{256}$$

$$\int_0^\infty \beta J_0(\beta\rho) j_0(\beta) d\beta = \begin{cases} \left(1-\rho^2\right)^{-\frac{1}{2}}, & 0<\rho<1, \\ 0, & 1<\rho. \end{cases} \tag{257}$$

$$\int_0^\infty \beta J_0(\beta\rho) j_2(\beta) d\beta = \begin{cases} \left(1-\rho^2\right)^{-\frac{1}{2}}\left(2-3\rho^2\right), & 0<\rho<1, \\ 0, & 1<\rho. \end{cases} \tag{258}$$

$$\int_0^\infty J_1(\beta) j_0(\beta) d\beta = 1. \tag{259}$$

$$\int_0^\infty J_1(\beta) j_2(\beta) d\beta = 0. \tag{260}$$

The derivation for Equation (255) is as follows

$$\begin{aligned}
&\int_0^\infty \left[j_0(u+\beta)+j_0(u-\beta)\right] j_0(u)du \\
&\quad = \int_0^\infty \left[\frac{\sin(u+\beta)}{u+\beta}+\frac{\sin(u-\beta)}{u-\beta}\right]\frac{\sin(u)}{u}du \\
&\quad = \int_0^\infty \left[\frac{\sin(u)\cos(\beta)+\sin(\beta)\cos(u)}{u+\beta}+\frac{\sin(u)\cos(\beta)-\sin(\beta)\cos(u)}{u-\beta}\right]\frac{\sin(u)}{u}du \\
&\quad = 2\int_0^\infty \left[\frac{u\sin(u)\cos(\beta)-\beta\sin(\beta)\cos(u)}{u^2-\beta^2}\right]\frac{\sin(u)}{u}du \\
&\quad = 2\cos(\beta)\int_0^\infty \frac{\sin^2(u)}{u^2-\beta^2}du - 2\beta\sin(\beta)\int_0^\infty \frac{\sin(u)\cos(u)}{u(u^2-\beta^2)}du \\
&\quad = 2\cos(\beta)\int_0^\infty \frac{\sin^2(u)}{u^2-\beta^2}du - \beta\sin(\beta)\int_0^\infty \frac{\sin(2u)}{u(u^2-\beta^2)}du
\end{aligned} \tag{261}$$

Now, from Gradshteyn and Ryzhik [27] page 432 we have

$$\int_0^\infty \frac{\sin^2(u)}{u^2-\beta^2}du = \frac{\pi}{4\beta}\sin(2\beta) = \frac{\pi}{2\beta}\sin(\beta)\cos(\beta), \tag{262}$$

and from page 425 we have

$$\int_0^\infty \frac{\sin(2u)}{u(u^2-\beta^2)}du = \frac{-\pi}{2\beta^2}\left[1-\cos(2\beta)\right] = \frac{-\pi}{\beta^2}\sin^2(\beta). \tag{263}$$

So,

$$\begin{aligned}\int_0^\infty & \left[j_0(u+\beta)+j_0(u-\beta)\right]j_0(u)du \\ &= \frac{\pi}{\beta}\sin(\beta)\cos^2(\beta) + \frac{\pi}{\beta}\sin^3(\beta) \\ &= \frac{\pi}{\beta}\sin(\beta)\left[\cos^2(\beta)+\sin^2(\beta)\right] = \pi\frac{\sin(\beta)}{\beta} = \pi j_0(\beta).\end{aligned} \tag{264}$$

The derivation for Equation (256) is as follows

$$\begin{aligned}\int_0^\infty & \left[j_0(u+\beta)+j_0(u-\beta)\right]j_2(u)du \\ &= 2\int_0^\infty \left[\frac{u\sin(u)\cos(\beta)-\beta\sin(\beta)\cos(u)}{u^2-\beta^2}\right]\left[3\frac{\sin(u)}{u^3}-3\frac{\cos(u)}{u^2}-\frac{\sin(u)}{u}\right]du \\ &= 6\cos(\beta)\left[\int_0^\infty \frac{\sin^2(u)}{u^2\left(u^2-\beta^2\right)}du - \int_0^\infty \frac{\sin(u)\cos(u)}{u\left(u^2-\beta^2\right)}du\right] \\ &\quad + 6\beta\sin(\beta)\left[\int_0^\infty \frac{-\sin(u)\cos(u)}{u^3\left(u^2-\beta^2\right)}du + \int_0^\infty \frac{\cos^2(u)}{u^2\left(u^2-\beta^2\right)}du\right] - \pi j_0(\beta).\end{aligned} \tag{265}$$

Now, using partial fraction decomposition, we may write

$$\int_0^\infty \frac{\sin^2(u)}{u^2\left(u^2-\beta^2\right)}du = \int_0^\infty \frac{-\sin^2(u)}{\beta^2 u^2}du + \int_0^\infty \frac{\sin^2(u)}{\beta^2\left(u^2-\beta^2\right)}du. \tag{266}$$

From Gradshteyn and Ryzhik [27] page 431 we have

$$\int_0^\infty \frac{-\sin^2(u)}{\beta^2 u^2} du = \frac{-\pi}{2\beta^2}, \tag{267}$$

and from page 432 we have

$$\int_0^\infty \frac{\sin^2(u)}{\beta^2 \left(u^2 - \beta^2\right)} du = \frac{\pi}{4\beta^3} \sin(2\beta). \tag{268}$$

Now, we may write

$$-\int_0^\infty \frac{\sin(u)\cos(u)}{u\left(u^2 - \beta^2\right)} du = \int_0^\infty \frac{\sin(2u)}{2u\left(\beta^2 - u^2\right)} du = \frac{\pi}{4\beta^2}\left(1 - \cos(2\beta)\right), \tag{269}$$

where we have used Gradshteyn and Ryzhik [27] page 425. So,

$$\begin{aligned} &\int_0^\infty \frac{\sin^2(u)}{u^2\left(u^2 - \beta^2\right)} du - \int_0^\infty \frac{\sin(u)\cos(u)}{u\left(u^2 - \beta^2\right)} du \\ &\qquad = -\frac{\pi}{4\beta^2}\left[1 + \cos(2\beta)\right] + \frac{\pi}{4\beta^3}\sin(2\beta) \\ &\qquad = -\frac{\pi}{2\beta^2}\left[\cos^2(\beta)\right] + \frac{\pi}{2\beta^3}\sin(\beta)\cos(\beta). \end{aligned} \tag{270}$$

Now, by partial fraction decomposition we have

$$\begin{aligned} &\int_0^\infty \frac{-\sin(u)\cos(u)}{u^3\left(u^2 - \beta^2\right)} du \\ &\quad = \int_0^\infty \frac{\sin(u)\cos(u)}{\beta^2 u^3} du + \int_0^\infty \frac{\sin(u)\cos(u)}{\beta^4 u} du - \int_0^\infty \frac{u\sin(u)\cos(u)}{\beta^4\left(u^2 - \beta^2\right)} du. \end{aligned} \tag{271}$$

Now, from Gradshteyn and Ryzhik [27] page 431 we have

$$\int_0^\infty \frac{\sin(u)\cos(u)}{\beta^4 u} du = \frac{\pi}{4\beta^4}, \tag{272}$$

and from page 424 we have

$$-\int_0^\infty \frac{u\sin(u)\cos(u)}{\beta^4\left(u^2-\beta^2\right)}du = \int_0^\infty \frac{u\sin(2u)}{2\beta^4\left(\beta^2-u^2\right)}du = -\frac{\pi}{4\beta^4}\cos(2\beta). \tag{273}$$

Thus,

$$\begin{aligned}\int_0^\infty \frac{-\sin(u)\cos(u)}{u^3\left(u^2-\beta^2\right)}du &= \int_0^\infty \frac{\sin(u)\cos(u)}{\beta^2u^3}du + \frac{\pi}{4\beta^4}\left(1-\cos(2\beta)\right)\\ &= \int_0^\infty \frac{\sin(2u)}{2\beta^2u^3}du + \frac{\pi}{2\beta^4}\sin^2(\beta).\end{aligned} \tag{274}$$

Now, we may write

$$\int_0^\infty \frac{\cos^2(u)}{u^2\left(u^2-\beta^2\right)}du = -\int_0^\infty \frac{\cos^2(u)}{\beta^2u^2}du + \int_0^\infty \frac{\cos^2(u)}{\beta^2\left(u^2-\beta^2\right)}du. \tag{275}$$

From Gradshteyn and Ryzhik [27] page 461 we have

$$\int_0^\infty \frac{\cos^2(u)}{\beta^2\left(u^2-\beta^2\right)}du = -\frac{\pi}{4\beta^3}\sin(2\beta) = -\frac{\pi}{2\beta^3}\sin(\beta)\cos(\beta). \tag{276}$$

Thus,

$$\int_0^\infty \frac{\cos^2(u)}{u^2\left(u^2-\beta^2\right)}du = -\int_0^\infty \frac{1+\cos(2u)}{2\beta^2u^2}du - \frac{\pi}{2\beta^3}\sin(\beta)\cos(\beta). \tag{277}$$

Therefore,

$$\begin{aligned}&\int_0^\infty \frac{-\sin(u)\cos(u)}{u^3\left(u^2-\beta^2\right)}du + \int_0^\infty \frac{\cos^2(u)}{u^2\left(u^2-\beta^2\right)}du\\ &\qquad= \frac{1}{2\beta^2}\int_0^\infty \frac{\sin(2u)-u-u\cos(2u)}{u^3}du - \frac{\pi}{2\beta^3}\sin(\beta)\cos(\beta) + \frac{\pi}{2\beta^4}\sin^2(\beta).\end{aligned} \tag{278}$$

Now, we may write

$$\begin{aligned}\frac{1}{2\beta^2}&\int_0^\infty \frac{\sin(2u)-u-u\cos(2u)}{u^3}du\\&=\frac{1}{2\beta^2}\left[\int_0^\infty \frac{\sin(2u)-2u\cos(2u)}{u^3}du+\int_0^\infty \frac{u\cos(2u)-u}{u^3}du\right]\\&=\frac{1}{2\beta^2}\left[\int_0^\infty \frac{\sin(2u)-2u\cos(2u)}{u^3}du-2\int_0^\infty \frac{\sin^2(u)}{u^2}du\right].\end{aligned} \tag{279}$$

From Gradshteyn and Ryzhik [27] page 447 we have

$$\int_0^\infty \frac{\sin(2u)-2u\cos(2u)}{u^3}du=\pi, \tag{280}$$

and from page 431 we have

$$-2\int_0^\infty \frac{\sin^2(u)}{u^2}du=-\pi. \tag{281}$$

Therefore,

$$\frac{1}{2\beta^2}\int_0^\infty \frac{\sin(2u)-u-u\cos(2u)}{u^3}du=0. \tag{282}$$

Hence,

$$\int_0^\infty \frac{-\sin(u)\cos(u)}{u^3\left(u^2-\beta^2\right)}du+\int_0^\infty \frac{\cos^2(u)}{u^2\left(u^2-\beta^2\right)}du=-\frac{\pi}{2\beta^3}\sin(\beta)\cos(\beta)+\frac{\pi}{2\beta^4}\sin^2(\beta). \tag{283}$$

Now, combining Equations (265), (270), and (283) we get

$$\begin{aligned}
&\int_0^\infty \left[j_0(u+\beta)+j_0(u-\beta)\right] j_2(u)du \\
&\qquad = 6\cos(\beta)\left[-\frac{\pi}{2\beta^2}\left[\cos^2(\beta)\right]+\frac{\pi}{2\beta^3}\sin(\beta)\cos(\beta)\right] \\
&\qquad\quad + 6\beta\sin(\beta)\left[-\frac{\pi}{2\beta^3}\sin(\beta)\cos(\beta)+\frac{\pi}{2\beta^4}\sin^2(\beta)\right]-\pi j_0(\beta) \\
&\qquad = \pi\left[3\frac{\sin(\beta)}{\beta^3}\left(\cos^2(\beta)+\sin^2(\beta)\right)-3\frac{\cos(\beta)}{\beta^2}\left(\cos^2(\beta)+\sin^2(\beta)\right)-\frac{\sin(\beta)}{\beta}\right] \\
&\qquad = \pi\left[3\frac{\sin(\beta)}{\beta^3}-3\frac{\cos(\beta)}{\beta^2}-\frac{\sin(\beta)}{\beta}\right]=\pi j_2(\beta).
\end{aligned} \tag{284}$$

The derivation for Equation (257) is as follows

$$\begin{aligned}
\int_0^\infty \beta J_0(\beta\rho)j_0(\beta)d\beta &= \int_0^\infty \beta J_0(\beta\rho)\frac{\sin(\beta)}{\beta}d\beta \\
&= \int_0^\infty J_0(\beta\rho)\sin(\beta)d\beta.
\end{aligned} \tag{285}$$

Now, from Gradshteyn and Ryzhik [27] page 718 we have

$$\int_0^\infty J_0(\beta\rho)\sin(\beta)d\beta = \begin{cases} \left(1-\rho^2\right)^{-\frac{1}{2}}, & 0<\rho<1, \\ 0, & 1<\rho. \end{cases} \tag{286}$$

Thus,

$$\int_0^\infty \beta J_0(\beta\rho)j_0(\beta)d\beta = \begin{cases} \left(1-\rho^2\right)^{-\frac{1}{2}}, & 0<\rho<1, \\ 0, & 1<\rho. \end{cases} \tag{287}$$

The derivation for Equation (258) is as follows

$$\int_0^\infty \beta J_0(\beta\rho)j_2(\beta)d\beta = \int_0^\infty \beta J_0(\beta\rho)\left[\frac{3}{\beta}j_1(\beta)-j_0(\beta)\right]d\beta, \tag{288}$$

where we have used the recurrence relationship from Abramowitz and Stegun [1] of

$$j_{n-1}(z) + j_{n+1}(z) = (2n+1)z^{-1}j_n(z), \tag{289}$$

with $n = 1$. Now, using the fact that $j_n(x) = \sqrt{\frac{\pi}{2x}}J_{n+1/2}(x)$, we can write Equation (288) as

$$\int_0^\infty \beta J_0(\beta\rho)j_2(\beta)d\beta = 3\sqrt{\frac{\pi}{2}}\int_0^\infty \beta^{-1/2}J_0(\beta\rho)J_{3/2}(\beta)d\beta - \int_0^\infty \beta J_0(\beta\rho)j_0(\beta)d\beta. \tag{290}$$

From Gradshteyn and Ryzhik [27] page 683 we have

$$\int_0^\infty \beta^{-1/2}J_0(\beta\rho)J_{3/2}(\beta)d\beta = \begin{cases} \sqrt{\frac{2}{\pi}}\left(1-\rho^2\right)^{\frac{1}{2}}, & 0<\rho<1, \\ 0, & 1<\rho. \end{cases} \tag{291}$$

Finally, combining Equations (257) and (290)-(291) yields

$$\int_0^\infty \beta J_0(\beta\rho)j_2(\beta)d\beta = \begin{cases} \left(2-3\rho^2\right)\left(1-\rho^2\right)^{-\frac{1}{2}}, & 0<\rho<1, \\ 0, & 1<\rho. \end{cases} \tag{292}$$

The derivation of Equation (259) is as follows

$$\int_0^\infty J_1(\beta)j_0(\beta)d\beta = \int_0^\infty J_1(\beta)\frac{\sin(\beta)}{\beta}d\beta. \tag{293}$$

Now, from Gradshteyn and Ryzhik [27] page 727 we have

$$\int_0^\infty J_1(\beta)\frac{\sin(\beta)}{\beta}d\beta = 1. \tag{294}$$

So,

$$\int_0^\infty J_1(\beta)j_0(\beta)d\beta = 1. \tag{295}$$

The derivation of Equation (260) is as follows

$$\int_0^\infty J_1(\beta) j_2(\beta) d\beta = \sqrt{\frac{\pi}{2}} \int_0^\infty \beta^{-1/2} J_1(\beta) J_{5/2}(\beta) d\beta, \tag{296}$$

where we have used the fact that $j_n(x) = \sqrt{\frac{\pi}{2x}} J_{n+1/2}(x)$. Now, from Gradshteyn and Ryzhik [27] page 683 we have

$$\int_0^\infty \beta^{-1/2} J_1(\beta) J_{5/2}(\beta) d\beta = 0. \tag{297}$$

Thus,

$$\int_0^\infty J_1(\beta) j_2(\beta) d\beta = 0. \tag{298}$$

Bibliography

[1] Abramowitz, Milton and Irene A. Stegun (editors). *Handbook of Mathematical Functions with Formulas, Graphs, and Mathematical Tables*. Dover Publications, New York, 1972.

[2] Andrews, L.C., B.K. Shivamoggi, and Society of Photo-optical Instrumentation Engineers. *Integral transforms for engineers*. SPIE Optical Engineering Press, 1999.

[3] Asif, S.A., K.J. Wahl, and R.J. Colton. "Nanoindentation and contact stiffness measurement using force modulation with a capacitive load-displacement transducer". *Review of Scientific Instruments*, 70(5):2408–2413, May 1999.

[4] Atkins, Peter and Julio de Paula. *Physical Chemistry for the Life Sciences*. W.H. Freeman Company, New York, NY, 2006.

[5] Attard, Phil. "Measurement and interpretation of elastic and viscoelastic properties with the atomic force microscope". *Journal of Physics: Condensed Matter*, 19:1–33, 2007.

[6] Bagley, R.L. and P.J. Torvik. "Fractional Calculus - A Different Approach to the Analysis of Viscoelastically Damped Structures". *AIAA Journal*, 21(5):741–748, May 1983.

[7] Barthel, E. and G. Haiat. "Approximate Model for the Adhesive Contact of Viscoelastic Spheres". *Langmuir*, 18(24):9362–9370, 2002.

[8] Bhushan, Bharat (editor). *Handbook of Micro/Nano Tribology*. CRC Press LLC, Boca Raton, Florida, second edition, 1999.

[9] Binnig, G., C. F. Quate, and Ch. Gerber. "Atomic Force Microscope". *Physical Review Letters*, 56(9):930–933, March 1986.

[10] Bischel, M.S., M.R. Vanlandingham, R.F. Eduljee, J.W. Gillespie Jr., and J.M. Schultz. "On the use of nanoscale indentation with the AFM in the identification of phases in blends of linear low density polyethylene and high density polyethylene". *Journal of Material Science*, 35:221–228, 2000.

[11] Bleistein, Norman and Richard A. Handelsman. *Asymptotic Expansions of Integrals*. Dover Publications, Inc., New York, 1986.

[12] Bowman, F. *Introduction to Bessel Functions*. Longmans, Green and Co. Ltd., London, 1938.

[13] Briscoe, B. J., L. Fiori, and E. Pelillo. "Nano-indentation of Polymeric Surfaces". *Journal of Physics D: Applied Physics*, 31:2395–2405, 1998.

[14] Calvit, Harry H. "Numerical solution of the problem of impact of a rigid sphere onto a linear viscoelastic half-space and comparison with experiment". *International Journal of Solids and Structures*, 3:951–966, 1967.

[15] Cheng, L., X. Xia, L.E. Scriven, and W.W. Gerberich. "Spherical-tip indentation of viscoelastic material". *Mechanics of Materials*, 37:213–226, 2005.

[16] Christensen, R. M. *Theory of Viscoelasticity: An Introduction*. Academic Press, Inc., New York, 1971.

[17] Dahm, Werner J. A. *Technology Horizons - A Vision for Air Force Science and Technology During 2010-2030*. Technical Report AF/ST-TR-10-01-PR, United States Air Force Chief Scientist, May 2010.

[18] Derjaguin, B. V., V. M. Muller, and Yu. P. Toporov. "Effect of contact deformations on the adhesion of particles". *Journal of Colloid and Interface Science*, 53(2):314–326, November 1975.

[19] Dimitriadis, E.K., F. Horkay, J. Maresca, B. Kachar, and R.S. Chadwick. "Determination of Elastic Moduli of Thin Layers of Soft Material Using the Atomic Force Microscope". *Biophysical Journal*, 82(5):2798–2810, May 2002.

[20] Dinelli, F., S.K. Biswas, G.A.D. Briggs, and O.V. Kolosov. "Measurements of stiff-material compliance on the nanoscale using ultrasonic force microscopy". *Physical Review B*, 61(20):13995–14006, May 2000.

[21] Domke, J. and M. Radmacher. "Measuring the Elastic Properties of Thin Polymer Films with the Atomic Force Microscope". *Langmuir*, 14(12):3320–3325, March 1998.

[22] Erdélyi, Arthur. *Asymptotic Expansions*. Dover Publications, Inc., 1956.

[23] Fakhraai, Z. and J.A. Forrest. "Measuring the Surface Dynamics of Glassy Polymers". *Science*, 319:600–604, February 2008.

[24] Findley, William N., James S. Lai, and Kasif Onaran. *Creep and Relaxation of Nonlinear Viscoelastic Materials: With an Introduction to Linear Viscoelasticity*. Dover Publications, Inc., 1989.

[25] Fung, Rong-Fong and Shih-Chien Huang. "Dynamic Modeling and Vibration Analysis of the Atomic Force Microscope". *Journal of Vibration and Acoustics*, 123:502–509, October 2001.

[26] Fung, Y. C. *Foundations of Solid Mechanics*. Prentice-Hall, Inc., Englewood Cliffs, New Jersey, 1965.

[27] Gradshteyn, I.S. and I.M. Ryzhik. *Table of Integrals, Series, and Products*. Academic Press, San Diego, California, seventh edition, 2007.

[28] Graham, G.A.C. “The contact problem in the linear theory of viscoelasticity”. *International Journal of Engineering Science*, 3:27–46, 1965.

[29] Graham, G.A.C. “The contact problem in the linear theory of viscoelasticity when the time dependent contact area has any number of maxima and minima”. *International Journal of Engineering Science*, 5:495–514, 1967.

[30] Graham, G.A.C. “The correspondence principle of linear viscoelasticity theory for mixed boundary value problems involving time-dependent boundary regions”. *Quarterly of Applied Mathematics*, 26(2):167–174, 1968.

[31] Greenwood, J.A. “Contact between an axisymmetric indenter and a viscoelastic half-space”. *International Journal of Mechanical Sciences*, 52(6):829–835, June 2010.

[32] Greenwood, J.A. and K.L. Johnson. “An alternative to the Maugis model of adhesion between elastic spheres”. *Journal of Physics D: Applied Physics*, 31:3279–3290, 1998.

[33] Greenwood, J.A. and K.L. Johnson. “Oscillatory loading of a viscoelastic adhesive contact”. *Journal of Colloid and Interface Science*, 296:284–291, 2006.

[34] Grierson, D.S., E.E. Flater, and R.W. Carpick. “Accounting for the JKRDMT transition in adhesion and friction measurements with atomic force microscopy”. *Journal of Adhesion Science and Technology*, 19(3-5):291–311, 2005.

[35] Gurtin, M.E. and Eli Sternberg. “On the Linear Theory of Viscoelasticity”. *Archive for Rational Mechanics and Analysis*, 11:291–356, 1962.

[36] Guzina, B.B. and R.Y.S. Pak. "Vertical vibration of a circular footing on a linear-wave-velocity half-space". *Géotechnique*, 48(2):159–168, 1998.

[37] Haiat, G., M.C. Phan Huy, and E. Barthel. "The adhesive contact of viscoelastic spheres". *Journal of the Mechanics and Physics of Solids*, 51:69–99, 2003.

[38] Hashin, Zvi. "Vibration analysis of viscoelastic bodies with small loss tangents". *International Journal of Solids and Structures*, 13:549–559, 1977.

[39] Hertz, Heinrich. *Miscellaneous Papers*. Macmillan and Co., Inc., New York, 1896.

[40] Heuberger, M., G. Dietler, and L. Schlapbach. "Mapping the local Young's modulus by analysis of the elastic deformations occurring in atomic force microscopy". *Nanotechnology*, 6:12–23, 1995.

[41] Hochstadt, Harry. *Integral Equations*. John Wiley and Sons, Inc., New York, 1989.

[42] Howison, Sam. *Practical Applied Mathematics: Modelling, Analysis, Approximation*. Cambridge University Press, 2005.

[43] Hues, Steven M., Charles F. Draper, Kenneth P. Lee, and Richard J. Colton. "Effect of PZT and PMN actuator hysteresis and creep on nanoindentation measurements using force microscopy". *Review of Scientific Instruments*, 65(5):1561–1565, May 1994.

[44] Hunter, S.C. "The Hertz problem for a rigid spherical indenter and a viscoelastic half-space". *Journal of the Mechanics and Physics of Solids*, 8:219–234, 1960.

[45] Hurley, D.C., K. Shen, N.M. Jennett, and J.A. Turner. "Atomic force acoustic microscopy methods to determine thin-film elastic properties". *Journal of Applied Physics*, 94(4):2347–2354, August 2003.

[46] Israelachvili, Jacob N. *Intermolecular and Surface Forces.* Academic Press Inc., San Diego, California, second edition, 1991.

[47] Jang, Joonkyung, Mino Yang, and George Schatz. "Microscopic origin of the humidity dependence of the adhesion force in atomic force microscopy". *The Journal of Chemical Physics*, 126(17), 2007.

[48] Johnson, K.L., K. Kendall, and A.D. Roberts. "Surface energy and the contact of elastic solids". *Proceedings of the Royal Society of London. Series A: Mathematical and physical sciences*, 324:301–313, 1971.

[49] Kajiyama, Tisato, Keiji Tanaka, Isao Ohki, Shou-Ren Ge, Jeong-Sik Yoon, and Atsushi Takahara. "Imaging of Dynamic Viscoelastic Properties of a Phase-Separated Polymer Surface by Forced Oscillation Atomic Force Microscopy". *Macromolecules*, 27(26):7932–7934, 1994.

[50] Koeller, R.C. "Applications of fractional calculus to the theory of viscoelasticity". *Journal of Applied Mechanics*, 51:299–307, 1984.

[51] Lebedev, N. N. and Ia. S. Ufliand. "Axisymmetric Contact Problem for an Elastic Layer". *Journal of Applied Mathematics and Mechanics*, 22(3):320–326, 1958.

[52] Lee, E. H. and J. R. M. Radok. "The Contact Problem for Viscoelastic Bodies". *Journal of Applied Mechanics*, 438–444, September 1960.

[53] Lemoine, P. and J. McLaughlin. "Nanomechanical measurements on polymers using contact mode atomic force microscopy". *Thin Solid Films*, 339:258–264, 1999.

[54] Li, Guangming and Larry W. Burggraf. "Controlled Patterning of Polymer Films Using an AFM Tip as a Nano-hammer". *Nanotechnology*, 18(24), June 2007.

[55] Little, R. W. *Elasticity.* Prentice-Hall, New Jersey, 1973.

[56] Liu, Chien-Kuo, Sanboh Lee, Li-Piin Sung, and Tinh Nguyen. "Load-displacement relations for nanoindentation of viscoelastic materials". *Journal of Applied Physics*, 100:1–9, 2006.

[57] Love, A. E. H. *A Treatise on the Mathematical Theory of Elasticity.* Dover Publications, New York, fourth edition, 1944.

[58] Lu, H., B. Wang, J. Ma, G. Huang, and H. Viswanathan. "Measurement of Creep Compliance of Solid Polymers by Nanoindentation". *Mechanics of Time-Dependent Materials*, 7:189–207, 2003.

[59] Maivald, P., H.J. Butt, S.A.C. Gould, C.B. Prater, B. Drake, J.A. Gurley, V.B. Eiings, and P.K. Hansma. "Using force modulation to image surface elasticities with the atomic force microscope". *Nanotechnology*, 2:103–106, 1991.

[60] Mandal, B. N. "A Note On Bessel Function Dual Integral Equation With Weight Function". *The International Journal of Mathematics and Mathematical Sciences*, 11(3):543–550, 1988.

[61] Mandal, B. N. and Nanigopal Mandal. *Advances in Dual Integral Equations.* Chapman and Hall/CRC Press LLC, Florida, 1999.

[62] Maugis, D. "Adhesion of spheres: The JKR-DMT transition using a dugdale model". *Journal of Colloid and Interface Science*, 150(1):243–269, April 1992.

[63] Morse, Philip M. and Herman Feshbach. *Methods of Theoretical Physics*, volume 1–2. McGraw-Hill Book Company, Inc., New York, 1953.

[64] Nasim, C. "On Dual Integral Equations with Hankel Kernel and an Arbitrary Weight Function". *International journal of mathematics and mathematical sciences*, 9(2):293–300, 1986.

[65] Noble, D. "The solution of Bessel function dual integral equations by a multiplying-factor method". *Proceedings of the Cambridge Philosophical Society*, 59:351–362, 1963.

[66] Nony, L., R. Boisgard, and J.P. Aimé. "Nonlinear dynamical properties of an oscillating tip-cantilever system in the tapping mode". *Journal of Chemical Physics*, 111(4):1615–1627, July 1999.

[67] Odegard, G.M., T.S. Gates, and H.M. Herring. "Characterization of Viscoelastic Properties of Polymeric Materials Through Nanoindentation". *Experimental Mechanics*, 45(2):130–136, April 2005.

[68] Oommen, B. and K.J. Van Vliet. "Effects of nanoscale thickness and elastic nonlinearity on measured mechanical properties of polymeric films". *Thin Solid Films*, 513:235–242, 2006.

[69] Pak, Ronald Y. S. "Asymmetric Wave Propagation in an Elastic Half-Space by a Method of Potentials". *Journal of Applied Mechanics*, 54:121–126, March 1987.

[70] Pak, Ronald Y. S. and Bojan B. Guzina. "Three-Dimensional Green's Functions for a Multilayered Half-Space in Displacement Potentials". *Journal of Engineering Mechanics*, 128(4):449–461, April 2002.

[71] Peters, A. S. *Certain Dual Integral Equations and Sonine's Integrals, IMM-NYU 285.* Institute of Mathematical Sciences, New York University, New York, 1961.

[72] Pethica, J.B. and W.C. Oliver. "Tip Surface Interactions in STM and AFM". *Physica Scripta*, T19:61–66, 1987.

[73] Poularikas, Alexander D. (editor). *The Transforms and Applications Handbook*. CRC Press, Inc., Boca Raton, Florida, 1996.

[74] Rabe, U. and W. Arnold. “Acoustic microscopy by atomic force microscopy”. *Applied Physics Letters*, 64(12):1493–1495, March 1994.

[75] Rabe, U., K. Janser, and W. Arnold. “Vibrations of free and surface-coupled atomic force microscope cantilevers: Theory and experiment”. *Review of Scientific Instruments*, 67(9):3281–3293, September 1996.

[76] Radmacher, M., R.W. Tillmann, and H.E. Gaub. “Imaging viscoelasticity by force modulation with the atomic force microscope”. *Biophysical Journal*, 64:735–742, March 1993.

[77] Saada, Adel S. *Elasticity: Theory and Applications*. Krieger Publishing Company, 2nd edition, 1993.

[78] Sacha, G.M., A. Verdaguer, and M. Salmeron. “Induced Water Condensation and Bridge Formation by Electric Fields in Atomic Force Microscopy”. *The Journal of Physical Chemistry B*, 110(30):14870–14873, 2006.

[79] Schwarz, U.D. “A generalized analytical model for the elastic deformation of an adhesive contact between a sphere and a flat surface”. *Journal of Colloid and Interface Science*, 261:99–106, 2003.

[80] Sharma, P.K. and K. Hanumantha Rao. “Analysis of different approaches for evaluation of surface energy of microbial cells by contact angle goniometry”. *Advances in Colloid and Interface Science*, 98:341–463, 2002.

[81] Singh, S.P., J.F. Smith, and R.P. Singh. “Characterization of the Damping Behavior of a Nanoindentation Instrument for Carrying Out Dynamic Experiments”. *Experimental Mechanics*, 48:571–583, 2008.

[82] Sips, R. "General Theory of Deformation of Viscoelastic Substances". *Journal of Polymer Science*, 7(2/3):191–205, 1951.

[83] Sneddon, Ian N. *Fourier Transforms.* McGraw-Hill Book Company, Inc., New York, first edition, 1951.

[84] Sneddon, Ian N. "The relaxation between load and penetration in the axisymmetric Boussinesq problem for a punch of arbitrary profile". *International Journal of Engineering Science*, 3:47–57, 1965.

[85] Sneddon, Ian N. *Mixed Boundary Value Problems in Potential Theory.* John Wiley and Sons, Inc., New York, first edition, 1966.

[86] Stafford, Christopher M., Bryan D. Vogt, Christopher Harrison, Duangrut Julthongpiput, and Rui Huang. "Elastic Moduli of Ultrathin Amorphous Polymer Films". *Macromolecules*, 39(15):5095–5099, 2006.

[87] Stark, Robert W., Tanja Drobek, Jochen Fricke, Marcus Weth, and Wolfgang M. Heckl. "Determination of elastic properties of single aerogel powder particles with the AFM". *Ultramicroscopy*, 75:161–169, 1998.

[88] Sun, Yujie, Boris Akhremitchev, and Gilbert C. Walker. "Using the Adhesive Interaction between Atomic Force Microscopy Tips and Polymer Surfaces to Measure the Elastic Modulus of Compliant Samples". *Langmuir*, 20(14):5837–5845, 2004.

[89] Tabor, D. "Surface forces and surface interactions". *Journal of Colloid and Interface Science*, 58(1):2–13, January 1977.

[90] Tian, Jiayong, Hirotsugu Ogi, and Masahiko Hirao. "Dynamic-Contact Stiffness at the Interface Between a Vibrating Rigid Sphere and a Semi-Infinite Viscoelas-

tic Solid". *IEEE Transactions on Ultrasonics, Ferroelectrics, and Frequency Control*, 51(11):1557–1563, November 2004.

[91] Tian, Jiayong and Zhoumin Xie. "Dynamic contact stiffness of vibrating rigid sphere contacting semi-infinite transversely isotropic viscoelastic solid". *Acta Mechanica Solida Sinica*, 21(6):580–588, December 2008.

[92] Timoshenko, Stephen P. *History of Strength of Materials*. McGraw-Hill Book Company, Inc., 1953.

[93] Ting, T. C. T. "Contact Problems in the Linear Theory of Viscoelasticity". *Journal of Applied Mechanics*, 248–254, June 1968.

[94] Titchmarsh, E. C. *Introduction to the Theory of Fourier Integrals*. The Clarendon Press, Oxford, second edition edition, 1948.

[95] Tranchida, D., Z. Kiflie, S. Acierno, and S. Piccarolo. "Nanoscale mechanical characterization of polymers by atomic force microscopy (AFM) nanoindentations: viscoelastic characterization of a model material". *Measurement Science and Technology*, 20:1–9, 2009.

[96] Tweedie, Catherine A. and Krystyn J. Van Vliet. "Contact creep compliance of viscoelastic materials via nanoindentation". *Journal of Materials Research*, 21(6):1576–1589, June 2006.

[97] Vanlandingham, M.R., N.-K. Chang, P.L. Drzal, C.C. White, and S.-H. Chang. "Viscoelastic Characterization of Polymers Using Instrumented Indentation. I. Quasi-Static Testing". *Journal of Polymer Science: Part B: Polymer Physics*, 43:1794–1811, 2005.

[98] Vanlandingham, M.R., N.-K. Chang, P.L. Drzal, C.C. White, and S.-H. Chang. "Viscoelastic Characterization of Polymers Using Instrumented Indentation. II.

Dynamic Testing". *Journal of Polymer Science: Part B: Polymer Physics*, 43:1812–1824, 2005.

[99] Wahl, K.J., S.A.S. Asif, J.A. Greenwood, and K.L. Johnson. "Oscillating adhesive contacts between micron-scale tips and compliant polymers". *Journal of Colloid and Interface Science*, 296:178–188, 2006.

REPORT DOCUMENTATION PAGE

Form Approved
OMB No. 074-0188

1. REPORT DATE *(DD-MM-YYYY)* 24-03-2011	**2. REPORT TYPE** Doctoral Dissertation	**3. DATES COVERED** *(From – To)* October 2002 – March 2011

4. TITLE AND SUBTITLE

An Analytical Model of Nanometer Scale Viscoelastic Properties of Polymer Surfaces Measured Using an Atomic Force Microscope

5a. CONTRACT NUMBER

5b. GRANT NUMBER

5c. PROGRAM ELEMENT NUMBER

6. AUTHOR(S)

Goldberg, Jacob B.

5d. PROJECT NUMBER
JON: 06P374 JON: 08P206

5e. TASK NUMBER

5f. WORK UNIT NUMBER

7. PERFORMING ORGANIZATION NAMES(S) AND ADDRESS(S)
Air Force Institute of Technology
Graduate School of Engineering and Management (AFIT/ENC)
2950 Hobson Way, Building 641
WPAFB, OH 45433-8865

8. PERFORMING ORGANIZATION REPORT NUMBER
AFIT/DAM/ENC/11-03

9. SPONSORING/MONITORING AGENCY NAME(S) AND ADDRESS(ES)
AFNWC/EN Attn: Lt. Col. Brian L. Evans
1551 Wyoming Blvd SE, Kirtland AFB, NM 87117 (505)853-3266

10. SPONSOR/MONITOR'S ACRONYM(S)
AFNWC/EN

11. SPONSOR/MONITOR'S REPORT NUMBER(S)

12. DISTRIBUTION/AVAILABILITY STATEMENT

APPROVED FOR PUBLIC RELEASE; DISTRIBUTION UNLIMITED

13. SUPPLEMENTARY NOTES
This material is declared a work of the U.S. Government and is not subject to copyright protection in the United States.

14. ABSTRACT

The United States Air Force and the Department of Defense is increasingly interested in nanomaterials. To study these materials, one needs to measure the mechanics of materials on the nanoscale. Over the past few decades the atomic force microscope (AFM) has been used in various methods to establish local surface properties at the nanoscale. In particular, surface elasticity measurements are crucial to understanding nanoscale surface properties. Problems arise, however, when measuring soft surfaces such as polymers and biological specimens, because these materials have a more complex viscoelastic response.

This research focuses on modeling an AFM dynamic nanoindentation experiment intended to characterize near-surface viscoelastic material parameters. The experiment uses an AFM in dynamic contact mode with a polymer surface to gather frequency dependent amplitude and phase data. A three-dimensional, dynamic viscoelastic model of the AFM and surface interaction is developed and then analytically solved in the linear approximation under appropriate physical assumptions based on the physics of the AFM experimental setup. As an illustrative application, the analytical solution is coupled with experimental data from a polystyrene material to ascertain surface material properties at the nanoscale. Our solution allows the direct calculation of the storage and loss modulus from experimental data.

15. SUBJECT TERMS
Viscoelastic, Material Properties, Atomic Force Microscope, Analytical Model

16. SECURITY CLASSIFICATION OF:			**17. LIMITATION OF ABSTRACT**	**18. NUMBER OF PAGES**	**19a. NAME OF RESPONSIBLE PERSON**
REPORT	**ABSTRACT**	**c. THIS PAGE**			Dr. William P. Baker (AFIT/ENC)
U	U	U	UU	129	**19b. TELEPHONE NUMBER** *(Include area code)* (937) 255-3636, ext. 4517 (William.Baker@afit.edu)

Standard Form 298 (Rev: 8-98)
Prescribed by ANSI Std. Z39-18